NOVEL APPLICATIONS OF COMPUTATIONAL AERODYNAMICS TO AERIAL REFUELLING ANALYSIS

NOUVELLES APPLICATIONS DE L'AÉRODYNAMIQUE COMPUTATIONNELLE À L'ANALYSE DU RAVITAILLEMENT AÉRIEN

A Thesis Submitted to the Division of Graduate Studies
of the Royal Military College of Canada
by

Luke H. Peristy, B.Sc., M.Sc.

In Partial Fulfillment of the Requirements for the Degree of
Doctor of Philosophy

December 2024

To my father, through whom engineering has always been a part of my life

Acknowledgements

First and foremost, I'd like to thank Dr. Ruben Perez for his help and guidance throughout my Ph.D. Whether he was passing along critical reference material, providing feedback on papers and presentations, or dropping one of his famous "Friday Afternoon Ideas" in my lap like a live grenade, both he and his knowledge were an integral part of my academic journey to this point. I'd also like to thank him for his trust in allowing me flexibility in my work. His support in all matters, academic and personal, would have been impossible to do without.

Secondly, I'd like to thank the Department of Airworthiness and Engineering Support at the Department of National Defence for supporting this research (Grant #18485SK101-07). In particular, Laird McKinnon and Jean-Philippe Caron were excellent contacts who provided extremely useful guidance regarding the most practical direction for this research, and I am gratified to know that this RMC/DND collaboration can be considered a success.

I'd also like to thank a number of individuals for their useful technical discussions and general congeniality, including Dr. Tim Takahashi of ASU, Dr. Peter Jansen of RMC, and Dr. Nicolas Fezans, Dr. Christoph Deiler, and Dr. Thomas Jann of DLR. A Ph.D. is a solitary endeavour, and any time I was able to affirmatively interact with anyone "on the outside", it went a long way to reassuring me that I was, in fact, a small part of a research community, and not just a lone wolf with a laptop running calculations into the void.

Finally, I'd like to thank my wife, Anja, who was the only person I know who never asked me "When will you finish?", despite having arguably the most stake in the answer. Your belief in me means the world.

Abstract

Peristy, Luke Howard. Ph.D. Royal Military College of Canada, December 2024. *Novel Applications of Computational Aerodynamics to Aerial Refuelling Analysis.* Supervised by Ruben E. Perez, B.Eng., M.A.Sc., Ph.D., P.Eng., Professor.

Air-to-air refuelling is an operational practice in military aviation which is used to increase mission lengths and to allow aircraft to stay airborne for much longer than would otherwise be possible. Furthermore, there is interest in developing air-to-air refuelling procedures in civil aviation as a means to increase fuel efficiency and to reduce carbon footprint. During air-to-air refuelling, the tanker and receiver aircraft must fly in close formation, such that the wake of the tanker has a detrimental effect on the flight dynamics of the receiver. The challenges associated with air-to-air refuelling generally stem from the necessity of performing the precise flight manoeuvres under adverse conditions. Better understanding of the interaction between the tanker and the receiver has implications for control system design, compatibility analysis, and future certification of civil air-to-air refuelling procedures. To this end, a new analysis methodology was developed and used to examine the positional stability and flight dynamics of the receiver during flying boom and probe-and-drogue refuelling. This methodology uses adjoint-based sensitivity analysis from a potential flow solver to obtain positional stability characteristics at higher computational speed and is combined with higher-order aerodynamic modelling and simplified control systems models. An F/A-18 receiver during probe-and-drogue refuelling was analyzed, revealing that, due to asymmetrical aerodynamic forces, the trim strategy required would cause cross-coupling in the dynamic response of the receiver. The framework was then extended with the inclusion of analytic pilot models to account fully for all aspects of air-to-air refuelling and to predict susceptibility to pilot-induced oscillations during flying boom refuelling. For instance, when the C-5 and C-17 were compared as receivers, the results obtained showed that the C-17 would be prone to pilot-induced oscillations in cases where an equivalent system delay was in excess of 350 ms.

Keywords: Air-to-Air Refuelling, Vortex Lattice Methods, Pilot Induced Oscillations, Flight Dynamics, Handling Qualities

Résumé

Peristy, Luke Howard. Ph.D. Royal Military College of Canada, Décembre 2024. *Nouvelles applications de l'aérodynamique computationnelle à l'analyse du ravitaillement aérien.* Supervisé par Ruben E. Perez, B.Eng., M.A.Sc., Ph.D., P.Eng., Professeur.

Le ravitaillement en vol est une activité opérationnelle qui est utilisée pour augmenter la durée des missions et qui peut permettre aux avions l'option de rester en vol beaucoup plus longtemps qu'il ne serait autrement possible. Lors du ravitaillement en vol, l'avion ravitailleur et l'avion récepteur doivent voler en formation serrée, de sorte que le sillage du ravitailleur a un effet néfaste sur la dynamique de vol du récepteur. Les défis associés au ravitaillement en vol découlent généralement de la nécessité d'effectuer les manœuvres de vol précises dans des conditions défavorables. Une meilleure compréhension de l'interaction entre le ravitailleur-citerne et le récepteur a des implications pour la conception du système de commande, l'analyse de compatibilité et la future certification des procédures de ravitaillement en vol pour des opérations civiles. À cette fin, une nouvelle méthodologie d'analyse a été développée et utilisée pour examiner la stabilité positionelles et la dynamique de vol du récepteur pendant le ravitaillement par perche et du système sonde-drogue. Cette méthodologie utilise une analyse de sensibilité basée sur l'adjoint d'un solveur d'écoulement potentiel pour obtenir des caractéristiques de stabilité de position à une vitesse de calcul plus élevée. Elle est aussi combinée avec une modélisation aérodynamique d'ordre supérieur et des modèles de systèmes de commande simplifiés. L'analyse d'un récepteur F/A-18 pendant le ravitaillement par carburant de la sonde et de la drogue a été effectuée, montrant qu'en raison des forces aérodynamiques asymétriques, la stratégie de compensation provoquerait un couplage de façon crois dans la réponse dynamique du récepteur. Le cadre a ensuite été étendu avec des modèles des pilotes analytiques pour prédire la susceptibilité aux oscillations induites par le pilote lors du ravitaillement en vol. Par example, lorsque le C-5 et le C-17 ont été comparés en tant que récepteurs, les résultats obtenus ont montré que le C-17 serait sujet à des oscillations induites par le pilote dans les cas où le délai équivalent du système dépassait 350 ms.

Mots-clés: Ravitaillement en vol, méthode de réseau de vortex, oscillations induites par le pilote, dynamique de vol, qualités de pilotage

Statement of Contributions

Contributions to Computational Aerodynamics

A novel methodology is introduced which uses adjoints within a vortex lattice method to calculate positional stability quantities, including change in rolling moment with respect to lateral position and change in pitching moment and change in lift with respect to vertical position. This methodology reduces computational time for analyses of air-to-air refuelling procedures where the control and stability of the tanker and receiver are highly coupled.

Contributions to Air-to-Air Refuelling Flight Dynamics

The integration of a vortex lattice method with a 6-degree-of-freedom, 9-state aircraft model and 4-state controller is demonstrated. This methodology uses a novel hybrid approach to resolving the aerodynamic forces and moments on the receiver within the tanker wake. This is then used to predict closed-loop natural modes at the trim points within the wake. Examination of the closed-loop eigenvectors shows cross-coupling effects that were not explicitly taken into account previously when considering aircraft flying qualities.

Contributions to Flying/Handling Qualities

A new positional stability quantity is introduced which relates changes in separation between tanker and receiver to the pilot response required to maintain formation station. This is combined with the use of two analytical pilot models to perform in-the-loop perturbation analyses. Through these analyses, which relate the positional stability, aircraft dynamics, and pilot response to each other, new guidelines are proposed for predicting pilot-induced oscillations susceptibility and subsequently demonstrated through the examination of the C-5 and C-17 when flown as receivers. These guidelines have implications for future aircraft control system design and tanker-receiver compatibility analyses.

Contents

List of Tables

List of Figures

Nomenclature

Roman Symbols

$\bar{c}$	Mean aerodynamic chord [m]
$\bar{q}$	Dynamic pressure [Pa]
AIC	Aerodynamic influence coefficient matrix [-]
$\boldsymbol{n}$	Normal vector [-]
$\boldsymbol{U}$	Air velocity vector [m/s]
$\boldsymbol{V}$	Velocity vector field [m/s]
ℓ	Rolling moment [N·m]
RHS	Right hand side vector [-]
a	Speed of sound [m/s]
$a_{\square\square}$	Aerodynamic influence coefficient [-]
b	Wingspan [m]
c_p	Control stick position [cm]
D	Drag force [N]
$e(s)$	Error signal in the s-domain [-]
F	Force [N]
f	Arbitrary function [-]
f_c	Crossover frequency [rad/s]
g	Gravitational acceleration [m·s^{-2}]

I_{xz}	Cross Product of Inertia about y [$\mathrm{kg} \cdot \mathrm{m}^2$]
I_x	Moment of Inertia about x [$\mathrm{kg} \cdot \mathrm{m}^2$]
I_y	Moment of Inertia about y [$\mathrm{kg} \cdot \mathrm{m}^2$]
I_z	Moment of Inertia about z [$\mathrm{kg} \cdot \mathrm{m}^2$]
K	Gain [-]
L	Lift force [N]
M	Dimensionalized pitching moment [s^{-2}]
m	Mass [kg]
m	Pitching moment [N·m]
n	Normal acceleration [$\mathrm{m} \cdot \mathrm{s}^{-2}$]
n	Yawing moment [N·m]
P	Separation vector, $[\Delta x, \Delta y, \Delta z]$ [-]
p	Roll rate [rad/s]
q	Pitch rate [rad/s]
R	Actuator disc radius [m]
r	Radial axis coordinate [-]
r	Yaw rate [rad/s]
$R_\square$	Residual equation [-]
S	Wing area [m^2]
SM	Static margin [%]
T	Thrust [N]
T_I	Time-lag constant [s]
T_L	Time-lead constant [s]
T_N	Neuromuscular time-lead constant [s]
U	Freestream air speed [m/s]
u	x-component of air velocity vector [m/s]

v	y-component of air velocity vector [m/s]
V_r	Radial velocity from actuator disk [m/s]
V_x	Streamwise velocity from actuator disk [m/s]
W	Weight [N]
w	z-component of air velocity vector [m/s]
X	x-axis coordinate (left-handed axis system) [m]
x	x-axis coordinate (right-handed axis system) [m]
Y	Sideforce force [N]
Y	y-axis coordinate (left-handed axis system) [m]
y	y-axis coordinate (right-handed axis system) [m]
y_i	State vector [-]
Z	Acceleration in the z-direction [m·s^{-2}]
Z	z-axis coordinate (left-handed axis system) [m]
z	z-axis coordinate (right-handed axis system) [m]

Greek Symbols

α	Angle of attack [rad]
β	Sideslip angle [rad]
β_{PG}	Prandtl-Glauert correction factor [-]
$\boldsymbol{\omega}$	Angular velocity vector [rad/s]
Δ	Denotes separation in space [-]
δ	Control surface deflection [rad]
Γ	Vortex circulation strength [s^{-1}]
γ	Flight path angle [rad]
λ	Adjoint vector [-]
ω	Arbitrary frequency [rad/s]

ω_n	Neuromuscular natural frequency [rad/s]
ω_n	Short period natural frequency [rad/s]
Φ	Roll angle [rad]
ϕ	Phase shift [rad]
Ψ	Yaw angle [rad]
ρ	Air density [kg/m^3]
τ_d	Time delay constant [s]
$\tau_{d_{\text{margin}}}$	Time delay margin [s]
Θ	Pitch angle [rad]
θ	Arbitrary angle [rad]
ζ	Damping constant [-]

Subscripts

α	Denotes derivative with respect to angle-of-attack
Δz	Denotes derivative with respect to vertical displacement between tanker and receiver
δ	Denotes derivative with respect to control surface deflection
$\dot{\alpha}$	Denotes derivative with respect to the time derivative of angle-of-attack
∞	Denotes freestream
eff	Denotes effective value
ind	Denotes induced value
rot	Denotes rotation
tail	Denotes component from aircraft tail
wake	Denotes wake component
a	Denotes aileron
B	Denotes body axis
cs	Denotes control system

e	Denotes elevator
i, j, K, l, m	Index variables
m	Denotes margin
N	Number of spanwise panels in a vortex lattice surface
P	Denotes positional value
p	Denotes pilot
q	Denotes derivative with respect to pitch rate
r	Denotes receiver
r	Denotes rudder
S	Denotes stability axis
t	Denotes tanker

Superscripts

T	Transpose of the vector/matrix

Dimensionless Groups

Ma	Mach number
C_ℓ	Rolling Moment Coefficient
C_L	Lift Coefficient
C_m	Pitching Moment Coefficient
C_n	Yawing Moment Coefficient

Acronyms

AAR	Air-to-Air Refuelling
AIC	Aerodynamic Influence Coefficient
CAP	Control Anticipation Parameter
CAS	Control Augmentation System

CFD	Computational Fluid Dynamics
CG	Centre of Gravity
DOD	Department of Defense
DOF	Degree of Freedom
FBR	Flying Boom Refuelling
HARV	High-Alpha Research Vehicle
IDF	Individual Discipline Feasible
KIAS	Knots Indicated Airspeed
PDR	Probe and Drogue Refuelling
PIO	Pilot-Induced Oscillation
RCAF	Royal Canadian Air Force
RTA	Real-time Analysis
SAVE	Surfing Aircraft Vortices for Energy
UAS	Unmanned Aerial System
USAF	United States Air Force
UVLM	Unsteady Vortex Lattice Method
VEMT	Vortex Effect Modelling Technique
VLM	Vortex Lattice Method
VPM	Vortex Panel Method

Axis Definitions

The body axis and stability axis system used can be seen in Figure 4.2, which shows an F/A-18 flying in steady level flight at an angle of attack α, which can be seen in the difference in the body axes (denoted by a subscript B) and the stability axes (denoted by a subscript S). The roll, pitch, and yaw moment coefficients (C_ℓ, C_m, and C_n) are defined about body frame axes x_B, y_B, and z_B respectively. The lift, drag, and side force coefficients (C_L, C_D, and C_Y) are defined as positive along $-z_S$, $-x_S$, and $+y_S$ respectively. The Euler angles Φ, Θ, and Ψ are rotations of the body axes, whereas the angles α and β are aerodynamic angles defined relative to the direction the aircraft is moving within the airflow at velocity V, as shown. Positive control surface deflections are also notated in Figure 1.

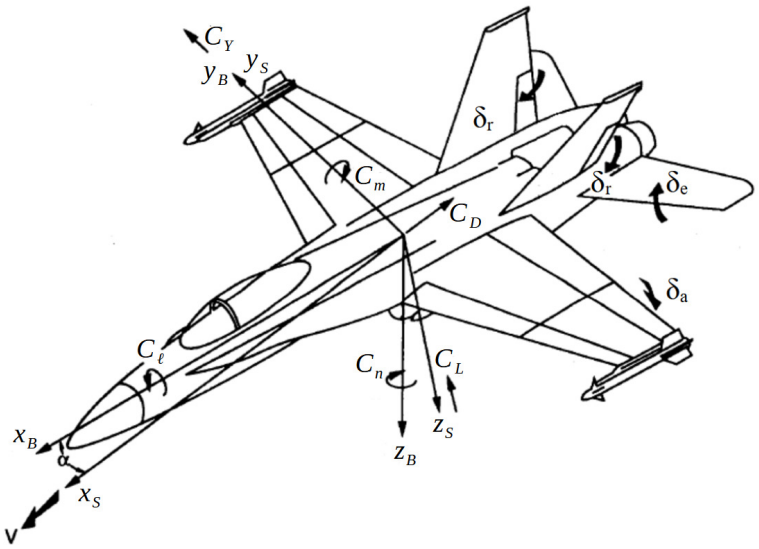

Figure 1: Body axis and stability axis system with control surface sign conventions. [1]

1 Introduction

1.1 Motivation

An aircraft's range or endurance is one of the canonical measures of aircraft performance, and greater endurance, holding all other factors equal, is generally considered desirable regardless of mission profile. While great effort is expended during the design phase of an aircraft's development cycle to maximize its endurance, once in operation, it can be further increased for any individual mission via the transfer of fuel from another aircraft during flight. The transfer of fuel during flight is a process referred to as air-to-air refuelling (AAR) or aerial refuelling, and has over 100 years of operational history. After its first demonstration in the 1920s, AAR enabled the first non-stop flight to circumnavigate the earth in 1949, and it has been a standard practice in many military air forces, worldwide, since the 1950s [2].

In a military context, the advantages of extending an aircraft's range and endurance through AAR are clear, since an aircraft that refuels in-flight will be capable of longer ferry flights and spending longer time on station, thus extending force projection while generally enhancing mission capability and operational effectiveness. Exploratory studies have also suggested that AAR may be a useful addition to civil aviation practice. It has been demonstrated that a long-haul flight with AAR requires less fuel compared to an identical mission with a layover for ground refuelling [3]. An aircraft that receives fuel via AAR can have a reduced initial take-off weight compared to a baseline mission that includes a stop-over for fuel. This results in fuel burn improvements via an overall reduction in power required (and therefore fuel used) during take-off, and also eliminates the need to land and take-off again following a stop-over. Nangia has suggested that reductions in fuel usage for international flights that utilize AAR could be between 30% and 40%, with commensurate cost savings as long as the amount of fuel dispensed by the tanker to various receivers is greater than the amount of fuel used by the tanker in-flight [4]. Furthermore, removing the need for a fuel stop-over also reduces the number of ground-air-ground cycles, increasing the time between maintenance events, and improving the overall lifespan of an aircraft.

While the advantages of AAR are well-known, so are its challenges. The process of AAR necessitates that the aircraft dispensing fuel (the tanker) and the aircraft receiving fuel (the receiver) fly in close formation flight so as to facilitate the flow of fuel through either a long, rigid boom, or a flexible hose. However, while flying in close formation flight, the receiver is subjected to aerodynamic disturbances due to the wake of the tanker. Depending on the area of the wake in which the receiver is flying in, it may be subject to flow features such as upwash, sidewash, or downwash caused by the tanker's lifting surfaces, or backwash from the tanker's propulsive units. A schematic of these flow features can be seen in Figure 1.1.

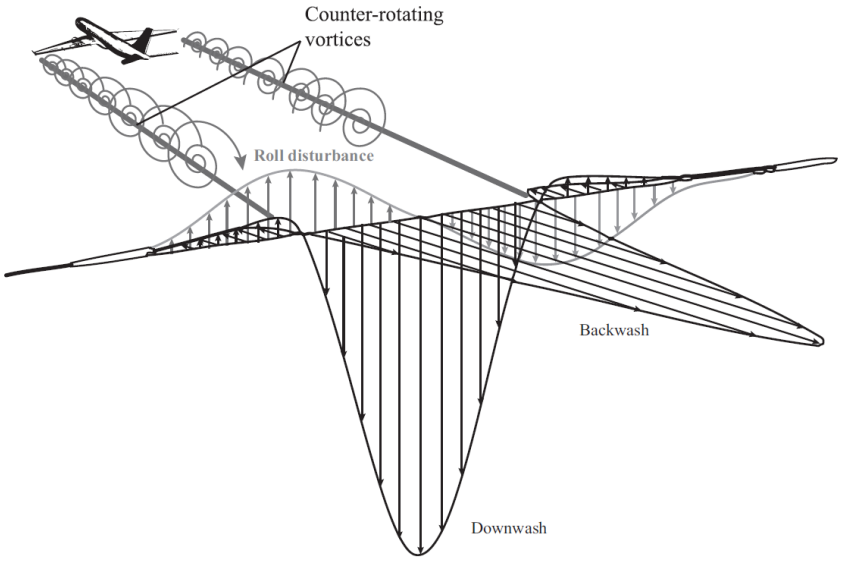

Figure 1.1: Typical spanwise flow features of an aircraft wake [2].

The upwash, downwash, sidewash, and backwash lead to aerodynamic forces on the receiver which must be counteracted by pilot inputs. The aerodynamic forces are not typically constant, and therefore pilot inputs must be continuously adjusted in order to execute the precise manœuvres required during AAR. The exact nature of the required manœuvres is typically determined by the type of AAR procedure being performed. The two methods used most often for AAR are known as probe and drogue refuelling (PDR) and flying boom refuelling (FBR). During PDR, the tanker extends a long flexible hose at the end of which is a cone-shaped drogue. The drogue remains behind and below the tanker as it flies straight and level. The receiver aircraft then extends a probe from the airframe

and the pilot directs it into the drogue. Once the connection is made, fuel is transferred and the aircraft fly in this physically linked formation until the transfer is complete. PDR typically requires precise flight inputs in both the longitudinal and lateral-direction axes when tracking the movement of the drogue during the docking procedure.

To enable FBR, a rigid tube or boom is fitted to the underside of the tanker aircraft. This boom is usually extensible and fitted with small wings to provide some aerodynamic control. The receiver aircraft is also fitted with a fixed-point receptacle or socket on the upper surface of its fuselage. During the FBR procedure, the tanker and receiver fly in formation and a boom operator on board the tanker uses a control stick to manoeuvre the boom and its nozzle into the receiver's socket [5]. This typically requires its most precise flight inputs in the longitudinal plane, since the receiver does not need to track the boom, but must rather precisely hold position near the tanker.

The tanker and receiver themselves are also important factors, since different tankers create different wakes, and different receivers react to these wakes differently. Clearing tanker-receiver pairs for operation is an extensive process that involves a combination of analysis and flight testing [6]. This analysis is intended to predict the effect of the tanker wake on the refuelling aircraft, and to determine if the refuelling procedure can be completed safely. Over long time scales, computational fluid dynamics (CFD) calculations, simulator training, and flight tests can be combined to create an extensive body of evidence that demonstrates tanker-receiver compatibility [6]. However, it is not always possible for aircraft to refuel in flight using an approved tanker. When military aircraft are deployed and require refuelling from an unapproved tanker, a risk assessment is performed and a special purpose flight permit is issued. This process can rely substantially on engineering judgment and the results are often subject to large uncertainties. Furthermore, during an aircraft's design phase, it may not always be practical to test every possible control system configuration for its suitability to the AAR task in a simulator environment. Therefore, analysis methods that provide guidance regarding appropriate gains, delays, and filters for a given aircraft configuration can be used to narrow the design space and direct the design process towards a smaller number of potential solutions for high-fidelity analysis, saving time and resources. Furthermore, results generated from medium-fidelity methods are more appropriate for use in a real-time analysis (RTA) environment. High-fidelity CFD analyses generate large amounts of data, whose processing, storage, and retrieval requires significant computational resources. Medium-fidelity analysis techniques typically produce smaller amounts of data, which can be stored easily and retrieved in time scales suitable for RTA. In short, while the precision and accuracy

of high-fidelity simulation may be desirable when time and resources are not significant factors, the continued development fast and computationally light methods is still important when time and resources are limited.

1.2 Objectives and Significance

The principal goal of this research is to develop a multi-modal AAR analysis framework that is both light in terms of computational resources required, and robust to different types of tankers, receivers, and refuelling methods. This is achieved through the following:

- The development of a computational aerodynamic tool to evaluate the forces and moments imparted upon a receiver flying in a tanker wake.
- The introduction of novel stability quantities and a demonstration of their relevance to the AAR task.
- The examination of a fully coupled 6-degree-of-freedom (DOF) aircraft dynamic model, and discussion of its implications for the AAR task.
- The use of mathematical pilot models and the a demonstration of their relevance to control systems design.

The AAR task exists in the intersection of aerodynamics, flight dynamics, control systems design, and human factors, all of which will be addressed through various methods. Successful demonstration of the above will have implications for AAR analysis and research, since most current AAR projects involve large teams with significant resources in terms of computing power, simulator infrastructure, and funding. The ability to generate useful insights about the AAR task for any given tanker-receiver pair with a minimum of resources has the potential to streamline military operations and the aircraft design process for configurations that will require AAR as part of their mission profile. It could also reduce the number of simulator and flight tests required for clearance by significantly narrowing the range of feasible refuelling envelopes at minimal cost in terms of both time and computing. Furthermore, any new insights generated over the course of this research will be relevant to current AAR practice and will constitute a meaningful contribution to the state of the art.

1.2.1 Contributions

This thesis improves the state of the art in three main areas: computational aerodynamics, AAR flight dynamics, and human factors/pilot-induced oscillation avoidance.

Contributions to Computational Aerodynamics

A novel methodology is introduced which uses adjoints within a vortex lattice method to calculate positional stability quantities, including change in rolling moment with respect to lateral position and change in pitching moment and change in lift with respect to vertical position. This methodology reduces computational time for analyses of air-to-air refuelling procedures where the control and stability of the tanker and receiver are highly coupled.

Contributions to Air-to-Air Refuelling Flight Dynamics

The integration of a vortex lattice method with a 6-degree-of-freedom, 9-state aircraft model and 4-state controller is demonstrated. This methodology uses a novel hybrid approach to resolving the aerodynamic forces and moments on the receiver within the tanker wake. This is then used to predict closed-loop natural modes at the trim points within the wake. Examination of the closed-loop eigenvectors shows cross-coupling effects that were not explicitly taken into account previously when considering aircraft flying qualities.

Contributions to Flying/Handling Qualities

A new positional stability quantity is introduced which relates changes in separation between tanker and receiver to the pilot response required to maintain formation station. This is combined with the use of two analytical pilot models to perform in-the-loop perturbation analyses. Through these analyses, which relate the positional stability, aircraft dynamics, and pilot response to each other, new guidelines are proposed for predicting pilot-induced oscillations susceptibility and subsequently demonstrated through the examination of the C-5 and C-17 when flown as receivers. These guidelines have implications for future aircraft control system design and tanker-receiver compatibility analyses.

1.3 Overview

This dissertation is organized as follows: Chapter 2 presents a literature review of previous work done in the fields of AAR, wake modelling, control system design, and AAR refuelling handling qualities. Chapter 3 introduces the necessary methodology used for rapid AAR analysis and a novel technique for calculating receiver positional stability quantities that describe the ability of a receiver to hold its position relative to the tanker during AAR. Chapter 4 examines lateral-directional positional stability, assesses its relevance regarding the dynamic modes of a single-seat fighter receiver, and contains insights regarding the prediction of

handling qualities specific to the AAR task. Chapter 5 examines positional stability and its relevance to control system design in the longitudinal axis for FBR. It also demonstrates the feasibility of using different analytical pilot models in closed loop control system design. Finally, Chapter 6 summarizes the dissertation's conclusions and recommendations.

Units of measurement will be consistent with the International System of Units (SI units) except in cases where the aviation standard is to express specific quantities using the units of Imperial Measurement System. For example, altitude will be expressed in terms of feet (ft) rather than meters (m).

2 Literature Review

AAR challenges have stimulated research to understand the influence of tanker aircraft wakes on receiver aircraft and flight control system design. These two areas are related since, as the influence of the tanker aircraft and its wake are modelled more effectively, there can be a corresponding improvement in the flight control system design. The most recent advancements in AAR have been driven predominantly by the continuing development of automated refuelling processes in both unmanned aerial systems (UASs) [5] and crewed receivers [7]. However, until automated refuelling procedures demonstrate a human level of proficiency in their ability to perform the AAR task, there will be practical reasons to study AAR as currently practised on human-controlled aircraft. This literature review will summarize previous research in the following areas:

1. Aircraft and wake modelling
2. Experiments, pilot-in-the-loop simulations, and flight tests

It will examine and summarize the current state of the art in order to identify areas where further improvement is possible. It will not extend to certain topics which are beyond the scope of this dissertation, such as drogue and hose dynamic modelling and advanced flight control system design architectures.

2.1 Aircraft and Wake Modelling

Operational considerations for formation flight and AAR contain some overlap, hence analysis methods for formation flight may have implications for AAR analysis, and *vice versa*.

2.1.1 Computational Modelling of Wake and Receiver

Much of the earliest modelling and analysis of the effect of a tanker wake on a receiver was done by Bloy and his colleagues over of period of time from 1986 to 2002. This has included modelling a tanker aircraft as a horseshoe vortex with a vortex lattice representation of the receiver to examine the receiver's lateral

dynamic stability [8] and longitudinal dynamic stability [9, 10], aerodynamic interference [11, 12], and tanker trajectory [13]. Bloy *et al.*'s earlier work used a simple horseshoe vortex with an appropriate circulation distribution to model the flowfield of the tanker. However, later work by Bloy and West used a line vortex model to account for the effect of wake roll-up [14], and this was used further in later work by Bloy and Lea examining the directional stability of a large receiver aircraft [15]. In the lateral-directional axis, Bloy noted that a receiver slightly displaced from the tanker centreline displayed static stability, but was also dynamically unstable [8]. Later, Bloy and Jouma noted the introduction of two oscillatory dynamic modes that were not present in free-air dynamics. One of these, involving a rolling oscillation, was highly damped, and the other, primarily involving an oscillation in lateral position, was unstable [15]. In the longitudinal axis, Bloy *et al.* found that their subject receiver aircraft exhibited instability depending on the differences in downwash gradients experienced by the wing and tail [9, 10].

Bloy *et al.* also performed a campaign of wind tunnel tests to validate their aerodynamic models [11, 12, 15]. Bloy's most recent contribution, with Khan, was the development of an aerodynamic model for use in a real-time simulation [16]. These models generally agreed well with the wind tunnel measurements, although some discrepancies were noted in earlier work due to the simplicity of the horseshoe vortex model. Bloy's dynamics models were generally based on a single-point mass. They found that this method was adequately accurate as long as the wingspan of the receiver aircraft was much less than that of the tanker aircraft [16].

This is a similar approach to that taken by Dogan and Blake. Venkataramanan and Dogan developed a dynamic model for AAR that included the effect of time-varying mass and inertia associated with fuel transfer, the induced wind of the tanker, and atmospheric turbulence. This resulted in a set of non-linear 6-DOF equations of motion for the receiver aircraft [17]. Dogan *et al.* developed a model that expressed the air velocities in the wake as a function of the separations between the tanker and receiver. This allowed them to develop flight dynamics equations that included effective wind terms thus removing the necessity for forces and moments to be calculated explicitly [18]. Dogan *et al.* proceeded to use this model in the design of a linear position-tracking controller [19]. Tucker, Blake, and Dogan derived non-linear 6-DOF equations of motion for the receiver aircraft that accounted for the movement of the centre of mass during fuel transfer, and embedded it in an integrated simulation environment with a feedback controller [20].

Dogan *et al.* also used a Vortex Effect Modelling Technique (VEMT) to model the wing and horizontal tail of the tanker aircraft. This model was able to model

accurately the effect of the wake vortex on the dynamics of the receiver aircraft. The induced-wind components calculated using the VEMT were in good agreement with flight test data [21]. Blake *et al.* also performed wind tunnel tests to compare to results generated by a vortex lattice code [22]. They found that the vortex lattice calculations accurately predicted wake-induced effects on lift and pitching moment in the longitudinal axis. The predicted wake-induced effects on rolling moment were also found to be very accurate compared to the wind tunnel survey. However, the vortex lattice method (VLM) code predicted the drag effects quite poorly, which Blake speculates was due to the model's neglect of viscous effects.

The most recent work performed by Dogan and Blake focused on modelling the bow-wave effect. They initially used a combination of inviscid sources and sinks and VLMs. They found that vortex-based methods alone failed to model the bow wave effect when aircraft were separated by small distances. By using stream functions superimposed on the flow field induced by horseshoe vortices, they were able to produce results that were in good agreement with CFD calculations [23]. This method was also used by Dai *et al* [24]. Blake *et al.* further improved on this method by using an Euler-based *Cart3D* code. The results provided by *Cart3D* regarding the effect of the receiver on the tanker aircraft were in reasonable agreement with flight test data. They conclude that the volume-induced flowfield must be accounted for when modelling the bow wave effect [25]. Bow wave modelling was further examined by Liu *et al.* who used a combination of CFD data and deep learning algorithms to estimate the receiver bow wave in real time in an effort to avoid the use of lookup tables [26].

Katz demonstrated the use of a panel code, VSAERO, to estimate the aerodynamic interaction between a KC-135 tanker and MQ-9 Reaper receiver. He concluded that the stability of the refuelling aircraft was most sensitive to changes in the lateral and vertical separation compared to changes in the longitudinal separation [27].

2.1.2 Wake Modelling for Formation Flight

Most early work on formation flight was focused on birds. One of the first examinations of formation flight in the context of aviation was performed by Maskew [28], who used a VLM to estimate the potential benefits of formation flight for aircraft. He noted that induced drag reductions of 20% to 50% were possible, depending on the formation used, although these benefits were extremely sensitive to lateral or vertical deviations from the identified optimal position in

the wake. Blake and Multhopp built on that work by using a combination of VLMs and viscous core horseshoe vortices, finding that fifty percent of the induced drag benefit was lost if the optimum flight position could not be maintained to better than 10% of a wing span [29]. VLM calculations performed by Blake showed that the calculated induced rolling moment was of a smaller magnitude than that calculated from an equivalent horseshoe vortex representation. Blake further extended the VLM to include calculation of forces, moments, and equations of motion for aircraft in formation. However, the computational costs of modelling individual aircraft was considered prohibitively expensive, so a reduction in states and variables was made by using a database of experimental data [30]. By deriving stability derivatives, Blake found dynamic modes relevant to formation flight and AAR that were both stable and unstable. Following this, Venkataramanan and Dogan collaborated with Blake on a 6-DOF analysis using a modified horseshoe vortex model with the intention of designing a non-linear controller for UASs flying in close formation [31]. This model was compared to wind tunnel experiments, demonstrating adequate agreement with the effect of lateral spacing on rolling moment, side force, and wake-induced drag, but also exposing significant differences with the effect of vertical spacing on lift, pitching moment, side force and wake-induced drag. Venkataramanan *et al.* concluded that an improved vortex model was necessary to obtain better agreement with the wind tunnel experiments.

Dogan *et al.* collaborated to develop a model that could capture the aerodynamic coupling between aircraft in formation flight. Blake performed further wind tunnel experiments with Gingras, observing that VLM calculations predicted effects on lift well, except in areas of the flow where there was great overlap in the spanwise direction [32]. The VLM calculations also predicted an induced drag reduction of 40% with 10% lateral overlap, whereas wind tunnel experiments showed induced drag reduction of 25% with 15% lateral overlap. This discrepancy was thought to have been caused by flow separation at the wing tips. Nevertheless, excellent agreement was found between the predicted and experimentally determined stability boundaries for lift and rolling moment derivatives, although the pitch moment derivatives agreed to a lesser degree. Bramesfeld and Maughmer examined the effects of wake roll-up on inviscid aerodynamic models [33] where fixed and relaxed-wake models produced similar results for the induced-drag savings. However, in the region near the lowest induced drag factors, the fixed wake model predicted a wider range of lateral separation than the relaxed-wake model did. Bramesfeld and Maughmer concluded that a fixed-wake model is likely to be of sufficient accuracy for applications where computational power is at a premium, such as in RTA or part of automated formation flight control systems.

Saban and Whidborne used a wake vortex model based on Weissinger's extended lifting line theory to examine the aerodynamic coupling between aircraft flying in close formation. This computational method was integrated with *Simulink* to demonstrate how analyzing the aerodynamic coupling can support the design of automatic control systems [34]. In the interest of computational efficiency, Zhang and Liu developed a continuous vortex sheet model by combining a single horseshoe vortex with an elliptical lift distribution to represent both aircraft flying in formation. The resulting predicted induced lift and rolling moments compared favourably to wind tunnel experiments and were more accurate than a standard horseshoe vortex model. However, the model seemed inadequate at predicting the side force effects observed in flight tests [35]. Fleischmann and Lone developed an unsteady VLM to predict aerodynamic forces and moments on C-17 aircraft in formation flight. This model is also notable for its use of Rankine vortices, rather than Biot-Savart vortices that introduce singularities to the flow field [36]. They also applied their analysis methodology to predict potential fuel burn benefit from a Surfing Aircraft Vortices for Energy (SAVE) flight test trial involving two C-17 military aircraft with 1250 meters of longitudinal separation, finding that they could predict the overall trends in fuel savings as a function of location. However, the method underestimated the actual values reported by the United States Air Force (USAF) by up to 40%.

Ning *et al.* used a Betz wake model with an empirical vortex core model to examine the effects of wake roll-up, vortex decay, vortex instabilities and atmospheric turbulence [37]. They used two phase wake decay models developed by Holzäpfel [38] to propagate the wake downstream and Monte Carlo simulations to allow for realistic variation and uncertainty in wake propagation and tracking. They concluded that turbulent gusts cause the greatest variation in induced drag savings suggesting that extended formation flight may only be practical for low turbulence levels with longitudinal spacing between aircraft of less than 50 spans. Improvements in precision navigation and remote sensing would be useful in minimizing these errors. Kless *et al.* built on the work of Ning *et al.* using the Betz method to propagate the wakes generated with Euler simulations [39]. These were then used as boundary conditions on a full CFD domain with adaptive mesh representing the trailing aircraft. They found that roll trimming eroded inviscid drag savings, but that the trailing aircraft induced drag during subsonic flight was reduced by 54% and 35% trans-sonic flight when trimmed in roll. Like Ning *et al.* they concluded that effective vortex tracking was a major challenge that must be met before formation flight becomes a viable option due to the sensitivity of the fuel savings to the location of the trailing aircraft relative to the vortex.

It is generally agreed that the efficacy of formation flight, in terms of overall

improvements to fuel consumption, is dependent on how precisely the following aircraft is able to fly in the optimal area of the wake while simultaneously limiting magnitude and number of control inputs required to maintain trim. This is because fuel saved from induced drag reduction may be cancelled out by the increased fuel costs of trim maintenance in scenarios where the required control surface deflections cause large, temporary increases in drag [30, 36].

2.1.3 Aircraft and Wake Modelling Discussion

Both flight tests and computational studies show that the tanker's wake has a major effect on receiver dynamics. The salient question of how to resolve the downwash and sidewash components of the wake into forces and moments on the receiver has therefore been approached in two different ways. The first approach involves distributing the wake over the lifting surfaces of the receiver and directly calculating the resultant aerodynamic forces and moments on the receiver using CFD methods. However, CFD can only be used for specific combinations of tanker and receiver [19], with the results typically being stored in look-up tables [40]. In this approach, the amount of data generated by CFD analyses can be prohibitively large. Fezans and Jann have stated that the data imported into a real time simulation require a compromise between precision and memory usage [7]. The second approach to resolve aerodynamic forces and moments, first demonstrated by Bloy and Khan [16] and then also used by Venkataramanan and Dogan *et al.* [18], is to calculate the downwash, sidewash, and velocity gradients at a single point, typically taken to be the receiver's centre of gravity (CG). This is an approach that has proven better in cases where the receiver wingspan is much smaller than that of the tanker, since the implicit or explicit averaging about a single point is a more valid approximation when the amount of downwash and sidewash varies less across the wingspan when compared to its average [16]. In general, algorithmic and methodological improvements are important in any situation in which either time or computational power is limited. This is what motivates this present work's exploration of new ways to improve computational efficiency without sacrificing fidelity.

The use of VLMs represents a middle ground in terms of computational speed and fidelity. VLM computational grids require a number of points that is several orders of magnitude less than what is required for a good quality CFD grid. Correspondingly, the time required to perform a single VLM calculation is several orders of magnitude less than what is required for the CFD calculation, and several orders of magnitude less data is generated. The extensive use of vortex lattice- and other potential flow-based analyses in formation flight research demonstrates their effectiveness in wake modelling. However, the effect of wake

roll-up begins to become more relevant when separation between aircraft in formation flight is larger. In general, it appears difficult to predict simultaneously the drag and rolling moment experienced by the trailing aircraft without accounting for the wake roll-up [41]. However, even some methodologies that explicitly calculate wake roll-up can significantly differ from flight tests in terms of predicted drag [36]. This trend can be seen in other VLM-based work, such as those of Blake *et al.* [22,32] and Venkataramanan *et al.* [31], although in the latter case, the single-point modelling method may be implicated as a cause for the discrepancy between predicted results and wind tunnel results.

An under-explored aspect of the wake modelling with vortex lattice and potential flow methods is the effect of propulsion, either as propwash or jetwash. While such effects may not be relevant at large separations, they create a measurable contribution to the tanker wake in the nearfield. Only Weinerfelt and Nilsson explicitly mention the use of a basic propeller slipstream model [42]. Jet or propeller effects are generally only considered in CFD work, such as the aforementioned Fezans *et al.* [7, 40, 43], or in the case of Li *et al.* who examined jet impingement on a small fighter aircraft using a Reynolds-Averaged Navier-Stokes calculation, and found that it can have a significant impact on the local rolling moment and lift force should it occur [44]. Effect of propwash and other propulsion effects will therefore be considered using the methodology introduced presently in Chapter 3 and further discussed in Chapter 4.

2.2 Experiments, Pilot-in-the-Loop Simulations, and Flight Tests

An early account of the difficulties encountered during AAR flight tests was given by Bradley [45]. Bradley reported that both VC-10 and Victor aircraft exhibited a short period pitch oscillation when making contact with the flying boom or in the refuelling position. This oscillatory behaviour was more or less pronounced depending on both the tanker and the airspeed. Flight test data of a VC-10 receiver behind a Victor K2 tanker exhibited oscillations in pilot stick force and normal acceleration, and these oscillations had higher frequencies at 310 knots, indicated airspeed (KIAS) than they did at 250 KIAS. Similar oscillatory behaviours were also noted in flight tests for the FBR of the C-17. Iloputaife *et al.* strongly implicated a variety of causes for deficient handling qualities reported, including the small frequency separation between the short period and longitudinal control system dynamics, and bow wave effects leading to poor stability of the tanker [46]. In the longitudinal axis, this was alleviated in part by reducing the

pitch control sensitivity, with further improvements to the flight control law being subsequently documented by Weltz *et al.* that minimized tendencies towards pilot-induced oscillations (PIOs) during the AAR task [47].

The presence of PIOs during AAR is not limited to large aircraft. In 1974, *Calspan* conducted an investigation on longitudinal flying qualities for fighters, using the AAR task as one of the flight phases from which to acquire handling qualities data. Taschner used this data set to examine the effect of rate command attitude hold controls, attitude command attitude hold controls, and conventional flight controls on AAR handling qualities. He did not find that one control response type was necessarily better than the others, but rather suggested the existence of tradeoffs which depended on the pilot's familiarity with the flight dynamics [48]. He also documented that the previously established Bandwith criterion was a poor predictor of poor handling qualities in cases of lightly damped short period longitudinal dynamics or improperly-designed lead compensation [49].

Mitchell and Klyde used the PDR AAR task with the F-14 as a test bed to examine PIO characteristics [50]. Bidinotto *et al.* then used the PIO detection paradigm introduced by Mitchell and Klyde to analyze the feasibility of using analytical pilot models with a simulated PIO-prone aircraft. They demonstrated that an analytical pilot model could produce PIOs in a simulation when given a specific task to be performed by an aircraft plant which was theoretically susceptible to PIOs and also highly unstable [51].

The most recent published work regarding AAR flying and handling qualities is the product of ground-based pilot-in-the-loop simulations. Wang *et al.* used a simulated F-16 with a non-linear dynamics model with variable flight control system parameters to determine bounds on the bandwidth and magnitude of the frequency response to pilot inputs corresponding to Level 1 and Level 2 flying qualities [52]. Yin *et al.* used an identical methodology with simulator-based analyses to suggest new control law requirements to prevent PIOs in pitch during FBR [53]. Unsurprisingly, there was significant overlap between the bounds of Level 1 flying qualities and the PIO-avoidance bounds. Any simulated aircraft with Level 1 flying qualities does not exhibit PIOs almost by definition. Lu *et al.* built on this work by suggesting a "handling quality metric" for PDR based on the maximum response of the flight path angle to a "chirp" signal of variable frequency. This handling quality metric exhibited moderate correlation with the Cooper-Harper rating given by pilots performing the AAR task in the simulator [54]. That team also applied an analytical pilot model, similar to the ones used by Bidinotto *et al.*, although it was only used to determine a reasonable value of the pilot gain the pitch axis [51].

In the U.S., most AAR research is proprietary [5], but some information exists about refuelling projects undertaken in Europe. Weinerfelt and Nilsson summarized efforts at Saab Aerosystems to develop a real-time model for AAR in order to provide simulation and visualization tools [42]. Saab combined an internally-developed wing-tip vortex model coupled with a propeller slipstream model to estimate the flowfield behind a C-130 Hercules, and combined it with a drogue dynamic model in a flight simulator. There is a similar, but more extensive, AAR project currently being developed by Fezans *et al.* that seeks to approach the problem with both medium-fidelity and high-fidelity tools including analytical VLM methods, flight tests, CFD, wind tunnel measurements, and control systems simulations [7,43]. This has resulted in extensive pilot-in-the-loop simulations being performed for helicopter refuelling, single-seater fighter refuelling, and tanker refuelling [40]. The project's stated aim is to eventually demonstrate fully autonomous AAR using autonomous control of the receiver and a fully actuated drogue [40].

2.2.1 Pilot-in-the-Loop Simulator and Flight Test Discussion

Due to the high level of precision flight path control required to successfully perform AAR, an examination of the purely open-loop response of a receiver in the tanker wake is of limited utility. The closed-loop and pilot-in-the-loop responses of the receiver during AAR are of greater practical importance, and this has been driving research to develop AAR-specific flying and handling qualities guidelines using flight tests and pilot-in-the-loop simulations. The previous work of Taschner, Wang *et al.*, and Yin *et al.* demonstrated the relevance of flight path angle response to both AAR handling qualities and PIO avoidance [48, 52, 53]. However, such research requires non-trivial investment in either flight testing or simulator infrastructure. An approach involving an analytical pilot response, similar to that taken by Lu *et al.* in Ref. [54], can generate actionable insights at a fraction of the cost due to its ease of implementation. This present work expands on the work of Lu *et al.* in Chapter 5 by demonstrating a methodology that relates analytic pilot response and receiver positional stability to PIO susceptibility. This methodology can be a valuable tool for addressing PIOs early in an aircraft's design process, while avoiding the need for flight tests or pilot-in-the-loop simulations.

3 Aerodynamic Modelling of Aircraft and Wakes

Analysis of AAR has always fundamentally required calculation of the air velocity field in the wake of a tanker around the refuelling contact point, and an estimate of its effect on the mechanics and dynamics of the receiver. Recalling that potential flow-based analyses, such as vortex lattice methods, have been effective tools for the completion of both tasks in previous work, a potential flow-based VLM was chosen to model the various tanker and receiver aircraft throughout this work, because it can be easily adapted to different aircraft geometries, and has demonstrated the ability to capture the major features of a tanker's wake and its resultant forces and moments on a receiver, at low computational cost. This chapter will provide an overview of the basic theory behind this VLM and will discuss its relevant technical considerations and limitations. This chapter will also discuss the novel methodological improvements made, and introduce the mathematics behind the sensitivity analysis that will be used in this work.

3.1 Potential Flow Theory and Vortex Panel Methods

3.1.1 Potential Flow Theory

Potential flow methods are so-called due to their derivation from conservation of mass and irrotationality resulting in the calculation of a velocity field whose potential satisfies Laplace's Equation. This can be shown as follows:

Consider Equation 3.1 for the conservation of mass in an incompressible flow

$$\nabla \cdot (\boldsymbol{V}) = 0 \tag{3.1}$$

where $\nabla\cdot$ is the divergence operator and $\boldsymbol{V}$ is the velocity vector field. Conservation of mass requires that the divergence of the velocity vector field is 0 at all

points *i.e.* the amount of flow into all points is the same as the amount of flow out. We can also consider the vorticity, or curl, of this vector field, which is defined as $\xi = \nabla \times \boldsymbol{V} = 2\boldsymbol{\omega}$, where $\boldsymbol{\omega}$ is the vector describing the flow's angular velocity. Assuming that the flow is irrotational at all points such that $\nabla \times \boldsymbol{V} = 0$, this implies that the fluid elements have no angular velocity and their motion is purely translational. This assumption is valid for flows without viscosity, and therefore can be used to approximate flow fields in which viscosity has a very small effect, such as in the case of flow around aircraft.

In order to proceed, a scalar function ϕ, known as the velocity potential, is introduced and defined such that its gradient is the flow velocity field $\boldsymbol{V}$. It follows from vector calculus that $\nabla \times (\nabla\phi) = 0$ for all scalar functions. Therefore, the velocity field derived from ϕ automatically satisfies irrotationality. In addition, $\nabla \cdot (\nabla\phi) = \nabla^2\phi = 0$ is Laplace's Equation, a linear differential equation also seen in electrostatics. If the function, ϕ, satisfies Laplace's Equation, then the resulting velocity field can be calculated from the gradient of the function.

$$\mathbf{V} = \nabla\phi \tag{3.2}$$

This formulation is very useful because any velocity field that satisfies Laplace's equation may be added to any other velocity field that satisfies Laplace's equation to create a different velocity field that also satisfies Laplace's equation. In practice, this means that representative flow fields can be created by superimposing elementary flows such as point/line sources, point/line sinks, point/line doublets, and point/line vortices to create valid irrotational inviscid flows. The VLM and vortex panel method (VPM) are based on the addition of velocity contribution from line vortices. Though it neglects several fluid properties, such as viscosity, potential flow theory is a valid analysis model for this work since aircraft flying in close proximity operate in a linear aerodynamic regime where near-field vortex decay is negligible. In polar coordinates, Laplace's Equation is as follows:

$$\frac{1}{r}\frac{\partial}{\partial r}\left(r\frac{\partial\phi}{\partial r}\right) + \frac{1}{r^2}\frac{\partial^2\phi}{\partial\theta^2} = 0 \tag{3.3}$$

A velocity potential function ϕ that satisfies this equation will have its radial and angular velocities (V_r and V_θ) given by the following derivatives:

$$V_r = \frac{\partial\phi}{\partial r}, \quad V_\theta = \frac{1}{r}\frac{\partial\phi}{\partial\theta} \tag{3.4}$$

Given this, it is trivial to show that the potential function that is a linear function of θ:

$$\phi = -\frac{\Gamma}{2\pi}\theta \tag{3.5}$$

both satisfies Laplace's Equation and results in axial and radial velocities of

$$V_r = 0 \qquad V_\theta = -\frac{\Gamma}{2\pi r} \tag{3.6}$$

This is the basis for a 2D irrotational vortex flow where the velocity of the flow at a point P_0 around some vortex core is a function of the vortex strength, Γ, and inversely proportional to the distance r from P_0 to the vortex core. This construction of a 2D irrotational vortex flow can be extended to a third dimension by extending the point vortex into a vortex line or filament. Laplace's Equation in 3D cylindrical coordinates is:

$$\frac{1}{r}\frac{\partial}{\partial r}\left(r\frac{\partial \phi}{\partial r}\right) + \frac{1}{r^2}\frac{\partial^2 \phi}{\partial \theta^2} + \frac{d^2\phi}{dz^2} = 0 \tag{3.7}$$

and therefore a vortex filament of infinite length with the potential function presented in Equation 3.5 also satisfies Laplace's Equation in three dimensions.

Consider the finite length vortex filament extending from P_1 to P_2 as sketched in Figure 3.1.

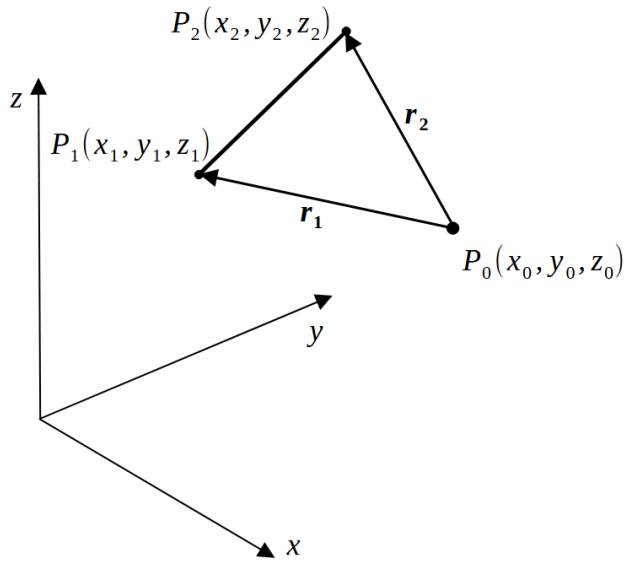

Figure 3.1: Sketch of a vortex filament of finite length.

Given a generalized three-dimensional vortex filament, the flowfield induced at some point of interest, P_0, can be found using the Biot-Savart law.

$$d\boldsymbol{V} = \frac{\Gamma}{4\pi} \cdot \frac{d\boldsymbol{l} \times \boldsymbol{r}}{|\boldsymbol{r}|^3} \tag{3.8}$$

where $\boldsymbol{l}$ is some infinitesimal vector along the vortex filament. Integrating $\boldsymbol{l}$ over the entire vortex filament gives the total induced velocity at P_0.

$$\boldsymbol{V} = \frac{\Gamma}{4\pi} \int \frac{d\boldsymbol{l} \times \boldsymbol{r}}{|\boldsymbol{r}|^3} d\boldsymbol{l} \tag{3.9}$$

This can be simplified using vector calculus. A linear vortex filament of finite length which is defined by the vector $\boldsymbol{r}_0 = \boldsymbol{r}_1 - \boldsymbol{r}_2$ induces the following velocity $\boldsymbol{V}$ at some point:

$$\boldsymbol{V} = \frac{\Gamma}{4\pi} \frac{\boldsymbol{r}_1 \times \boldsymbol{r}_2}{|\boldsymbol{r}_1 \times \boldsymbol{r}_2|^2} \left[\boldsymbol{r}_0 \cdot \left(\frac{\boldsymbol{r}_1}{|\boldsymbol{r}_1|} - \frac{\boldsymbol{r}_2}{|\boldsymbol{r}_2|} \right) \right] \tag{3.10}$$

where $\boldsymbol{r}_1$ and $\boldsymbol{r}_2$ are the vectors defined by each end of the vortex filament relative to the point of interest P_0. This equation can obviously become numerically unstable for small values of $|\boldsymbol{r}_1|$, $|\boldsymbol{r}_2|$, and $|\boldsymbol{r}_1 \times \boldsymbol{r}_2|^2$. Numerical singularities can be avoided by forcing the induced velocity $\boldsymbol{V}$ to be zero when $|\boldsymbol{r}_2|$, and $|\boldsymbol{r}_1 \times \boldsymbol{r}_2|^2$ are below some threshold ϵ. However, this can still lead to unrealistic velocity profiles near the vortex line. Consider the example of a closed vortex loop of width 1 m and circulation strength Γ, a representation of which can be seen in Figure 3.2a, and whose downwash profile can be seen in Figure 3.2b.

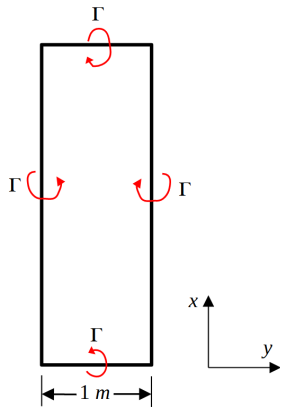

(a) Closed vortex loop of width 1 m

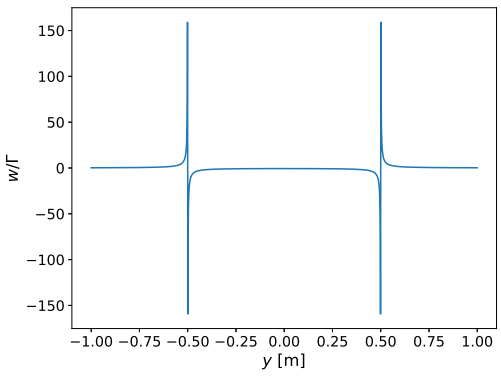

(b) Normalized downwash profile

Figure 3.2: Typical Biot-Savart vortex loop and its downwash profile at $z = 0$ m.

The downwash velocities in Figure 3.2b are normalized by the circulation strength Γ. It can clearly be seen in Figure 3.2b that close to the vortex line element at ± 0.5 m, there is a large spike in upwash and downwash on either side of the vortex line elements, leading to non-physical velocities and non-physical velocity derivatives. In order to avoid this, a limit of 1.1 is placed on the induced normalized velocity of each vortex element. This leads to the downwash profile presented in Figure 3.3.

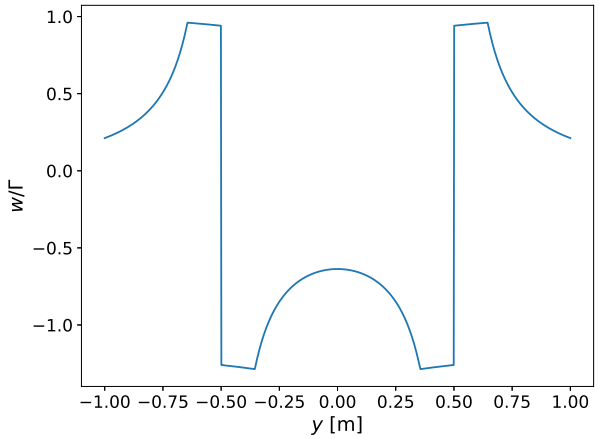

Figure 3.3: Normalized downwash profile of the modified Biot-Savart vortex at $z = 0.0$ m.

By placing this limit on the total induced velocity, a vortex core diameter of roughly 0.3 m is imposed and non-physical flow behaviour is comparatively limited. The effect the finite vortex core diameter has on downwash and sidewash profiles at other vertical separations can be seen in Figures 3.4 through 3.7.

Figure 3.4 shows the standard Biot-Savart vortex downwash and sidewash profile at a vertical height of 0.01 m underneath the vortex ring, and Figure 3.5 shows the downwash and sidewash profile of the modified vortex at the same height. The sharp velocity peaks of the Biot-Savart vortex have been smoothed in the modified vortex, and the maximum velocity of the sidewash has been significanly reduced from a normalized velocity of 15 m/s per unit circulation strength to 1.1 m/s per unit circulation strength. Within a full vortex lattice code, this has the effect of reducing numerical instabilities when vortex lines from a lifting surface lie too closely to the collocation points of other surfaces (or aircraft) without affecting the lift distribution on panels, as long as the panels are sufficiently large.

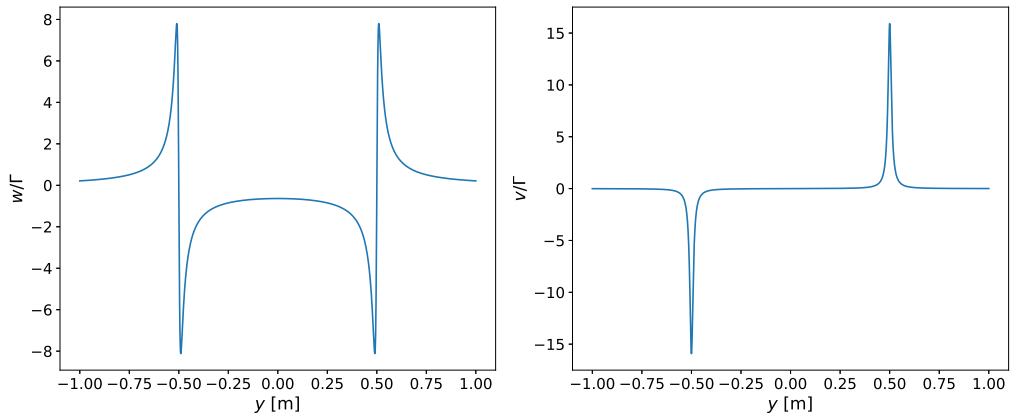

(a) Normalized downwash profile (b) Normalized sidewash profile

Figure 3.4: Normalized wake profiles of the standard Biot-Savart vortex at $z = 0.01$ m.

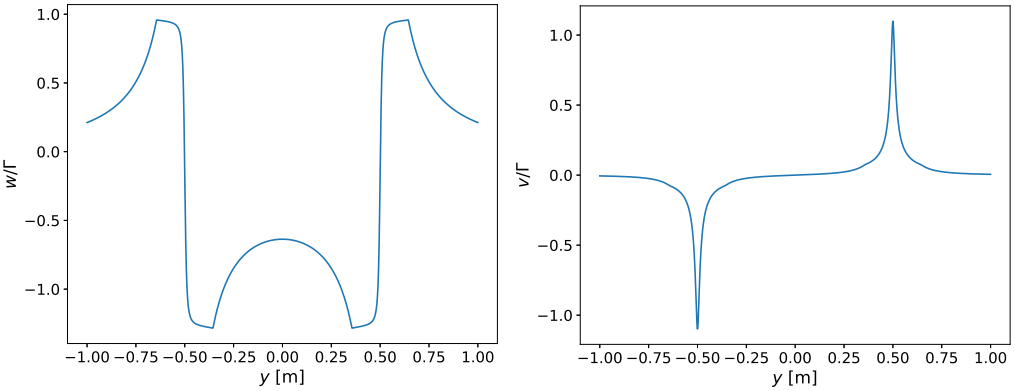

(a) Normalized downwash profile (b) Normalized sidewash profile

Figure 3.5: Normalized wake profiles of the modified Biot-Savart vortex at $z = 0.01$ m

Figure 3.6 shows the standard Biot-Savart vortex downwash and sidewash profile at a vertical height of 0.1 m underneath the vortex ring, and Figure 3.7 shows the downwash and sidewash profile of the modified vortex at the same height. Comparing Figure 3.6 and Figure 3.7, it can be seen that at the vertical separation of $z = -0.1$ m, there is very little difference in the downwash and sidewash profiles of the Biot-Savart and modified vortices. The downwash profiles

are nearly identical, and the sidewash profile maximum velocity has been reduced from 1.5 m/s per unit circulation strength to 1.1 m/s per unit circulation strength.

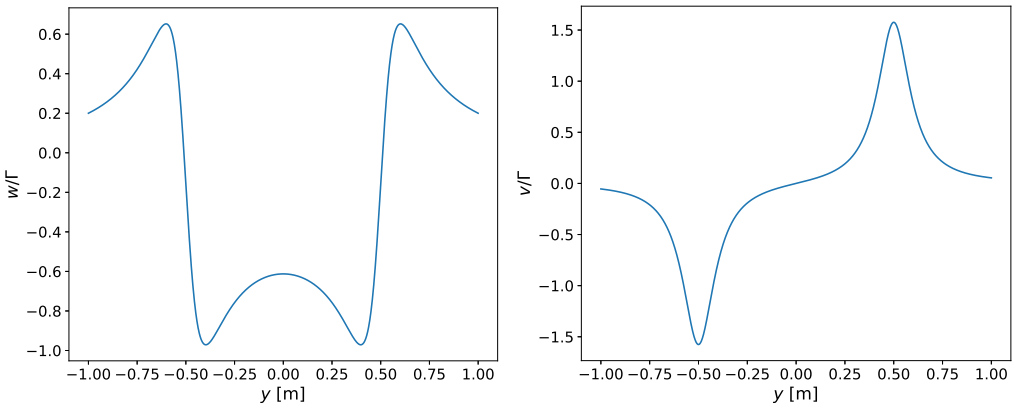

(a) Normalized downwash profile (b) Normalized sidewash profile

Figure 3.6: Normalized wake profiles of the standard Biot-Savart vortex at $z = 0.1$ m.

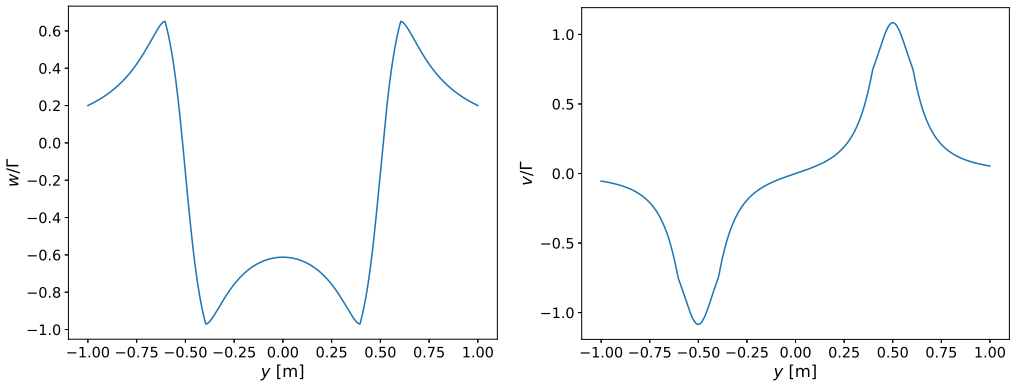

(a) Normalized downwash profile (b) Normalized sidewash profile

Figure 3.7: Normalized wake profiles of the modified Biot-Savart vortex at $z = 0.1$ m

3.1.2 Vortex Panel Method

Lifting surfaces of the tanker and receiver aircraft are modelled using quadrilateral elements constructed from vortex line elements. Each vortex panel is associated with some vortex circulation strength (Γ), which are proportional to the lift generated by each panel. These circulation strengths can be calculated using certain boundary conditions, the above vector calculus relation in Equation 3.10, and linear algebra. Furthermore, despite the assumption of incompressibility inherent to potential flow theory, the Prandtl-Glauert correction is used to extend the range of Mach numbers at which the code can produce valid results to $Ma_\infty = 0.7$, at speeds below which most AAR procedures take place. The vortex panel code developed for this work is based on that of Katz and Plotkin [55] and was programmed in *Python*. This is elaborated upon further using the schematic of a representative panel surface presented in Figure 3.8.

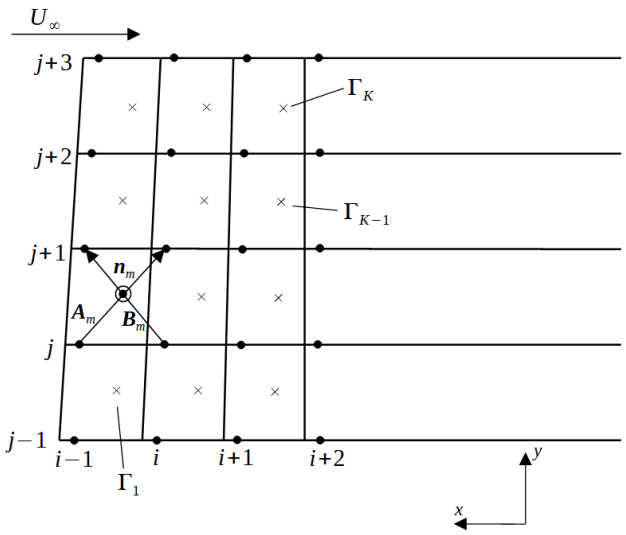

Figure 3.8: Array of wing and wake panel corner points. Airflow is moving in the $-x$ direction.

This vortex panel surface has K panels in total. Each vortex panel is made up of vortex line elements whose vertices are defined by panel corner points ($\bullet$) that are indexed in the $-x$ direction with the index i and in the y direction with the index j. Each vortex panel is associated with some Γ, a panel collocation point ($\times$), and a normal vector $\boldsymbol{n}$ which is considered to originate at the collocation point. The direction of an example normal vector above, $\boldsymbol{n}_m$, is defined by cross-product of two vectors, $\boldsymbol{A}_m$ and $\boldsymbol{B}_m$, which themselves are defined by the panel corner points

such that $\boldsymbol{A}_m$ extends from point $(i-1, j)$ to point $(i, j+1)$ and $\boldsymbol{B}_m$ extends from point (i, j) to $(i-1, j+1)$. Figure 3.8 also shows vortex lines extending in the $-x$ direction, which represent the prescribed flat wake of the vortex panel system extending from the trailing edges into the farfield. The circulation strength of the flat wake vortex line elements are equal to those of the panels to which they are attached.

The Γ values are calculated by ascribing the boundary condition that the net flow through each panel at its collocation point must be 0. This is done by calculating the aerodynamic influence coefficients (AIC) of each panel. The aerodynamic influence of panel ℓ on the collocation point of panel m (a_{ml}) is given by the dot product

$$a_{m\ell} = (u_{\text{ind}}, v_{\text{ind}}, w_{\text{ind}})_{m\ell} \cdot \boldsymbol{n}_m \tag{3.11}$$

where $(u_{\text{ind}}, v_{\text{ind}}, w_{\text{ind}})_{ml}$ are the x, y, and z velocity components induced by vortex ring l at the collocation point of panel m. (Note that the coordinate systems used to define $(u_{\text{ind}}, v_{\text{ind}}, w_{\text{ind}})_{ml}$ and $\boldsymbol{n}_m$ are not important as long as they are the same.) The influence of each ring vortex on each collocation point must be added. For a single collection of vortex panels, and assuming that the only external flow is the freestream velocity $\boldsymbol{U}_\infty$, at some collocation point m, the total influence from all K vortex rings must be such that

$$\sum_{l=1}^{K} a_{ml}\Gamma_l = -\boldsymbol{U}_\infty \cdot \boldsymbol{n}_m \tag{3.12}$$

which is to say that the velocity induced by every vortex panel at each collocation point must be equal and opposite to the freestream velocity component which is parallel to the panel's normal vector. A system of equations known as the AIC matrix is populated by influence coefficients of each vortex ring at each collocation point using the above boundary condition. A full vortex panel system with K vortex rings and collocation points can be represented in matrix form as follows:

$$\begin{bmatrix} a_{11} & a_{12} & a_{13} & \dots & a_{1K} \\ a_{21} & a_{22} & a_{23} & \dots & a_{2K} \\ \vdots & \vdots & \vdots & \ddots & \vdots \\ a_{K1} & a_{K2} & a_{K3} & \dots & a_{KK} \end{bmatrix} \begin{bmatrix} \Gamma_1 \\ \Gamma_2 \\ \vdots \\ \Gamma_K \end{bmatrix} = \begin{bmatrix} -\boldsymbol{U}_\infty \cdot \boldsymbol{n}_1 \\ -\boldsymbol{U}_\infty \cdot \boldsymbol{n}_2 \\ \vdots \\ -\boldsymbol{U}_\infty \cdot \boldsymbol{n}_K \end{bmatrix} \tag{3.13}$$

By denoting the vector on the right hand side of the equation as RHS, Equation 3.13 can be represented as:

$$\text{AIC}\,\Gamma = RHS \tag{3.14}$$

For a simple vortex lattice system, the circulation strengths Γ are found by inverting the AIC matrix. These Γ terms are then proportional to the lift generated by each panel, and the Γ corresponding to the wake vortex elements are proportional to the air velocities in the wake. By either adjusting the direction of the normal vectors of the tanker vortex panel system, or by changing the direction of the freestream vector in a way analogous to changing the aircraft's angle of attack, a solution of vortex ring strengths can be found such that the total lift generated is equal to the presumed weight of the aircraft that the vortex panel system is representing.

The force generated by each individual vortex panel on the leading edge of a surface is found using Equation 3.15 for leading edge panels:

$$\Delta F_m = (\rho U_\infty \Gamma_m \Delta y_m)/\beta_{PG}^2 \tag{3.15}$$

where Δy_m is the spanwise width of panel m. Additionally, a Prandtl-Glauert correction factor (β_{PG}) is applied when calculating lift, where $\beta_{PG} = \sqrt{1 - \mathrm{Ma}_\infty^2}$. A full Prandtl-Glauert correction would require stretching the geometry of the vortex panel system. However, in this case the calculated forces are simply scaled by $1/\beta_{PG}$, which is a valid approach up until Ma = 0.7. The lift generated by non-leading edge panels is proportional to the difference in Γ between the panel and the panel directly in front of it as shown in Equation 3.16.

$$\Delta F_m = \rho U_\infty (\Gamma_m - \Gamma_{m-N}) \Delta y_m / \beta_{PG}^2 \tag{3.16}$$

where N is the total number of spanwise panels for the surface in question and the $m - N$ is the index of the upstream neighbour of panel m. The induced drag, normal force, and lift force are then calculated through the projection of ΔF_m into the x, y, and z directions respectively.

$$[\Delta D_m, \Delta Y_m, \Delta L_m] = [\Delta F_m \cdot \hat{\boldsymbol{x}}, \Delta F_m \cdot \hat{\boldsymbol{y}}, \Delta F_m \cdot \hat{\boldsymbol{z}}] \tag{3.17}$$

Once the vortex ring strengths for the tanker have been calculated, they can then be used to predict air velocities in the wake of the aircraft. For the case of a vortex panel system representing a receiver in the wake of a tanker, the wake velocities at each collocation point are then added to the freestream velocity vector in the RHS of the receiver vortex panel method equation as shown in Equation 3.18.

$$\begin{bmatrix} a_{11} & a_{12} & a_{13} & \dots & a_{1K} \\ a_{21} & a_{22} & a_{23} & \dots & a_{2K} \\ \vdots & \vdots & \vdots & \ddots & \vdots \\ a_{K1} & a_{K2} & a_{K3} & \dots & a_{KK} \end{bmatrix} \begin{bmatrix} \Gamma_1 \\ \Gamma_2 \\ \vdots \\ \Gamma_K \end{bmatrix} = \begin{bmatrix} -(\boldsymbol{U}_\infty + \boldsymbol{U}_{\text{wake}}) \cdot \boldsymbol{n}_1 \\ -(\boldsymbol{U}_\infty + \boldsymbol{U}_{\text{wake}}) \cdot \boldsymbol{n}_2 \\ \vdots \\ -(\boldsymbol{U}_\infty + \boldsymbol{U}_{\text{wake}}) \cdot \boldsymbol{n}_K \end{bmatrix} \tag{3.18}$$

where the $\boldsymbol{U}_{\text{wake}}$ term consists of the air velocities in the tanker wake. Simple jet effects from the tanker are added to the term $\boldsymbol{U}_{\text{wake}}$ are included by assuming a streamtube of fixed radius emanating from the engines, inside of which is a fixed jet velocity. Having calculated the lift generated by each vortex panel, the vector $\boldsymbol{r}_j$ is defined as the vector from the aircraft's presumed centre of gravity (CG) to the collocation point of panel j. From this, the individual contribution of any panel j to the aircraft's rolling moment l, pitching moment m, and yawing moment n can be calculated as follows:

$$[l, m, n]_j = (\Delta F_j \boldsymbol{n}_j \times \boldsymbol{r}_j) \tag{3.19}$$

The total moment being imposed on the aircraft can be found by summing the contribution of all K panels.

$$[l, m, n] = \sum_{j=1}^{K} \Delta F_j \boldsymbol{n}_j \times \boldsymbol{r}_j \tag{3.20}$$

These moments can be converted into moment coefficients using the normalizations shown in Equations 3.21 through 3.23:

$$C_l = \frac{l}{\bar{q} S b} \tag{3.21}$$

$$C_m = \frac{m}{\bar{q} S \bar{c}} \tag{3.22}$$

$$C_n = \frac{n}{\bar{q} S b} \tag{3.23}$$

where $\bar{q}$ is the freestream dynamic pressure.

3.1.3 Propwash Model

Propulsion effects from propwash are accounted for using the closed-form actuator disk model first demonstrated by Conway [56], the use of which has been demonstrated in various panel codes including those of Droandi and Gibertini [57] and Alba *et al.* [58]. The flowfield induced by the actuator disk is defined by Equations 3.24 and 3.25 for $V_x(r, x)$, the velocity in the streamwise direction, and Equation 3.26 for $V_r(r, x)$, the velocity in the radial direction. In this formulation, R is the propeller radius, r is a radial coordinate (0 along the propeller axis), and x is the axial coordinate.

$$V_x(r, 0) = \frac{V_{x_0}}{R} \sqrt{R^2 - r^2} \tag{3.24}$$

$$V_x(r,x) = 2V_x(r,0) + V_{x_0}\left(-a + \frac{x}{R}\arcsin\left[\frac{2R}{\sqrt{x^2+(R+r)^2}+\sqrt{x^2+(R^2-r^2)}}\right]\right) \tag{3.25}$$

$$V_r(r,x) = \frac{V_{x_0}|x|}{2r}\left(\frac{1}{a}-a\right) - \frac{V_{x_0}r}{2R}\arcsin\left[\frac{2R}{\sqrt{x^2+(R+r)^2}+\sqrt{x^2+(R^2-r^2)}}\right] \tag{3.26}$$

where a is defined as follows:

$$a = \sqrt{\frac{\sqrt{(R^2-r^2-x^2)^2+4R^2x^2}+R^2-r^2-x^2}{2R^2}} \tag{3.27}$$

For use within the VLM code, the global coordinates of a point of interest (a vortex panel collocation point, for example) are converted into the local coordinates of each propeller, and these axial and radial velocities are added to determine the total propwash effect at this point. A typical example of nearfield propulsion swirl from this model can be seen in Figure 3.9, which depicts the swirl caused by the C-130's propellers, all of which rotate in the same counter-clockwise direction.

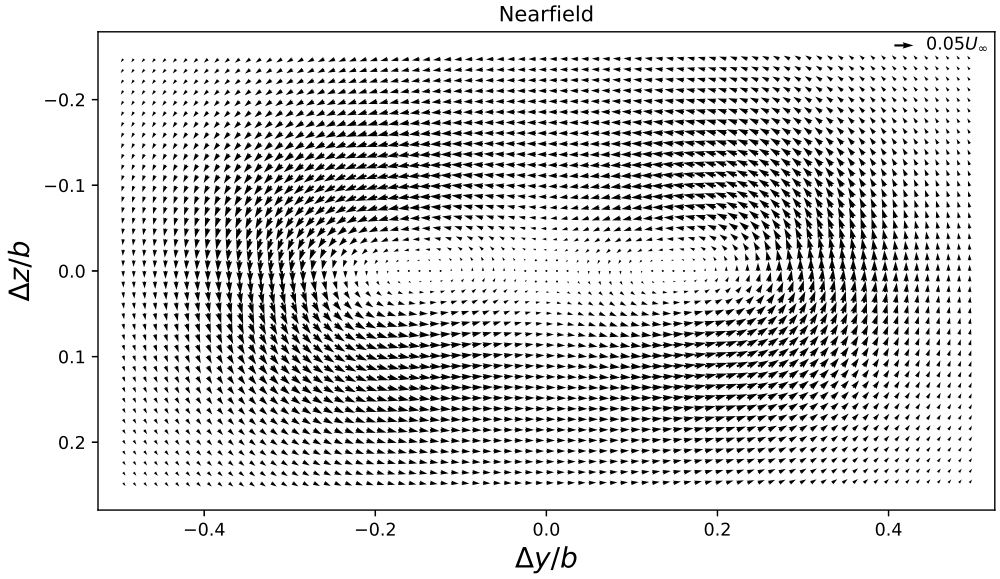

Figure 3.9: Propeller swirl of a C-130 Hercules, $U_\infty = 94.6$ m/s.

Jetwash Model

In cases where jetwash rather than propwash is relevant, a simple "streamtube" model is used in which circular areas of interest within the wake are identified. Within these areas, a fixed jetwash velocity is assumed and added to the overall velocities in the wake. The development of a more detailed jetwash model was explored, but not implemented due to the requirement of a complex integration and discretized spatial grid within the VLM. A detailed discussion of the explored jetwash model can be found in Appendix A.

3.2 Wake Model Validation

This section presents validation of the tanker wake velocities produced by the vortex panel/actuator disk model of a C-130 Hercules. Vicroy *et al.* [59] published flight test data in which a C-130 Hercules with a mass of approximately 45000 kg, and flying at an altitude of 1525 m (5000 ft) with a speed of Mach 0.28 was used as a wake generator. The induced wake velocity was measured by an OV-10 aircraft flying approximately 450 m behind the C-130 aircraft. The vortex panel representation of the Hercules aircraft will be identical to the dimensions published by Bloy and Trochadilis [10], with a flat wake and no simulated wake roll-up or free wake elements. This VLM geometry used can be seen in Figure 3.10.

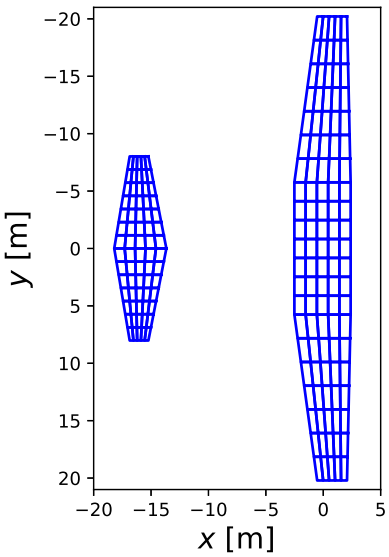

Figure 3.10: Vortex panel representation of the C-130 model used in this work. Airflow is moving in the $-x$ direction.

The CG of the C-130 was assumed to be aligned with the centre line at $0.15\bar{c}$. The C-130 was assumed to be in steady level flight such that the lift is equal to the weight and the pitching moment is 0, which is represented mathematically as:

$$L_t = W_t \qquad \text{and} \qquad m_t = 0 \tag{3.28}$$

A comparison of the C-130 Hercules wake measured during flight tests, and the wake generated by a vortex panel method can be seen in Figure 3.11. The velocities are normalized to the freestream velocity of 94.6 m/s (310.4 ft/s), and the Δy axis is normalized by the C-130's wingspan of 40.42 m (132 ft, 7 in.).

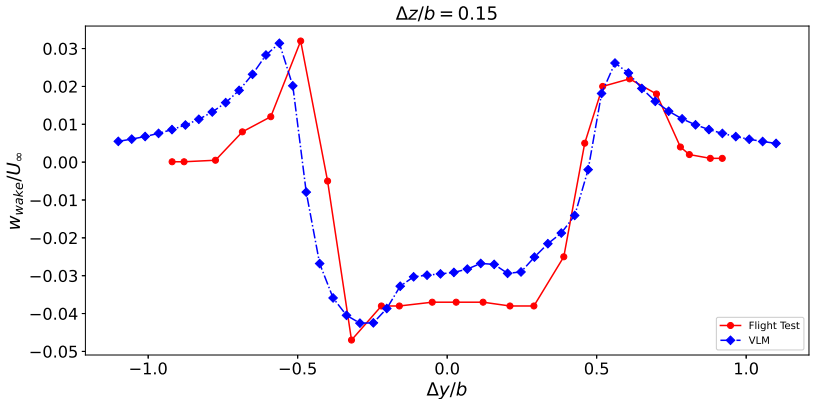

Figure 3.11: Downwash profile of a C-130 Hercules flying at 5000 ft, Ma = 0.28

The downwash profiles demonstrate similar trends. The magnitude of the maximum downwash velocity and the upwash velocity at $\Delta y/b = 0.6$ are very closely aligned, and addition of the propulsion model appears to capture the asymmetry about $\Delta y/b = 0.0$ in the downwash velocities, something that was in the flight test data. At all points between $\Delta y/b = \pm 0.4$, the magnitude of the discrepancies is less than 1% of U_∞.

The greatest discrepancies between the downwash profiles can be seen in the upwash values outboard of the wingtips at $\pm 0.5 \Delta y/b$. In this area, the upwash calculated using the VLM does not decay as rapidly with increasing lateral offset when compared to the flight test data. A plausible cause for this are viscous effects that are not modelled in the VLM. These include vortex decay or increases to vortex core radius with time. Atmospheric effects otherwise unaccounted for are also a possible source of uncertainty. As the wake measurements were conducted approximately 450 m behind the C-130 during the flight test, it is expected that viscous effects would start to become significant in this area of the farfield. A discrepancy in the location of the upwash peak of $\Delta y/b = -0.5$ can also be seen,

with the modeled upwash peak appearing a distance of $\Delta y/b = 0.1$ outboard of the upwash peak measured by the flight test. This could simply be a function of wake roll-up, or a measurement wake encounter that was not completely perpendicular to the wake, as we expect the wake profile to have their upwash peaks in near-symmetric locations about $\Delta y/b = 0$ in an idealized environment.

Figure 3.12 shows the sidewash profile for the same C-130 VLM model and its comparison to the flight test data.

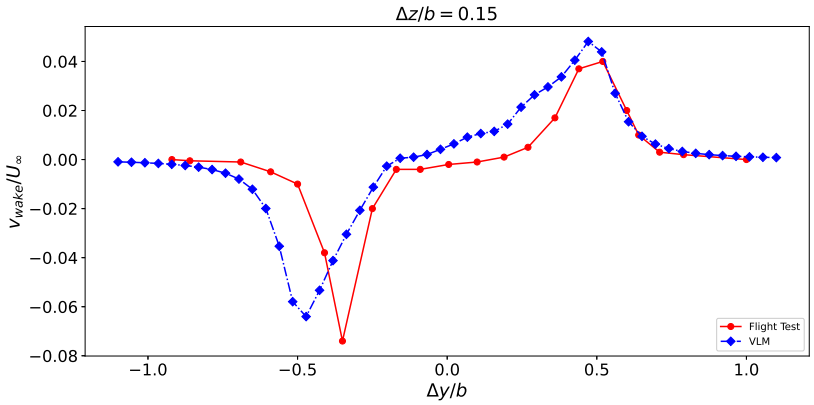

Figure 3.12: Sidewash profile of a C-130 Hercules flying at 5000 ft, Ma = 0.28

Similar asymmetries exist in the flight test data for sidewash data as in the downwash data evidenced in Figure 3.11. The VLM data also reproduce this asymmetric trend, although it is much less pronounced. Additionally, the flight test sidewash velocities tend towards 0 about between $\Delta y/b = -0.25$ and $\Delta y/b = 0.25$ whereas the VLM sidewash velocities tend to show an approximately constant gradient with respect to Δy between $\Delta y/b = -0.25$ and $\Delta y/b = 0.25$. The location at which the sidewash velocities begin to increase more rapidly is consistent between both the flight test and VLM data, however. Also similar to the downwash data is the sidewash peak near $\Delta y/b = -0.5$ appearing a distance of $\Delta y/b = 0.1$ outboard of the peak in the flight test data, which again is likely an effect of vortex drift. Finally, it can be seen that the magnitude of the sidewash velocity peak near $\Delta y/b = -0.5$ is under-predicted by around 1.5% of U_∞, whereas the magnitude of the sidewash velocity peak near $\Delta y/b = 0.5$ is over-predicted by around 1.2% of U_∞. Together with the systematic over-prediction of positive sidewash velocities, this could be evidence of an unaccounted-for wind gust or other minor atmospheric disturbance during the flight test, which added some small but measurable negative value to the sidewash velocities, not captured in the VLM data.

Although the nature of collecting experimental data during a flight test can make obtaining data free of environmental artifacts very difficult, this validation is useful to show that the potential flow method with propwash effect does indeed capture the overall trends of the velocities in the wake, including the pronounced asymmetries about the tanker centreline. Propulsive effects being a likely cause of asymmetry is further supported by Figure 3.13 which shows the downwash profile of the C-130 in identical flight conditions, but without any propulsion effects.

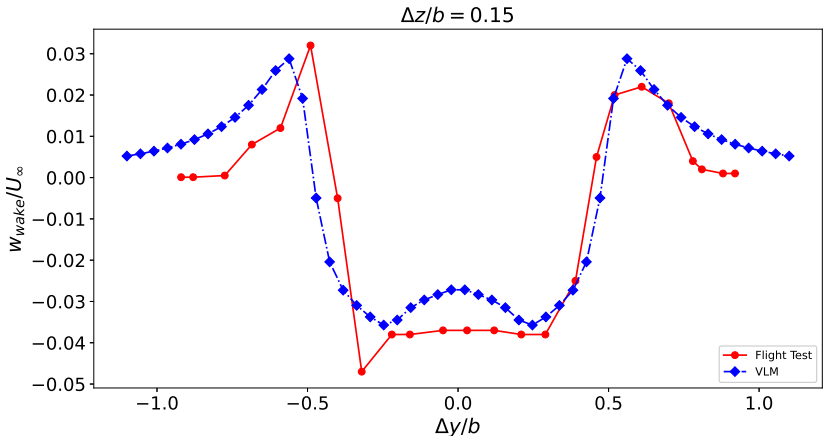

Figure 3.13: Downwash profile without propulsion effects of a C-130 Hercules flying at 5000 ft, Ma = 0.28.

As demonstrated in Figure 3.13, the downwash profile without the propulsion effects is symmetrical about $\Delta y/b = 0$, which strongly suggests that the propulsive effects are the main source of asymmetry in the wake velocities.

In general, the absolute error between the flight tests and model is less than 1% of U_∞ in the areas which are relevant for AAR. However, this methodology should still only be considered appropriate for near-field analysis, as viscous effects and wake roll-up are not considered, and will become non-negligible considerations as the distance between tanker and receiver increases.

3.3 Aircraft Model Validation

NASA flight test data published by Hansen and Cobleigh [60] is used below to further validate the wake model, and evaluate the VLM's ability to calculate moments and forces on an aircraft flying in the wake that's generated. Hansen and Cobleigh performed multiple flight tests consisting of two F/A-18 aircraft flying

in formation at various longitudinal, lateral, and vertical separations in order to investigate the effect of wingtip vortices on a trailing aircraft flying in close formation flight. The data collected at Mach 0.56 at an altitude of 25 000 ft with 55 ft (16.75 m) of nose-to-tail separation between the aircraft is of particular interest, since this is a nominal AAR flight condition for a small fighter aircraft, and the aircraft were close enough to be considered within the nearfield before wake roll-up effects become significant.

The VLM breakpoints used to model the F/A-18 are given in Appendix B. The vortex panel representation generated from this geometry can be seen in Figure 3.14. For the validation calculation, the F/A-18 models consisted of 52 vortex panels each.

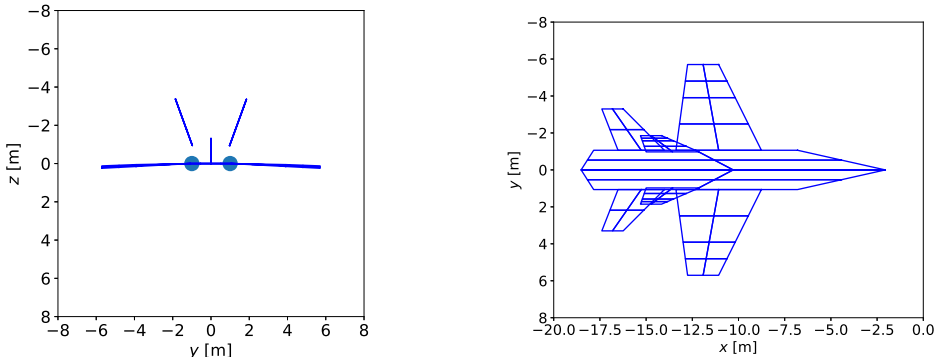

(a) F/A-18 model in the yz-plane

(b) F/A-18 model in the xy-plane

Figure 3.14: VLM representation of an F/A-18. Airflow is moving in the $-x$ direction.

The data collected and published by Hansen and Cobleigh are organized based on vertical distance between aircraft and the percentage of wing overlap as a percentage of the wingspan ($b = 11.4$m). Figure 3.15 shows a visual representation of the percentage of wing overlap. A wing overlap of 50% means that the nose of the trailing aircraft is aligned with the right wingtip of the lead aircraft. A wing overlap of 0% means that the left wingtip of the trailing aircraft is aligned with the right wingtip of the lead aircraft. A negative wing overlap means there is separation between the left wingtip of the trailing aircraft and the right wingtip of the lead aircraft. This separation distance is also expressed as a percentage of the wingspan.

The vertical separations of interest are $\Delta z = 2.85$ m ($0.25b$), $\Delta z = 4.28$ m ($0.375b$), and $\Delta z = 5.7$ m ($0.50b$). In order to perform these calculations, the wake from a trimmed F/A-18 model was generated. Then a second F/A-18 model was

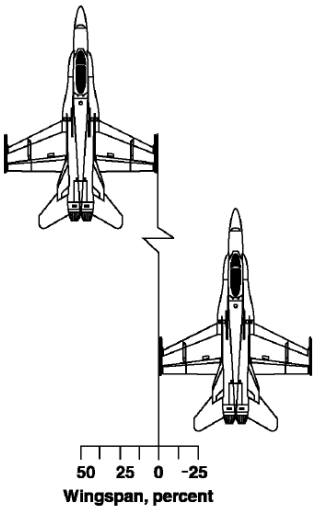

Figure 3.15: Relative lateral position as a percentage of wingspan overlap. (Adapted from Ref. [60])

placed in the wake, the wake velocities calculated over the vortex panels, and the effect in terms of induced rolling moment and induced pitching moment compared to the pitching and rolling moment in free air was calculated. The induced rolling moment at various lateral and vertical separations can be seen in Figure 3.16 and the induced pitching moment at various lateral and vertical separations can be seen in Figure 3.17.

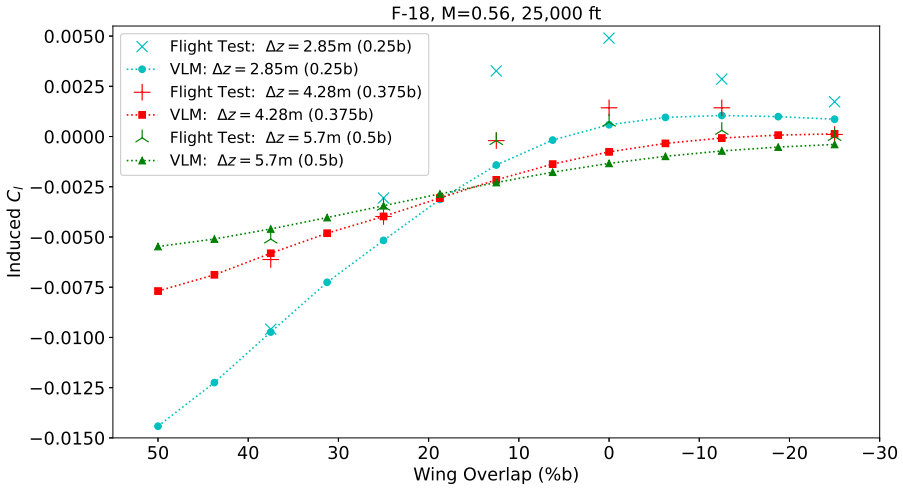

Figure 3.16: Induced rolling moment on a trailing F/A-18 during formation flight. Lead aircraft: F/A-18, longitudinal separation: 55 ft nose-to-tail.

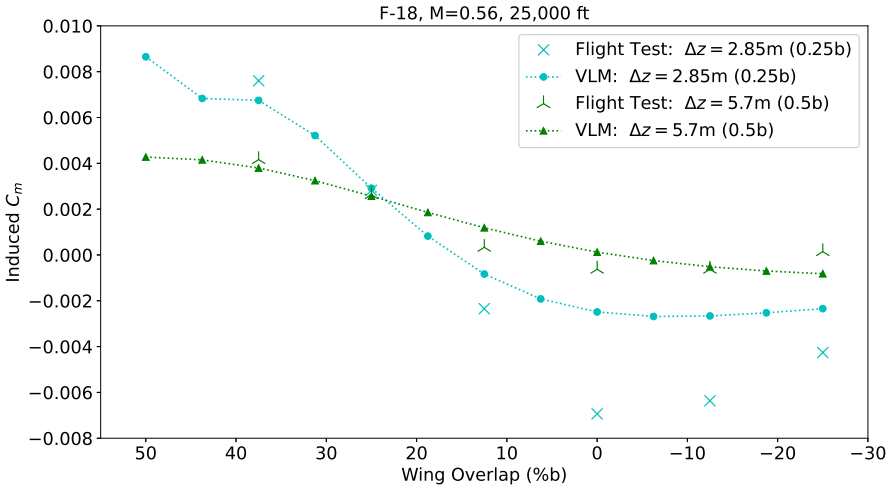

Figure 3.17: Induced pitching moment on a trailing F/A-18 during formation flight. Lead aircraft: F/A-18, longitudinal separation: 55 ft nose-to-tail.

For all vertical separations examined, the VLM and the flight test data generally show good agreement in terms of the magnitude of the induced rolling moment at wing overlaps from 50% to roughly 20%. Outboard of 20% wing overlap, the VLM tends to significantly under-predict the magnitude of the rolling moment. This is likely caused by an over-prediction of upwash velocities, as also seen in Figure 3.11. The magnitude of the induced rolling moment is a function of the downwash gradient across the entire wing span. If the upwash velocities are being overpredicted, then the upwash gradient is being under-predicted, leading to an under-prediction of the induced rolling moment. The poor prediction of these upwash velocities and its subsequent effect on induced rolling moment could be caused by the wake roll-up not being taken into account.

In Figure 3.17, the calculated induced pitching moment at a vertical separation of $\Delta z = 5.7$ m $(0.50b)$ shows good agreement with the flight test data at all lateral separations examined. However at $\Delta z = 2.85$ m $(0.25b)$, the induced pitching moment is once again under-predicted for lateral separations greater than 20% wing overlap. Unlike in the case of the rolling moment, it is not clear how an over-estimation of upwash velocities would lead to an underestimation of negative (nose-down) pitching moment. Flying in an area of upwash leads to an increase in apparent angle-of-attack. For an aircraft that has a negative $C_{m,\alpha}$ curve, this increase in angle of attack should lead to a negative pitching moment, with larger upwash velocities leading to larger negative pitching moments. The large deviation in the upwash region may simply be an artifact from the flight test

data collection process, or it might be indicative of some larger modeling error in the VLM. Ultimately, despite inaccurate predictions in the regions of upwash in the wake, the VLM performs well in terms of both estimating wake velocities, and evaluating their effect on a trailing aircraft in the regions of interest where downwash effects dominate *i.e.* within the wingspan of a lead aircraft or tanker.

3.4 Calculation of Positional Stability Using Coupled Sensitivities

Blake and Gingras discuss positional stability as an important aspect of close formation flight, such as is typical during the AAR task. Positional stability refers to the tendency of the receiver aircraft to return to its original position relative to the tanker when disturbed [32]. For the receiver to be positionally stable relative to the tanker in the longitudinal axis, increase in vertical separation between tanker and receiver will result in the receiver experiencing a positive (nose-up) pitching moment and an increase in lift. This is expressed mathematically as follows:

$$\frac{\partial C_L}{\partial \Delta z} > 0 \qquad \text{and} \qquad \frac{\partial C_m}{\partial \Delta z} > 0$$

Similarly, for the tanker to be positionally stable in the lateral-directional axis, an increase in lateral separation between the tanker and the receiver should result in a rolling moment and yawing moment that counteracts the movement of the receiver. This is expressed mathematically as

$$\frac{\partial C_l}{\partial \Delta y} < 0 \qquad \text{and} \qquad \frac{\partial C_n}{\partial \Delta y} < 0$$

i.e. a rightward movement of the receiver relative to the tanker results in a left wing down rolling moment, and a nose left yawing moment. Note that the positional derivatives are expressed in terms of the separation between the aircraft Δz and Δy. This to make it clear that these quantities are based on movement of the receiver relative to the tanker, rather than a movement of the receiver in its own reference frame. An increase in Δz could be due a downwards movement of the receiver *or* an upwards movement of the tanker. Calculation of these positional stability quantities can be performed via a basic finite difference method, where the aerodynamic forces and moments the receiver experiences at two different positions are subtracted and divided by the distance between the positions compared. However, this calculation can be performed more efficiently by using the linear nature of the VLM's governing equations and applying the adjoint method

which is often used to perform sensitivity calculations during numerical optimization studies. This substantially reduces the calculation time required particularly in the case of a two-way coupled VLM calculations, where the receiver is assumed to also have some effect on the trim condition of the tanker.

To introduce this concept, first the calculation of sensitivities assuming one-way coupling will be derived in which it is assumed that only the tanker has an effect on the receiver. Following this, two-way coupled sensitivity analysis will be derived and demonstrated in a test case.

3.4.1 One-Way Coupled Sensitivity

In the case of a one-way coupled analysis, the steady level trim condition is first enforced on the tanker to calculate the representative flow field in the wake according to the free-body diagram seen in Figure 3.18.

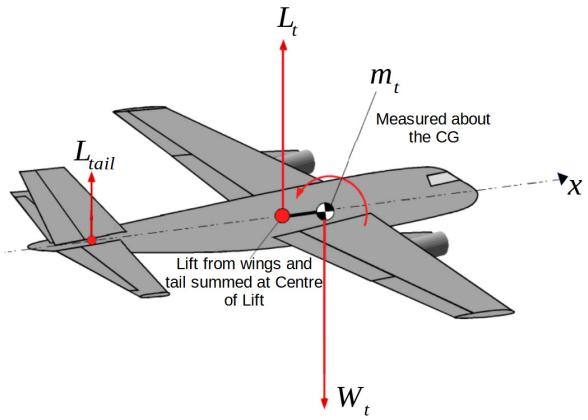

Figure 3.18: Free-body diagram for an aircraft at steady level flight in the longitudinal axis.

Recall the conditions

$$L_t = W_t \qquad \text{and} \qquad m_t = 0 \tag{3.29}$$

where the subscript $_t$ denotes the tanker. Recalling Equation 3.13, the condition that lift must be equal to weight is enforced by adjusting the angle of the tanker's normal vectors relative to the effective airflow, $\boldsymbol{U}_\infty$. The pitching moment is then further adjusted by changing the angle of the normal vectors corresponding to the tanker's elevators. This is a coupled problem with two equations and two unknowns, and can be expressed in terms of residual equations that must equal 0.

$$R_1(\alpha_t, \delta_{e_t}) = W_t - L_t(\alpha_t, \delta_{e_t}) = 0 \tag{3.30}$$

$$R_2(\alpha_t, \delta_{e_t}) = m_t(\alpha_t, \delta_{e_t}) = 0 \tag{3.31}$$

Both these residual equations are functions of the tanker's angle of attack, α_t, and elevator deflection, δ_{e_t}. These equations are solved using Newton's method. An initial α_t and δ_{e_t} are guessed, which produces a residual vector $R = [R_1, R_2]$. New values for α_t and δ_{e_t}, denoted by α_t^* and $\delta_{e_t}^*$ can then be determined by evaluating Equation 3.32.

$$\begin{bmatrix} \alpha_t^* \\ \delta_{e_t}^* \end{bmatrix} = \begin{bmatrix} \alpha_t \\ \delta_{e_t} \end{bmatrix} - \begin{bmatrix} \frac{\partial L_t}{\partial \alpha_t} & \frac{\partial L_t}{\partial \delta_{e_t}} \\ \frac{\partial m_t}{\partial \alpha_t} & \frac{\partial m_t}{\partial \delta_{e_t}} \end{bmatrix}^{-1} \begin{bmatrix} R_1 \\ R_2 \end{bmatrix} \tag{3.32}$$

This requires calculating the terms $\frac{\partial L_t}{\partial \alpha_t}$, $\frac{\partial L_t}{\partial \delta_{e_t}}$, $\frac{\partial m_t}{\partial \alpha_t}$, and $\frac{\partial m_t}{\partial \delta_{e_t}}$, which is done analytically by taking the derivative of the normal vector rotation matrices. For example, in two dimensions, in order to rotate a vector through some angle θ, multiply the vector by the Euler transformation shown in Equation 3.33.

$$[M_{rot}] = \begin{bmatrix} \cos\theta & -\sin\theta \\ \sin\theta & \cos\theta \end{bmatrix} \tag{3.33}$$

Therefore, to obtain the vector corresponding to the derivative with respect to the angle θ, the following rotation vector is used:

$$\begin{bmatrix} \frac{dM_{rot}}{d\theta} \end{bmatrix} = \begin{bmatrix} -\sin\theta & -\cos\theta \\ \cos\theta & -\sin\theta \end{bmatrix} \tag{3.34}$$

The rotation derivative matrix is then used to produce a different set of rotated vectors corresponding to the derivatives with respect to α_t and δ_{e_t} that are then used in Equation 3.13 such that

$$\begin{bmatrix} \partial\Gamma_1/\partial\alpha_t \\ \partial\Gamma_2/\partial\alpha_t \\ \vdots \\ \partial\Gamma_K/\partial\alpha_t \end{bmatrix} = \begin{bmatrix} a_{11} & a_{12} & a_{13} & \dots & a_{1K} \\ a_{21} & a_{22} & a_{23} & \dots & a_{2K} \\ \vdots & \vdots & \vdots & \ddots & \vdots \\ a_{K1} & a_{K2} & a_{K3} & \dots & a_{KK} \end{bmatrix}^{-1} \begin{bmatrix} -\boldsymbol{U}_\infty \cdot \partial \boldsymbol{n}_1/\partial\alpha_t \\ -\boldsymbol{U}_\infty \cdot \partial \boldsymbol{n}_2/\partial\alpha_t \\ \vdots \\ -\boldsymbol{U}_\infty \cdot \partial \boldsymbol{n}_K/\partial\alpha_t \end{bmatrix} \tag{3.35}$$

$$\begin{bmatrix} \partial\Gamma_1/\partial\delta_{e_t} \\ \partial\Gamma_2/\partial\delta_{e_t} \\ \vdots \\ \partial\Gamma_K/\partial\delta_{e_t} \end{bmatrix} = \begin{bmatrix} a_{11} & a_{12} & a_{13} & \dots & a_{1K} \\ a_{21} & a_{22} & a_{23} & \dots & a_{2K} \\ \vdots & \vdots & \vdots & \ddots & \vdots \\ a_{K1} & a_{K2} & a_{K3} & \dots & a_{KK} \end{bmatrix}^{-1} \begin{bmatrix} -\boldsymbol{U}_\infty \cdot \partial \boldsymbol{n}_1/\partial\delta_{e_t} \\ -\boldsymbol{U}_\infty \cdot \partial \boldsymbol{n}_2/\partial\delta_{e_t} \\ \vdots \\ -\boldsymbol{U}_\infty \cdot \partial \boldsymbol{n}_K/\partial\delta_{e_t} \end{bmatrix} \tag{3.36}$$

and the values of the $\frac{\partial L_t}{\partial \alpha_t}$, $\frac{\partial L_t}{\partial \delta_{e_t}}$, $\frac{\partial m_t}{\partial \alpha_t}$, and $\frac{\partial m_t}{\partial \delta_{e_t}}$ terms can be determined by using the $\frac{\partial \Gamma}{\partial \alpha_t}$ and $\frac{\partial \Gamma}{\partial \delta_{e_t}}$ vectors through Equations 3.15, 3.16, 3.17, and 3.20.

Once the tanker has been trimmed, the receiver can be trimmed with the addition of the $\boldsymbol{U}_{\text{wake}}$ terms in the RHS of Equation 3.18. It is often of interest to calculate the sensitivity of the receiver's lift, pitching moment, and rolling moment to its position in the wake of the tanker. To do this, the change in wake velocities with respect to position at each collocation point must be calculated, and then the associated change in the vortex circulation strengths, lift distribution, and induced moments can be found by a similar method to the above. For instance, to find the sensitivity of the receiver pitching moment to a change in vertical position z, the following system of linear equations could be solved for the $\frac{\partial \Gamma}{\partial \Delta z}$ terms:

$$\begin{bmatrix} \partial\Gamma_1/\partial\Delta z \\ \partial\Gamma_2/\partial\Delta z \\ \vdots \\ \partial\Gamma_K/\partial\Delta z \end{bmatrix} = \begin{bmatrix} a_{11} & a_{12} & a_{13} & \dots & a_{1K} \\ a_{21} & a_{22} & a_{23} & \dots & a_{2K} \\ \vdots & \vdots & \vdots & \ddots & \vdots \\ a_{K1} & a_{K2} & a_{K3} & \dots & a_{KK} \end{bmatrix}^{-1} \begin{bmatrix} -\partial \boldsymbol{U}_{\text{wake}}/\partial\Delta z \cdot \boldsymbol{n}_1 \\ -\partial \boldsymbol{U}_{\text{wake}}/\partial\Delta z \cdot \boldsymbol{n}_2 \\ \vdots \\ -\partial \boldsymbol{U}_{\text{wake}}/\partial\Delta z \cdot \boldsymbol{n}_K \end{bmatrix} \tag{3.37}$$

The $\frac{\partial \Gamma}{\partial \Delta z}$ terms can then be used to solve for all relevant sensitivities with respect to Δz. This process is identical when solving for sensitivities with respect to Δy. In order to damp numerical instabilities caused by collocation point proximity to wake vortex lines, a central differencing scheme is instituted to determine values of $\partial \boldsymbol{U}_{\text{wake}}/\partial\Delta z$ and $\partial \boldsymbol{U}_{\text{wake}}/\partial\Delta y$.

3.4.2 Two-Way Coupled Sensitivities

In this section, two-way coupling will be considered between the updraft effect of the receiver and the lift distribution and pitching moment of the tanker. In order to represent this, two new AIC matrices representing the coupling from between the tanker and receiver (AIC_{tr}) and the coupling between the receiver and tanker (AIC_{rt}) are used.

$$\text{AIC}_{tt}\Gamma_t + \text{AIC}_{tr}\Gamma_t = \text{RHS}_t \tag{3.38}$$

$$\text{AIC}_{rr}\Gamma_t + \text{AIC}_{rt}\Gamma_t = \text{RHS}_r \tag{3.39}$$

where the subscript t denotes the tanker and the subscript r denotes the receiver. The reason why the vortex panel systems are explicitly expressed separately is because the terms AIC_{tt} and AIC_{rr} are constant for a given aircraft geometry

and mesh. Therefore, in order to save computational time, they can be calculated once per simulation and only the aerodynamic coupling terms AIC_{tr} and AIC_{rt} must be calculated for every spatial offset between the aircraft.

Once again, it is assumed that steady level flight conditions exist so the total lift must be equal to the weight of each aircraft, and each aircraft must be trimmed in pitch. This is analogous to FBR, where the aerodynamic forces in the lateral-directional axis are assumed to be symmetrical and steady level flight can be achieved simply by trimming in the longitudinal axis. The trim equations in the longitudinal axis are given in Equations 3.40 through 3.43.

$$L_t = W_t \tag{3.40}$$

$$L_r = W_r \tag{3.41}$$

$$m_t = 0 \tag{3.42}$$

$$m_r = 0 \tag{3.43}$$

The pitching moment about the CG of each aircraft is changed by adjusting the angle of the normal vector of certain elevator panels. This deflection is expressed as δ_{e_t} and δ_{e_r}. Some dependence is assumed on the relative position of the aircraft, represented by the variable P_j. Thus the governing equations of the general aerodynamic system may be written in the form of the residual equations 3.44 through 3.49. The residual equations are numbered R_1 through R_6.

$$R_1(P_j, \boldsymbol{U_\infty}, \Gamma_t, \Gamma_r, \alpha_t, \delta_{e_t}) = \mathrm{AIC}_{tt} \cdot \Gamma_t + \mathrm{AIC}_{tr}(P_j) \cdot \Gamma_r - \mathrm{RHS}_t(\boldsymbol{U_\infty}, \alpha_t, \delta_{e_t}) = 0 \tag{3.44}$$

$$R_2(P_j, \boldsymbol{U_\infty}, \Gamma_t, \Gamma_r, \alpha_r, \delta_{e_r}) = \mathrm{AIC}_{rr} \cdot \Gamma_r + \mathrm{AIC}_{rt}(P_j) \cdot \Gamma_t - \mathrm{RHS}_r(\boldsymbol{U_\infty}, \alpha_r, \delta_{e_r}) = 0 \tag{3.45}$$

$$R_3(\alpha_t, \delta_{e_t}) = L_t(\alpha_t, \delta_{e_t}) - W_t = 0 \tag{3.46}$$

$$R_4(\alpha_r, \delta_{e_r}) = L_r(, \alpha_r, \delta_{e_r}) - W_r = 0 \tag{3.47}$$

$$R_5(\alpha_t, \delta_{e_t}) = m_t(\alpha_t, \delta_{e_t}) = 0 \tag{3.48}$$

$$R_6(\alpha_r, \delta_{e_r}) = m_r(\alpha_r, \delta_{e_r}) = 0 \tag{3.49}$$

3.4.3 Adjoint Formulation and Sensitivity Derivations

For a steady state analysis, the aerodynamic forces and moments of interest include lift (L), rolling moment (ℓ), pitching moment (m), yawing moment (n), and their respective coefficients C_L, C_ℓ, C_m, and C_n. Let any of these be represented by f. These forces and moments are functions of Γ, which are also dependent on the angles of attack (α), elevator deflections (δ_e), and the flight formation parameters such as Δx, Δy, and Δz represented by P_j. This makes P_j and $\boldsymbol{U}_\infty$ independent variables, and Γ, α, and δ_e state vectors (y_i). For this analysis, it is assumed that $\boldsymbol{U}_\infty$ is fixed. Since f is a function of both P_j and y_i, the sensitivity of f to the independent variables P_j can be determined by the chain rule in Equation 3.50.

$$\frac{df}{dP_j} = \frac{\partial f}{\partial y_i}\frac{dy_i}{dP_j} \tag{3.50}$$

In practice, evaluating the sensitivities dy_i/dP_j can be time consuming, and therefore the residual equations are useful. The derivatives of the generalized residual equations with respect to P_j can be written as follows:

$$\frac{dR_g}{dP_j} = \frac{\partial R_g}{\partial P_j} + \frac{\partial R_g}{\partial y_i}\frac{dy_i}{dP_j} = 0 \tag{3.51}$$

This formulation allows for the computation of the total sensitivity of state variables with respect to independent variables:

$$\frac{\partial R_g}{\partial y_i}\frac{dy_i}{dP_j} = -\frac{\partial R_g}{\partial P_j} \tag{3.52}$$

$$\frac{dy_i}{dP_j} = -\left[\frac{\partial R_g}{\partial y_i}\right]^{-1}\frac{\partial R_g}{\partial P_j} \tag{3.53}$$

Substituting Equation 3.53 into Equation 3.50 gives Equation 3.54.

$$\frac{df}{dP_j} = -\underbrace{\frac{\partial f}{\partial y_i}\left[\frac{\partial R_g}{\partial y_i}\right]^{-1}}_{-\lambda}\frac{\partial R_g}{\partial P_j} \tag{3.54}$$

The first two factors on the right hand side of Equation 3.54 is defined as the *adjoint vector* λ. It can be obtained by solving the following equation:

$$\frac{\partial R_g}{\partial y_i}\lambda_g = -\frac{\partial f}{\partial y_i} \tag{3.55}$$

This can be generalized to the whole system of equations as follows:

$$\begin{aligned}\frac{df}{dP_j} = &-\lambda_1^T\left(\frac{\partial R_1}{\partial P_j}\right) - \lambda_2^T\left(\frac{\partial R_2}{\partial P_j}\right) - \lambda_3^T\left(\frac{\partial R_3}{\partial P_j}\right) \\ &- \lambda_4^T\left(\frac{\partial R_4}{\partial P_j}\right) - \lambda_5^T\left(\frac{\partial R_5}{\partial P_j}\right) - -\lambda_6^T\left(\frac{\partial R_6}{\partial P_j}\right)\end{aligned} \tag{3.56}$$

where $\lambda = [\lambda_1\ \lambda_2\ \lambda_3\ \lambda_4\ \lambda_5\ \lambda_6]$ is determined from Equation 3.57.

$$\begin{bmatrix} \frac{\partial R_1}{\partial \Gamma_t} & \frac{\partial R_1}{\partial \Gamma_r} & \frac{\partial R_1}{\partial \alpha_t} & \frac{\partial R_1}{\partial \alpha_r} & \frac{\partial R_1}{\partial \delta_{e_t}} & \frac{\partial R_1}{\partial \delta_{e_r}} \\ \frac{\partial R_2}{\partial \Gamma_t} & \frac{\partial R_2}{\partial \Gamma_r} & \frac{\partial R_2}{\partial \alpha_t} & \frac{\partial R_2}{\partial \alpha_r} & \frac{\partial R_2}{\partial \delta_{e_t}} & \frac{\partial R_2}{\partial \delta_{e_r}} \\ \frac{\partial R_3}{\partial \Gamma_t} & \frac{\partial R_3}{\partial \Gamma_r} & \frac{\partial R_3}{\partial \alpha_t} & \frac{\partial R_3}{\partial \alpha_r} & \frac{\partial R_3}{\partial \delta_{e_t}} & \frac{\partial R_3}{\partial \delta_{e_r}} \\ \frac{\partial R_4}{\partial \Gamma_t} & \frac{\partial R_4}{\partial \Gamma_r} & \frac{\partial R_4}{\partial \alpha_t} & \frac{\partial R_4}{\partial \alpha_r} & \frac{\partial R_4}{\partial \delta_{e_t}} & \frac{\partial R_4}{\partial \delta_{e_r}} \\ \frac{\partial R_5}{\partial \Gamma_t} & \frac{\partial R_5}{\partial \Gamma_r} & \frac{\partial R_5}{\partial \alpha_t} & \frac{\partial R_5}{\partial \alpha_r} & \frac{\partial R_5}{\partial \delta_{e_t}} & \frac{\partial R_5}{\partial \delta_{e_r}} \\ \frac{\partial R_6}{\partial \Gamma_t} & \frac{\partial R_6}{\partial \Gamma_r} & \frac{\partial R_6}{\partial \alpha_t} & \frac{\partial R_6}{\partial \alpha_r} & \frac{\partial R_6}{\partial \delta_{e_t}} & \frac{\partial R_6}{\partial \delta_{e_r}} \end{bmatrix}^T \begin{bmatrix} \lambda_1 \\ \lambda_2 \\ \lambda_3 \\ \lambda_4 \\ \lambda_5 \\ \lambda_6 \end{bmatrix} = \begin{bmatrix} \frac{\partial f}{\partial \Gamma_t} \\ \frac{\partial f}{\partial \Gamma_r} \\ \frac{\partial f}{\partial \alpha_t} \\ \frac{\partial f}{\partial \alpha_r} \\ \frac{\partial f}{\partial \delta_{e_t}} \\ \frac{\partial f}{\partial \delta_{e_r}} \end{bmatrix} \tag{3.57}$$

The derivatives in the matrix shown in Equation 3.57 can be found analytically as shown presently. Recalling that RHS_t and RHS_r are equal to $-\boldsymbol{U}_\infty \cdot \boldsymbol{n_m}$, their derivative with respect to angle of attack and elevator deflection can be determined as follows:

$$\begin{aligned}\frac{\partial \text{RHS}}{\partial \alpha} &= [-U_\infty \sin(\alpha), 0, U_\infty \cos(\alpha)] \cdot \boldsymbol{n_m} \\ \frac{\partial \text{RHS}}{\partial \delta_e} &= [-U_\infty \sin(\delta_e), 0, U_\infty \cos(\delta_e)] \cdot \boldsymbol{n_{\delta_e}}\end{aligned} \tag{3.58}$$

Similarly, the derivative of the residuals with respect to Γ are just the AICs themselves resulting in the following:

$$\begin{aligned}&\frac{\partial R_1}{\partial \Gamma_t} = \text{AIC}_{tt}, \quad \frac{\partial R_1}{\partial \Gamma_r} = \text{AIC}_{tr}, \quad \frac{\partial R_1}{\partial \alpha_t} = \frac{\partial \text{RHS}_t}{\partial \alpha_t}, \quad \frac{\partial R_1}{\partial \delta_{e_t}} = \frac{\partial \text{RHS}_t}{\partial \delta_{e_t}} \\ &\frac{\partial R_2}{\partial \Gamma_t} = \text{AIC}_{rt}, \quad \frac{\partial R_2}{\partial \Gamma_r} = \text{AIC}_{rr}, \quad \frac{\partial R_2}{\partial \alpha_r} = \frac{\partial \text{RHS}_r}{\partial \alpha_r}, \quad \frac{\partial R_2}{\partial \delta_{e_r}} = \frac{\partial \text{RHS}_r}{\partial \delta_{e_r}}\end{aligned} \tag{3.59}$$

Other derivatives can be obtained using the above known derivatives from Equations 3.58 and 3.59, and the following theorems:

$$\begin{aligned}
\frac{\partial \Gamma_t}{\partial \alpha_t} &= \left[\frac{\partial R_1}{\partial \Gamma_t}\right]^{-1} \frac{\partial R_1}{\partial \alpha_t} = \mathrm{AIC}_{tt}^{-1} \frac{\partial \mathrm{RHS}_{\boldsymbol{t}}}{\partial \alpha_t} \\
\frac{\partial \Gamma_t}{\partial \alpha_r} &= \left[\frac{\partial R_2}{\partial \Gamma_t}\right]^{-1} \frac{\partial R_2}{\partial \alpha_r} = \mathrm{AIC}_{rr}^{-1} \frac{\partial \mathrm{RHS}_{\boldsymbol{r}}}{\partial \alpha_r} \\
\frac{\partial \Gamma_t}{\partial \delta_{e_t}} &= \left[\frac{\partial R_1}{\partial \Gamma_t}\right]^{-1} \frac{\partial R_1}{\partial \delta_{e_t}} = \mathrm{AIC}_{tt}^{-1} \frac{\partial \mathrm{RHS}_{\boldsymbol{t}}}{\partial \delta_{e_t}} \\
\frac{\partial \Gamma_t}{\partial \delta_{e_r}} &= \left[\frac{\partial R_2}{\partial \Gamma_t}\right]^{-1} \frac{\partial R_2}{\partial \delta_r} = \mathrm{AIC}_{rr}^{-1} \frac{\partial \mathrm{RHS}_{\boldsymbol{r}}}{\partial \delta_{e_r}}
\end{aligned} \tag{3.60}$$

The partial derivatives of R_3 with respect to the angles of attack of each aircraft are as follows:

$$\frac{\partial R_3}{\partial \alpha_t} = \frac{\partial L_t}{\partial \alpha_t} = L\left(\frac{\partial \Gamma_t}{\partial \alpha_t}\right) = L\left(\mathrm{AIC}_{tt}^{-1} \frac{\mathrm{RHS}_t}{\partial \alpha_t}\right) \tag{3.61}$$

$$\begin{aligned}
\frac{\partial R_3}{\partial \alpha_r} = \frac{\partial L_t}{\partial \alpha_r} = L\left(\frac{\partial \Gamma_t}{\partial \alpha_r}\right) &= L\left(\left[\frac{\partial R_1}{\partial \Gamma_t}\right]^{-1} \frac{\partial R_1}{\partial \Gamma_t} \left[\frac{\partial R_2}{\partial \Gamma_t}\right]^{-1} \frac{\partial R_2}{\partial \alpha_r}\right) \\
&= L\left(\mathrm{AIC}_{tt}^{-1}\left[\mathrm{AIC}_{rt}\left[\mathrm{AIC}_{rr}^{-1} \frac{-\mathrm{RHS}_r}{\partial \alpha_r}\right]\right]\right)
\end{aligned} \tag{3.62}$$

The partial derivative of R_3 with respect to tanker elevator deflection is:

$$\frac{\partial R_3}{\partial \delta_{e_t}} = \frac{\partial L_t}{\partial \delta_{e_t}} = L\left(\frac{\partial \Gamma_t}{\partial \delta_{e_t}}\right) = L\left(\mathrm{AIC}_{tt}^{-1} \frac{\mathrm{RHS}_t}{\partial \delta_{e_t}}\right) \tag{3.63}$$

The partial derivatives of R_4 with respect to the angles of attack of the each aircraft are as follows:

$$\begin{aligned}
\frac{\partial R_4}{\partial \alpha_t} = \frac{\partial L_r}{\partial \alpha_t} = L\left(\frac{\partial \Gamma_t}{\partial \alpha_t}\right) &= L\left(\left[\frac{\partial R_2}{\partial \Gamma_t}\right]^{-1} \frac{\partial R_2}{\partial \Gamma_t} \left[\frac{\partial R_1}{\partial \Gamma_t}\right]^{-1} \frac{-\partial R_1}{\partial \alpha_t}\right) \\
&= L\left(\mathrm{AIC}_{rr}^{-1}\left[\mathrm{AIC}_{tr}\left[\mathrm{AIC}_{tt}^{-1} \frac{-\mathrm{RHS}_t}{\partial \alpha_t}\right]\right]\right)
\end{aligned} \tag{3.64}$$

$$\frac{\partial R_4}{\partial \alpha_r} = \frac{\partial L_2}{\partial \alpha_r} = L\left(\frac{\partial \Gamma_t}{\partial \alpha_r}\right) = L\left(\mathrm{AIC}_{rr}^{-1} \frac{\mathrm{RHS}_r}{\partial \alpha_r}\right) \tag{3.65}$$

The partial derivative of R_4 with respect to receiver elevator deflection is:

$$\frac{\partial R_4}{\partial \delta_{e_r}} = \frac{\partial L_r}{\partial \delta_{e_r}} = L\left(\frac{\partial \Gamma_r}{\partial \delta_{e_r}}\right) = L\left(\mathrm{AIC}_{rr}^{-1}\frac{\mathrm{RHS}_r}{\partial \delta_{e_r}}\right) \tag{3.66}$$

For functions of interest such as moments (which are functions of lift and the length of the moment arm), the derivatives with respect to vortex circulation strength are linear. Their derivative will simply be the length of the moment arm at which the change in lift, dL, is applied. This makes determination of the derivatives with respect to m analogous to determining the derivatives with respect to L. The partial derivatives of R_5 are calculated as follows:

$$\frac{\partial R_5}{\partial \Gamma_t^k} = \frac{\partial m_t}{\partial \Gamma_t^k} = m\left(\frac{\partial \Gamma_t}{\partial \Gamma_t^k}\right)$$

$$\frac{\partial R_5}{\partial \alpha_t} = \frac{\partial m_t}{\partial \alpha_t} = m\left(\frac{\partial \Gamma_t}{\partial \alpha_1}\right) = m\left(\mathrm{AIC}_{tt}^{-1}\frac{\mathrm{RHS}_t}{\partial \alpha_t}\right)$$

$$\begin{aligned}\frac{\partial R_5}{\partial \alpha_r} = \frac{\partial m_t}{\partial \alpha_r} = m\left(\frac{\partial \Gamma_t}{\partial \alpha_r}\right) &= m\left(\left[\frac{\partial R_1}{\partial \Gamma_t}\right]^{-1}\frac{\partial R_1}{\partial \Gamma_t}\left[\frac{\partial R_2}{\partial \Gamma_t}\right]^{-1}\frac{\partial R_2}{\partial \alpha_r}\right) \\ &= m\left(\mathrm{AIC}_{tt}^{-1}\left[\mathrm{AIC}_{rt}\left[\mathrm{AIC}_{rr}^{-1}\frac{-\mathrm{RHS}_r}{\partial \alpha_r}\right]\right]\right)\end{aligned} \tag{3.67}$$

$$\frac{\partial R_5}{\partial \delta_{e_t}} = \frac{\partial m_t}{\partial \delta_{e_t}} = m\left(\frac{\partial \Gamma_t}{\partial \delta_{e_t}}\right) = m\left(\mathrm{AIC}_{tt}^{-1}\frac{\mathrm{RHS}_t}{\partial \delta_{e_t}}\right)$$

and the partial derivatives of R_6 are calculated as follows:

$$\frac{\partial R_6}{\partial \Gamma_r^k} = \frac{\partial m_r}{\partial \Gamma_r^k} = m\left(\frac{\partial \Gamma_t}{\partial \Gamma_r^k}\right)$$

$$\begin{aligned}\frac{\partial R_6}{\partial \alpha_t} = \frac{\partial m_r}{\partial \alpha_t} = m\left(\frac{\partial \Gamma_t}{\partial \alpha_t}\right) &= m\left(\left[\frac{\partial R_2}{\partial \Gamma_t}\right]^{-1}\frac{\partial R_2}{\partial \Gamma_t}\left[\frac{\partial R_1}{\partial \Gamma_t}\right]^{-1}\frac{-\partial R_1}{\partial \alpha_t}\right) \\ &= m\left(\mathrm{AIC}_{rr}^{-1}\left[\mathrm{AIC}_{tr}\left[\mathrm{AIC}_{tt}^{-1}\frac{-\mathrm{RHS}_t}{\partial \alpha_t}\right]\right]\right)\end{aligned} \tag{3.68}$$

$$\frac{\partial R_6}{\partial \alpha_r} = \frac{\partial m_r}{\partial \alpha_r} = m\left(\frac{\partial \Gamma_t}{\partial \alpha_r}\right) = m\left(\mathrm{AIC}_{rr}^{-1}\frac{\mathrm{RHS}_r}{\partial \alpha_r}\right)$$

$$\frac{\partial R_6}{\partial \delta_{e_r}} = \frac{\partial m_r}{\partial \delta_{e_r}} = m\left(\frac{\partial \Gamma_t}{\partial \delta_r}\right) = m\left(\mathrm{AIC}_{rr}^{-1}\frac{\mathrm{RHS}_r}{\partial \delta_{e_r}}\right)$$

Table 3.1: Partial derivatives of the governing equations with respect to the state variables

	Γ_t	Γ_r	α_t	α_r	δ_{e_t}	δ_{e_r}
R_1	AIC_{tt}	AIC_{tr}	$-\frac{\partial \mathrm{RHS}_t}{\partial \alpha_t}$	0	$\frac{\partial \mathrm{RHS}_t}{\partial \delta_{e_t}}$	0
R_2	AIC_{rt}	AIC_{rr}	0	$-\frac{\partial \mathrm{RHS}_r}{\partial \alpha_r}$	0	$\frac{\partial \mathrm{RHS}_r}{\partial \delta_{e_r}}$
R_3	$\frac{\partial L_t}{\partial \Gamma_t}$	0	$\frac{\partial L_t}{\partial \alpha_t}$	$\frac{\partial L_t}{\partial \alpha_r}$	$\frac{\partial L_t}{\partial \delta_{e_t}}$	0
R_4	0	$\frac{\partial L_r}{\partial \Gamma_r}$	$\frac{\partial L_r}{\partial \alpha_t}$	$\frac{\partial L_r}{\partial \alpha_r}$	0	$\frac{\partial L_r}{\partial \delta_{e_r}}$
R_5	$\frac{\partial m_t}{\partial \Gamma_t}$	0	$\frac{\partial m_t}{\partial \alpha_t}$	$\frac{\partial m_t}{\partial \alpha_r}$	$\frac{\partial m_t}{\partial \delta_{e_t}}$	0
R_6	0	$\frac{\partial m_r}{\partial \Gamma_r}$	$\frac{\partial m_r}{\partial \alpha_t}$	$\frac{\partial m_r}{\partial \alpha_r}$	0	$\frac{\partial m_r}{\partial \delta_{e_r}}$

All other partial derivatives are assumed to be zero, and full results are summarized in Table 3.1.

The change in the residuals with respect to a formation flight parameter, P_j, occurs only through the coupling terms AIC_{tr} and AIC_{rt}. For simplicity, the partial derivatives of the coupling terms with respect to P_j have been determined numerically, which provides the matrices $\frac{d\mathrm{AIC}_{tr}}{dP_j}$ and $\frac{d\mathrm{AIC}_{rt}}{dP_j}$. These are used to obtain the partial derivatives of the residuals with respect to P_j as follows:

$$\begin{aligned} \frac{\partial R_1}{\partial P_j} &= \frac{d\mathrm{AIC}_{tr}}{dP_j} \cdot \Gamma_2 \\ \frac{\partial R_2}{\partial P_j} &= \frac{d\mathrm{AIC}_{rt}}{dP_j} \cdot \Gamma_1 \\ \frac{\partial R_3}{\partial P_j} = \frac{\partial R_4}{\partial P_j} &= \frac{\partial R_5}{\partial P_j} = \frac{\partial R_6}{\partial P_j} = 0 \end{aligned} \tag{3.69}$$

Thus, all the necessary terms required by Equation 3.56 and Equation 3.57 have been derived, and the sensitivity $\frac{df}{dP_j}$ can be calculated. An additional benefit of performing sensitivity analysis in this way is that the key quantities $\partial C_L/\partial \alpha$ and $\partial C_m/\partial \alpha$ are found with low additional computational effort since they are calculated implicitly as part of the overall analysis.

3.4.4 Use of Adjoint-Based Sensitivities

To demonstrate the calculation of adjoint-based sensitivities in a two-way coupled calculation, the case of the VC-10 tanker with a Hercules receiver will be considered. Bloy and Trochadilis considered this case with the VC-10 represented by two horseshoe vortices, and the Hercules represented by a vortex lattice [10]. Here, both the VC-10 and Hercules will be represented by a vortex lattice. The planforms used by Bloy and Trochadilis to represent the Hercules receiver aircraft can be seen in Figure 3.19. While the Hercules planform used in this work was identical to the one used by Bloy and Trochadilis, the VC-10 planform used was simplified to have straight wingtips, as seen in Figure 3.20.

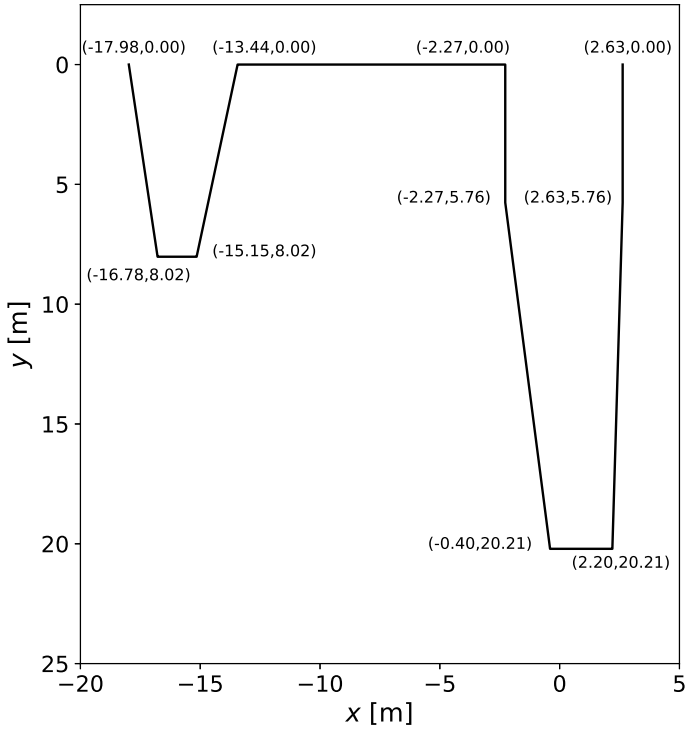

Figure 3.19: Hercules wing and tailplane planform breakpoints.

The centres of gravity for both aircraft are assumed to be at the origins. For the purposes of C_m calculation, the origin is also assumed to be placed at 35% of the mean aerodynamic chord from the leading edge of the planform. Some important specifications of the VC10 and Hercules aircraft used throughout this work, are listed in Table 3.2. Typical flight conditions are taken as Mach 0.5 at an altitude of 7600 m.

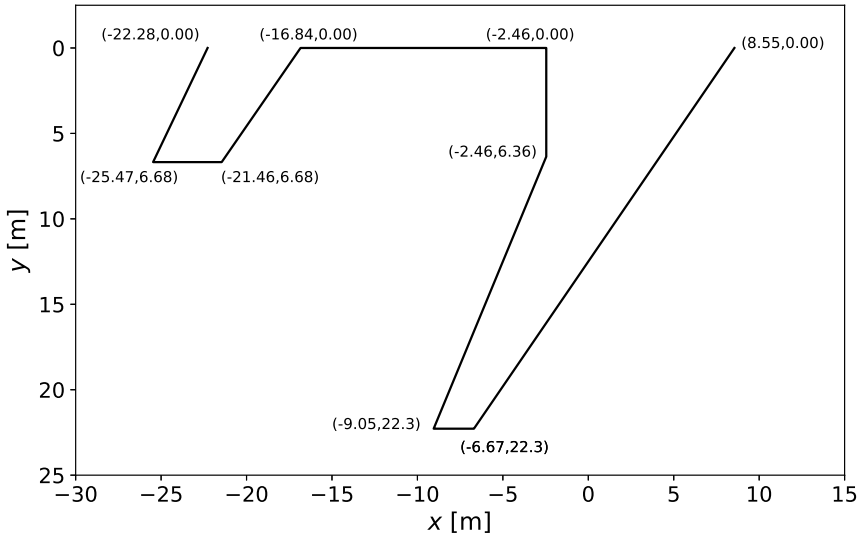

Figure 3.20: VC-10 wing and tailplane planform breakpoints.

Table 3.2: Details of tanker and receiver aircraft.

	VC10	Hercules
Wing area (m^2)	272.4	162.1
Tailplane area (m^2)	59.3	49.5
Tailplane height (m)	8.2	0
Mass (kg)	100×10^3	75.1×10^3

This analysis is simplified compared to the methodology outlined previously, in that the pitch trim will not be considered. This is because in the case of sensitivities, only the relative change in a quantity based on position is of interest, and this relative change does not vary significantly, regardless of whether trim in pitch is considered. In order to solve the coupled residual equations, an inner and outer iteration are used. Initial attempts to solve all residual equations simultaneously proved difficult to implement due to numerical instabilities. Therefore, a two-level algorithm was developed, and a flow chart of the solution scheme can be seen in Figure 3.21. The algorithm may be summarized as follows: first, the vortex circulation strengths, Γ_1 and Γ_2, are solved within the inner iteration. Before the inner iteration begins, an initial angle of attack is guessed for both aircraft. Cramer *et al.*'s individual discipline feasible (IDF) scheme [61] is used

to account for the couplings between the vortex circulation strengths. Once these are calculated for the given angle of attack, the outer iteration updates the angle of attack of both aircraft using a Newton's method. This algorithm then loops until the roots of all residual equations have been determined.

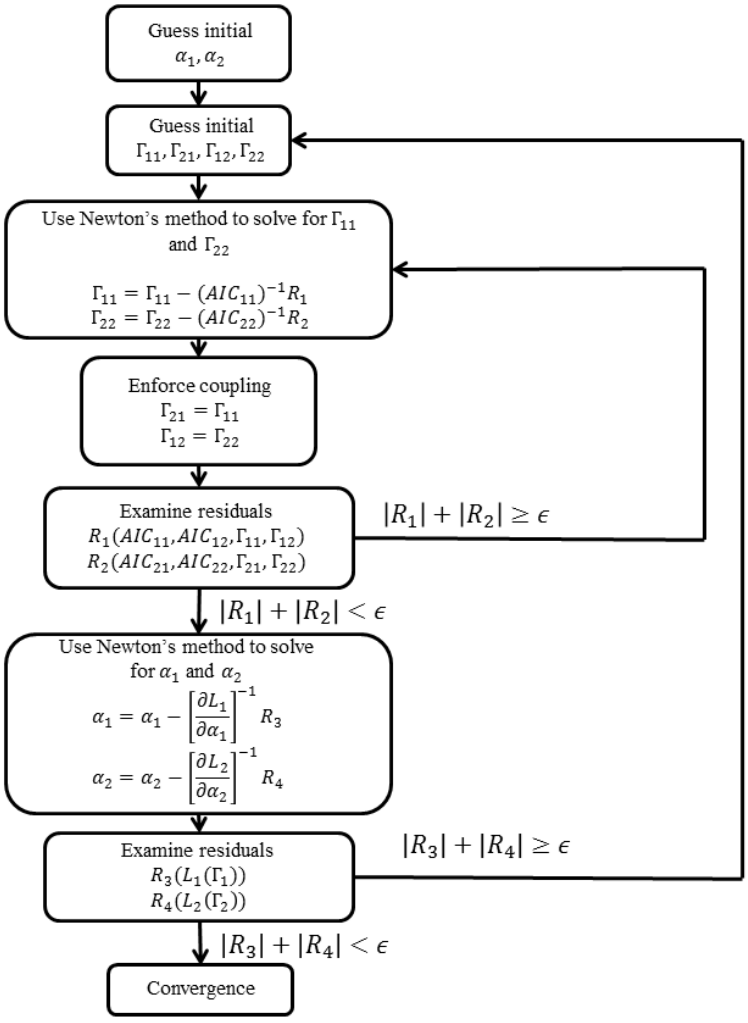

Figure 3.21: Flow chart of the two-level solution algorithm.

The derivatives of C_m with respect to Δz for the cases of a Hercules receiver aircraft flying behind a VC-10 and Hercules tanker were calculated using a finite difference method and the adjoint method outlined in Section 3.4.3. The results are summarized in Table 3.3.

Table 3.3: $\frac{dC_m}{d\Delta z}$ of a Hercules receiver behind a VC-10 tanker

z	Finite Difference (m^{-1})	Adjoint (m^{-1})	$\lvert\delta\rvert$
2	1.235×10^{-3}	1.246×10^{-3}	1.1×10^{-5}
4	-2.963×10^{-4}	-3.045×10^{-4}	8.2×10^{-6}
6	-3.003×10^{-4}	-3.093×10^{-4}	9.0×10^{-6}
8	-2.437×10^{-4}	-2.518×10^{-4}	8.1×10^{-6}
10	-1.978×10^{-4}	-2.046×10^{-4}	6.9×10^{-6}
12	-1.611×10^{-4}	-1.666×10^{-4}	2.4×10^{-6}
Normalized CPU time	1	0.21	

Most relevantly, the sensitivities calculated using the adjoint method were computed nearly five times faster than those computed using the finite difference method. Furthermore, there is good agreement between the sensitivities calculated by finite differences and the adjoint method, although there are some small differences. These differences are small, however, on an absolute scale, even if occasionally on the order of 10% of the sensitivity values themselves. They are likely caused by non-linearities in the local gradient.

3.5 Methodological Discussion

This chapter introduced the aerodynamic methodology used to calculate wake velocities, aerodynamic forces, and positional sensitivities in the subsequent analyses of PDR and FBR. In Chapter 4, propeller effects will be included to examine of the effect of asymmetries in the wake on the trim conditions and positional stability of the receiver during PDR. Chapter 5 will use longitudinal positional stability quantities in the analysis of PIO susceptibility. The question of when to use the one-way or two-way coupling is relevant, since the implementation of the latter is more complex and these analyses take longer to perform than the former which treat the flowfield induced by the tanker as fixed. Simultaneously trimming two aircraft that are aerodynamically coupled requires the use of an inner and outer iterative scheme, as shown in Figure 3.21, and this added complexity is only justified in cases where the behaviour of the tanker is of interest, the receiver is large relative to the tanker, and also close enough to have a measurable effect on the behaviour of the tanker. This is also why the fuselage of the receiver aircraft is not modelled in these analyses, since the receiver fuselage only has an effect on the behaviour of the tanker. In all subsequent analyses, it was determined that sensitivities from the faster one-way coupling were as effective as two way

coupling, but consumed less computational cost and time. However, a future use case for the two-way coupling algorithm could be analysis of PDR, where calculation of the forces on the drogue in the wake is required to predict its dynamics, and the bow-wave effect of the receiver is a non-negligible effect that must be considered.

4 Trim, Stability, and Dynamic Mode Analysis Framework

When analyzing aircraft dynamic modes, flying and handling qualities, it is common practice to decouple the longitudinal and lateral-directional degrees of freedom. This approach is appropriate when considering FBR, where the longitudinal stability and control is of much greater interest than the lateral and directional axes due to the downwash profile of the tanker being generally symmetrical about its centreline where refuelling occurs. However, during PDR where the fuel exchange system is mounted on the wing of the tanker, the receiver must contend with the changes in roll, pitch, and yaw moments simultaneously. Furthermore, it is known that compensating for the bow-wave effect of the receiver on the drogue must be performed in both the longitudinal and lateral-directional axes. Therefore, it is of interest to examine the behaviour and stability of the receiver in all axes simultaneously, and also to examine potential cross-coupling effects. In order to achieve this, a 6-DOF, 9-state aerodynamic model is integrated into the VLM analysis to examine both trim strategies and receiver dynamic characteristics in all axes during PDR. This is combined with the positional stability analysis introduced in Chapter 3 to create a framework that is used to examine both trim strategies and receiver dynamic characteristics during AAR.

The aircraft analyzed in this chapter are the C-130 Hercules tanker with an F/A-18 receiver. They were chosen due to the relatively large amount of public data available on both aircraft, and because they are a tanker-receiver combination that is most prevalent in the Royal Canadian Air Force (RCAF).

4.1 Methodology

As discussed in Chapter 2, the question of how to resolve the forces and moments imposed on the receiver during AAR is typically approached either by a full calculation of the effect of the flow-field on the receiver, or by averaging the downwash,

sidewash, and their velocity gradients and applying them at a single point, usually the receiver's CG. The methodology used in this section is a hybrid approach, wherein lift and rolling moments are calculated by integrating aerodynamic forces over the receiver model, but pitching and yawing moments are calculated using closed-form aerodynamic model, which assumes an effective angle of attack and sideslip that is calculated at the receiver's CG. The advantage of using the closed-form aerodynamic model is that it allows for analysis of dynamics at high angles of attack where potential flow methods break down due to flow separation. This is used in conjunction with the VLM and propwash model outlined in Chapter 3. Figure 4.1 shows the relationship between the various methodologies and the analysis objectives towards which they are applied to meet.

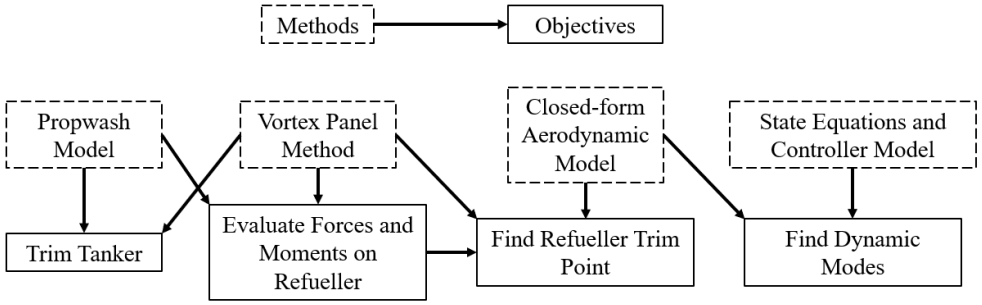

Figure 4.1: Relationship between framework methodologies and objectives.

The analysis is performed in a three-steps. First the tanker's trim point is determined, then the forces and moments on the receiver are evaluated in order to determine the receiver trim point. After the receiver trim point is determined, the dynamic modes can be calculated. The tanker trim point and receiver trim points are calculated separately to minimize calculation time. Once the full flow-field in the wake is established, it is assumed to be invariant. This is because the receiver, the F/A-18, is significantly smaller than the tanker and consequently its effect on the tanker is insignificant. Furthermore, any very small changes to the tanker's trim condition are not of interest.

4.1.1 Aerodynamic Model

An aerodynamic model is used to define the receiver's moment and force coefficients as closed-form expressions in terms of non-linear functions of α, β, control surface deflections, and kinematic rates. In general, the use of the closed-form aerodynamic model reduces computational time compared with calculating force and moments directly from the VLM. Additionally, the closed-form model has a greater range of validity for angles of attack and sideslip that lie outside the linear flight regime. This methodology is generic and can be easily adapted to differ-

ent aircraft since different model coefficients can be found by fitting the model to different aerodynamic data. The closed-form aerodynamic model used in this chapter for validation purposes is based on the F/A-18 aerodynamic model published by Chakraborty [62], itself based on flight test data published by Napolitano and Spagnuolo [63] and Iliff and Wang [64]. The closed form equations which define the aerodynamic model used are given in Appendix C. Some quantities, such as the lift force, lift coefficient C_L, rolling moment coefficient C_ℓ, and the pitch stiffness $\frac{\partial C_m}{\partial \alpha}$ are calculated using the VPM. This is done for two reasons: first, C_L and C_ℓ can be better estimated by integrating the variable aerodynamic forces over the panels rather than assuming a point value at the CG, and second, existing flight test data were subject to large uncertainties in the published values of $\frac{\partial C_m}{\partial \alpha}$ [65]. The values of $\frac{\partial C_m}{\partial \alpha}$ calculated using the VLM provided a better match of flight test data used for validation in Section 4.2. This would not necessarily be required for aircraft with better estimated aerodynamic data.

4.1.2 Axis Systems and Trim Equations

Both tanker and receiver are assumed to be in steady level flight. For the tanker, that requires:

$$L_t = W_t \qquad \text{and} \qquad m_t = 0$$

where L_t is the lift which is generated by the tanker, W_t is the weight of the tanker, and m_t is the overall pitching moment of the tanker about its CG. For the sake of simplicity, the effect of the thrust vector on the total lift generated by the tanker is ignored, since the angle of attack at the flight condition is very small (< 3 deg). By flying in the wake of the tanker, the receiver is subject to aerodynamic forces and moments that must be counteracted by flying with a combination of flight path and bank angles, control surface deflections, and thrust. These forces and moments are defined within the body axis and stability axis of the receiver. The body axis and stability axis system used can be seen in Figure 4.2, which shows an F/A-18 flying in steady level flight at an angle of attack α, which can be seen in the difference in the body axes (denoted by a subscript B) and the stability axes (denoted by a subscript S). The roll, pitch, and yaw moment coefficients (C_ℓ, C_m, and C_n) are defined about body frame axes x_B, y_B, and z_B respectively. The lift, drag, and side force coefficients (C_L, C_D, and C_Y) are defined as positive along $-z_S$, $-x_S$, and $+y_S$ respectively. The Euler angles Φ, Θ, and Ψ are rotations of the body axes, whereas the angles α and β are aerodynamic angles defined relative to the direction the aircraft is moving within the airflow at velocity V, as shown.

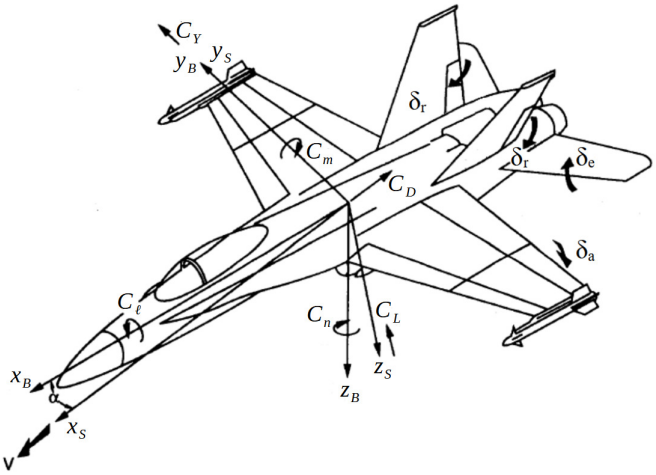

Figure 4.2: Body axis and stability axis system with control surface sign conventions. [1]

A unique aspect of α and β within an aircraft wake is that the wake velocities are not uniform in space meaning that different parts of the receiver flying within the wake experience different local α and β. Therefore, throughout this work, a simplifying assumption is made which defines an *effective* sideslip angle equal to the yaw angle minus the sideslip angle induced by the sidewash measured at the receiver center of gravity (CG) $\beta_{\text{eff}} = \Psi - \Delta_{v_{\text{ind}}}$. This is done so that a representative value of β can be used in the aerodynamic model, and choosing the CG as a representative point to evaluate wake velocities has been done in previous work of Bloy and Khan [16]. Similarly, the effective angle of attack is equal to the flight path angle plus the angle induced by the downwash measured at the receiver CG, $\alpha_{\text{eff}} = \Theta + \Delta_{w_{\text{ind}}}$.

In order to achieve trim, the sum of the forces and moments on the receiver must be equal to zero. For the forces in the stability body frame, this requires the force generated by the receiver in the z_B direction (F_{z_B}) and projected into the z_S axis plus the thrust generated by the receiver (T_r) projected into the z_S axis is equal and opposite to the weight of the receiver (W_r), as shown in Equation 4.1.

$$F_{z_B} \cos(\Theta) \cos(\Phi) + T \sin(\Theta) + W_r = 0 \tag{4.1}$$

Continuing in the stability frame, T_r projected into the x_S axis is equal and opposite to the drag, as represented in Equation 4.2.

$$D_r + T_r \cos(\Theta) = 0 \tag{4.2}$$

Finally, the force generated by the receiver in the z_B direction (F_{z_B}) and projected into the y_S axis plus any sideforce generated by the control surfaces (Y_r) is equal and opposite to the sideforce induced by the tanker wake (Y_{ind}), as shown in Equation 4.3.

$$F_{z_B}\sin(\Phi) + Y_r + Y_{\text{ind}} = 0 \tag{4.3}$$

For the moments defined about the receiver body axes, the moments caused by the control surface deflections and effective angle of attack and sideslip (m_r, l_r, n_r) are equal and opposite to the moments induced by the wake, (m_{ind}, l_{ind}, n_{ind}), following Equations 4.4, 4.5, and 4.6:

$$m_{\text{ind}} + m_r = 0 \tag{4.4}$$

$$l_{\text{ind}} + l_r = 0 \tag{4.5}$$

$$n_{\text{ind}} + n_r = 0 \tag{4.6}$$

The above series of six trim equations has seven unknowns: $\Theta, \Phi, \Psi, T, \delta_a, \delta_e, \delta_r$. Therefore, to solve for the trim states, one of the unknown values must be provided. In this work, trim conditions for $\Psi = 0$ and $\Phi = 0$ will be examined.

4.1.3 State Equations

The equations of motion are a six-DOF, nine-state mathematical model. They are adapted from NASA Contractor Report 194838 [63]. The equations of motion take the form

$$\dot{x} = f(x, u) \tag{4.7}$$

where $x := [V\ (\text{m/s}), \beta\ (\text{rad}), \alpha\ (\text{rad}), p\ (\text{rad/s}), q\ (\text{rad/s}), r\ (\text{rad/s}), \Phi\ (\text{rad}), \Theta\ (\text{rad}), \Psi\ (\text{rad})]$ and $u := [\delta_a\ (\text{rad}),\ \delta_e\ (\text{rad}), \delta_r\ (\text{rad}), T\ (\text{N})]$. The force equations are given as follows:

$$\begin{aligned}\dot{V} = &-\frac{\bar{q}S}{m}C_{D_{\text{ind}}} + g(\cos\Phi\cos\Theta\sin\alpha\cos\beta + \sin\Phi\cos\Theta\sin\beta) \\ &- g(\sin\Theta\cos\alpha\cos\beta) + \frac{T}{m}\cos\alpha\cos\beta\end{aligned} \tag{4.8}$$

$$\begin{aligned}\dot{\alpha} = &-\frac{\bar{q}S}{mV\cos\beta}C_L + q - \tan\beta(p\cos\alpha + r\sin\alpha) \\ &+ \frac{g}{V\cos\beta}(\cos\Phi\cos\Theta\cos\alpha + \sin\Theta\sin\alpha) - \frac{T\sin\alpha}{mV\cos\beta}\end{aligned} \tag{4.9}$$

$$\begin{aligned}\dot{\beta} =& \frac{\bar{q}S}{mV} C_{Y_{\text{ind}}} + p\sin\alpha - r\cos\alpha + \frac{g}{V}\cos\beta\sin\Phi\cos\Theta \\ &+ \frac{\sin\beta}{V}(g\cos\alpha\sin\Theta - g\sin\alpha\cos\Phi\cos\Theta + \frac{T}{m}\cos\alpha)\end{aligned} \tag{4.10}$$

where

$$C_{D_{\text{ind}}} = C_D\cos\beta - C_Y\sin\beta \tag{4.11}$$

$$C_{Y_{\text{ind}}} = C_Y\cos\beta + C_D\sin\beta \tag{4.12}$$

The rate of change of the roll, pitch, and yaw rates are related to the rates themselves and to the roll, pitch, and yaw moment coefficients as follows:

$$\dot{p} = \frac{1}{\kappa}\big(\big[(\bar{q}Sb)(I_z C_\ell + I_{xz}C_n)\big] - \big[I_{xz}^2 + I_z(I_z - I_y)\big]qr\big) \tag{4.13}$$

$$\dot{q} = \frac{1}{I_y}\big(\bar{q}S\bar{c}C_m + (I_z - I_x)pr\big) \tag{4.14}$$

$$\dot{r} = \frac{1}{\kappa}\big(\big[(\bar{q}Sb)(I_{xz}C_\ell + I_x C_n)\big] + \big[I_{xz}^2 + I_x(I_x - I_y)\big]pq\big) \tag{4.15}$$

$$\kappa = I_x I_z - I_{xz}^2 \tag{4.16}$$

Finally, the rate of change of the rotation of the aircraft's body axes is related to the roll, pitch, and yaw rates (p, q, r) as follows:

$$\begin{bmatrix}\dot{\Phi}\\ \dot{\Theta}\\ \dot{\Psi}\end{bmatrix} = \begin{bmatrix}1 & \sin\Phi\tan\Theta & \cos\Phi\tan\Theta\\ 0 & \cos\Phi & -\sin\Phi\\ 0 & \sin\Phi\sec\Theta & \cos\Phi\sec\Theta\end{bmatrix}\begin{bmatrix}p\\ q\\ r\end{bmatrix} \tag{4.17}$$

The equations for C_m, C_ℓ, C_n, C_Y, and C_D are non-linear in α and take the following form:

$$\begin{aligned}C_m =& \big(C_{m\alpha 3}\alpha^3 + C_{m\alpha 2}\alpha^2 + C_{m\alpha 1}\alpha\big) + \big(C_{m\delta_e 2}\alpha^2 + C_{m\delta_e 1}\alpha + C_{m\delta_e 0}\big)\delta_e \\ &+ \frac{\bar{c}}{2V}\big(C_{mq3}\alpha^3 + C_{mq2}\alpha^2 + C_{mq1}\alpha + C_{mq0}\big)q\end{aligned} \tag{4.18}$$

$$\begin{aligned}C_\ell =& \big(C_{\ell\beta 4}\alpha^4 + C_{\ell\beta 3}\alpha^3 + C_{\ell\beta 2}\alpha^2 + C_{\ell\beta 1}\alpha + C_{\ell\beta 0}\big)\beta \\ &+ \big(C_{\ell\delta_a 3}\alpha^3 + C_{\ell\delta_a 2}\alpha^2 + C_{\ell\delta_a 1}\alpha + C_{\ell\delta_a 0}\big)\delta_a \\ &+ \big(C_{\ell\delta_r 3}\alpha^3 + C_{\ell\delta_r 2}\alpha^2 + C_{\ell\delta_r 1}\alpha + C_{\ell\delta_r 0}\big)\delta_r \\ &+ \frac{b}{2V}\big(C_{\ell p1}\alpha + C_{\ell p0}\big)p + \frac{b}{2V}\big(C_{\ell r2}\alpha^2 + C_{\ell r1}\alpha + C_{\ell r0}\big)r\end{aligned} \tag{4.19}$$

$$\begin{aligned} C_n =& \big(C_{n\beta 2}\alpha^2 + C_{n\beta 1}\alpha + C_{n\beta 0}\big)\beta \\ &+ \big(C_{n\delta_a 3}\alpha^3 + C_{n\delta_a 2}\alpha^2 + C_{n\delta_a 1}\alpha + C_{n\delta_a 0}\big)\delta_a \\ &+ \big(C_{n\delta_r 4}\alpha^4 + C_{n\delta_r 3}\alpha^3 + C_{n\delta_r 2}\alpha^2 + C_{n\delta_r 1}\alpha + C_{n\delta_r 0}\big)\delta_r \\ &+ \frac{b}{2V}\big(C_{np1}\alpha + C_{np0}\big)p + \frac{b}{2V}\big(C_{nr1}\alpha + C_{nr0}\big)r \end{aligned} \tag{4.20}$$

$$\begin{aligned} C_Y =& \big(C_{Y\beta 2}\alpha^2 + C_{Y\beta 1}\alpha + C_{Y\beta 0}\big)\beta \\ &+ \big(C_{Y\delta_a 3}\alpha^3 + C_{Y\delta_a 2}\alpha^2 + C_{Y\delta_a 1}\alpha + C_{Y\delta_a 0}\big)\delta_a \\ &+ \big(C_{Y\delta_r 3}\alpha^3 + C_{Y\delta_r 2}\alpha^2 + C_{Y\delta_r 1}\alpha + C_{Y\delta_r 0}\big)\delta_r \end{aligned} \tag{4.21}$$

$$\begin{aligned} C_D =& \big(C_{D\alpha 4}\alpha^4 + C_{D\alpha 3}\alpha^3 + C_{D\alpha 2}\alpha^2 + C_{D\alpha 1}\alpha + C_{D\alpha 0}\big)\cos\beta + C_{D_0} \\ &+ \big(C_{D\delta_e 3}\alpha^3 + C_{D\delta_e 2}\alpha^2 + C_{D\delta_e 1}\alpha + C_{D\delta_e 0}\big)\delta_e \end{aligned} \tag{4.22}$$

The coefficients of Equations 4.18 through 4.22 can be found in Appendix C.

4.2 Validation

The validation of the C-130 wake model and F/A-18 VLM model was shown in Chapter 3. This section presents the validation of the F/A-18 controller and aerodynamic model by comparing the open-loop and closed-loop dynamic behaviour of the combined models to published flight test data.

4.2.1 Controller and Dynamic Model

It is customary for linear analyses of closed-loop systems to use reduced order control models to assess stability and performance about certain trim points. Here, only the first-order response and stability of the aircraft is of interest, and therefore the higher order terms in the control law can be neglected. Figure 4.3 shows the simplified control law used to examine closed-loop dynamic behaviour. This controller structure is based on the F/A-18 Control Augmentation System (CAS) presented in Buttrill *et al.*, which is a lower-order model of the full aircraft CAS [1].

For the sake of simplicity, actuator dynamics and several filters are ignored and the controller only uses feedback of α, q, r, and p. Actuator dynamics are ignored, since their response rates are much faster than the frequencies of the aircraft dynamic modes [1], and therefore their influence on the closed loop modes is negligible. In longitudinal feedback, the angle of attack α and pitch rate q have the

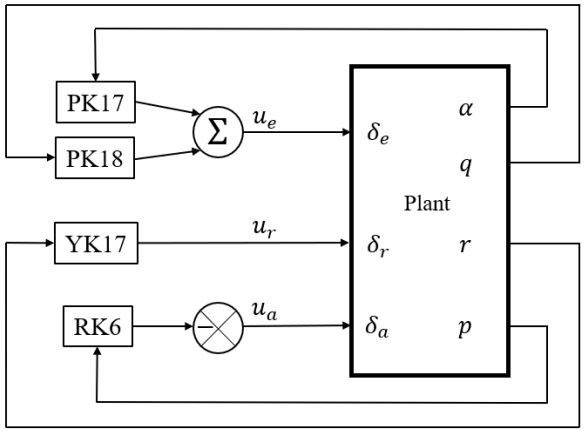

Figure 4.3: F/A-18 reduced order flight control law.

gains defined by Buttrill as PK17 and PK18 respectively. The rudder channel feedback is multiplied by the gain given in function YK17. The roll channel feedback is multiplied by gain given by function RK6 and rendered negative.

Thrust is assumed to be held constant at its trim value in all analyses. This gives the plant measurements as $y = [V\ \beta\ \alpha\ p\ q\ r\ \Phi\ \Theta\ \Psi]$ and the controller input vector as $u = [\delta_a\ \delta_e\ \delta_r]$. The controller feedback matrix is:

$$\big[K\big] = \begin{bmatrix} 0 & 0 & 0 & RK6 & 0 & 0 & 0 & 0 & 0 \\ 0 & 0 & -PK17 & 0 & -PK18 & 0 & 0 & 0 & 0 \\ 0 & 0 & 0 & 0 & 0 & -YK17 & 0 & 0 & 0 \end{bmatrix} \tag{4.23}$$

and the control effectiveness matrix B is given in Equation 4.24.

$$\big[B\big] = \begin{bmatrix} \frac{\partial V}{\partial \delta_a} & \frac{\partial V}{\partial \delta_e} & \frac{\partial V}{\partial \delta_r} \\ \frac{\partial \beta}{\partial \delta_a} & \frac{\partial \beta}{\partial \delta_e} & \frac{\partial \beta}{\partial \delta_r} \\ 0 & \frac{\partial \alpha}{\partial \delta_e} & 0 \\ \frac{\partial p}{\partial \delta_a} & 0 & \frac{\partial p}{\partial \delta_r} \\ 0 & \frac{\partial q}{\partial \delta_e} & 0 \\ \frac{\partial r}{\partial \delta_a} & 0 & \frac{\partial r}{\partial \delta_r} \\ 0 & 0 & 0 \\ 0 & 0 & 0 \\ 0 & 0 & 0 \end{bmatrix} \tag{4.24}$$

The derivatives in the control effectiveness matrix can all be found analytically from the aerodynamic model by linearizing the state equations about the trim point. The controller-augmented closed-loop plant matrix, the eigenvalues of which give the natural modes of the aircraft, is $A - BK$, where A is the linearized plant matrix.

In order to validate the aerodynamic and dynamic model, the eigenvalues of the aircraft's dynamic modes published in Davidson [66] and Ostroff *et al.* [67] were used as a basis for comparison. NASA's High-Alpha Research Vehicle (HARV) was a modified F/A-18 developed to study high angle of attack technologies including thrust-vectoring and other advanced aerodynamic controls. In order to evaluate the controller model and gains, the predicted flying qualities of both the open-loop and closed-loop systems were examined for the flight conditions given in Tables 4.1 and 4.2.

Table 4.1: Trim Conditions and Open-Loop Short-Period Frequencies

Flight Conditions		Published [67]		Model	
Altitude (ft)	Mach (-)	Trim α (deg)	Short-Period Freq. (rad/s)	Trim α (deg.)	Short-Period Freq. (rad/s)
15 000	0.70	2.52	2.7	2.66	2.39
15 000	0.49	5.0	1.4	5.8	1.4
25 000	0.70	3.58	2.1	3.47	1.9
25 000	0.59	5.0	1.5	5.36	1.4
35 000	0.70	5.34	1.5	4.85	1.5
35 000	0.60	7.24	1.0	7.43	1.1

Table 4.2: Trim Conditions and Open-Loop Lateral-Directional Eigenvalues

	Published [66]				Model			
Mach (-)	Trim α (deg.)	Spiral	Roll	Dutch Roll	Trim α (deg.)	Spiral	Roll	Dutch Roll
0.59	5.0	0.004	-1.40	-0.20$\pm$1.67i	5.36	-0.03	-1.00	-0.41$\pm$1.50i
0.41	10.0	0.011	-0.74	-0.21$\pm$1.58i	11.6	-0.06	-0.46	-0.34$\pm$1.52i
0.36	15.0	0.006	-0.46	-0.19$\pm$1.56i	15.6	-0.08	-0.35	-0.27$\pm$1.54i
0.33	20.0	-0.033	-0.28	-0.16$\pm$1.77i	18.1	-0.09	-0.30	-0.23$\pm$1.55i

The model shows a slight tendency to under-predict the short-period frequency at higher mach numbers. However, because most AAR takes place below Ma=0.6, this is not considered a serious problem. The lateral-directional modes show good agreement in terms of Dutch roll frequency and roll subsidence, although the predicted Dutch roll damping is higher than the published values. Furthermore, the published data indicate an unstable spiral mode for the F/A-18 that the model

does not [66]. In practice, the unstable spiral mode necessitates the use of a washout filter, as noted by Buttrill *et al.* [1].

The dynamic characteristics of an aircraft are referred to as flying qualities, and are often described in terms of qualitative levels. Level 1 flying qualities are satisfactory, Level 2 flying qualities are acceptable, and Level 3 flying qualities result in a controllable aircraft with excessive pilot workload, or mission effectiveness degradation. When considering the longitudinal flying qualities of an aircraft, it is assumed that two responses of particular interest to the pilot are the initial pitch acceleration and the steady state normal acceleration (n/α) from a step input. The control anticipation parameter (CAP) is the ratio of these two parameters and is given in Equation 4.25.

$$\text{CAP} = \frac{\omega_n^2}{n/\alpha} \tag{4.25}$$

where ω_n is the short period frequency. The term n/α can be calculated from the derivatives of the dimensionalized pitching moment with respect to elevator deflection (M_δ), angle of attack (M_α), and pitch rate (M_q), as well as the derivative of the vertical acceleration with respect to angle of attack (Z_α) and elevator deflection (Z_δ). These derivatives are given in Equations 4.26 through 4.30, and the equation for n/α itself is given in Equation 4.31.

$$M_\delta = \frac{QSc}{I_y}\frac{\partial C_m}{\partial \delta_e} \tag{4.26}$$

$$M_\alpha = \frac{QSc}{I_y}\frac{\partial C_m}{\partial \alpha} \tag{4.27}$$

$$M_q = \frac{QSc}{I_y}\left(\frac{c}{2V}\right)\frac{\partial C_m}{\partial (qc/2V)} \tag{4.28}$$

$$Z_\delta = \frac{-QS}{m}\frac{\partial C_L}{\partial \delta_e} \tag{4.29}$$

$$Z_\alpha = \frac{QS}{m}(C_D - \frac{\partial C_L}{\partial \alpha}) \tag{4.30}$$

$$\frac{n}{\alpha} = \frac{U_\infty}{g}\left[\frac{-M_\alpha Z_\delta + Z_\alpha M_\delta}{-M_q Z_\delta + U_\infty M_\delta}\right] \tag{4.31}$$

The comparison of the short period flying qualities for the open- and closed-loop F/A-18 model can be seen in Figure 4.4.

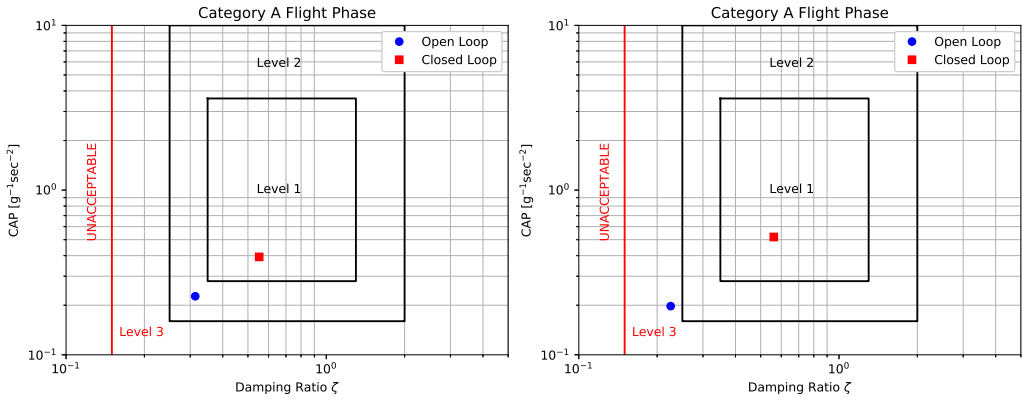

(a) 15 000 ft, Ma=0.7 (b) 35 000 ft, Ma=0.6

Figure 4.4: Open-loop and closed-loop flying qualities of the short period mode with respect to MIL-STD-1797A [68].

Figure 4.4 shows a clear improvement in the flying qualities between the open-loop and closed-loop plant across different flight conditions. At the higher speed, lower altitude flight condition, the open-loop system is predicted to have Level 2 flying qualities, and at the lower speed, higher altitude flight condition, the open-loop system is predicted to have Level 3 flying qualities. In both cases, the short period damping and the CAP are too small to allow for Level 1 flying qualities. At both flight conditions tested, the addition of the α and pitch rate q feedback increases damping and CAP, and improves the flying qualities to Level 1. This shows that the controller in the closed-loop system functions as designed.

When examining the Dutch roll and lateral-directional flying qualities, the addition of a washout filter was also examined. The comparison of the Dutch roll flying qualities can be seen in Figure 4.5. It can be seen that the closed loop system had little effect on the natural frequency of the Dutch roll while it increased the damping, as one would expect in a well-designed controller system. In general, it is expected that a washout filter should further dampen the Dutch roll mode of the aircraft. However, in Figure 4.5a, it can be seen that, as implemented in this model, the use of a washout filter at higher Mach resulted in both a reduction in damping and natural frequency compared to the simple closed loop model. Since the implementation of the washout filter did not improve the aircraft's flying qualities at the two flight conditions examined it was not included in the closed loop analysis. The lack of an unstable spiral mode, which might also necessitate the use of the washout filter, further justifies this decision.

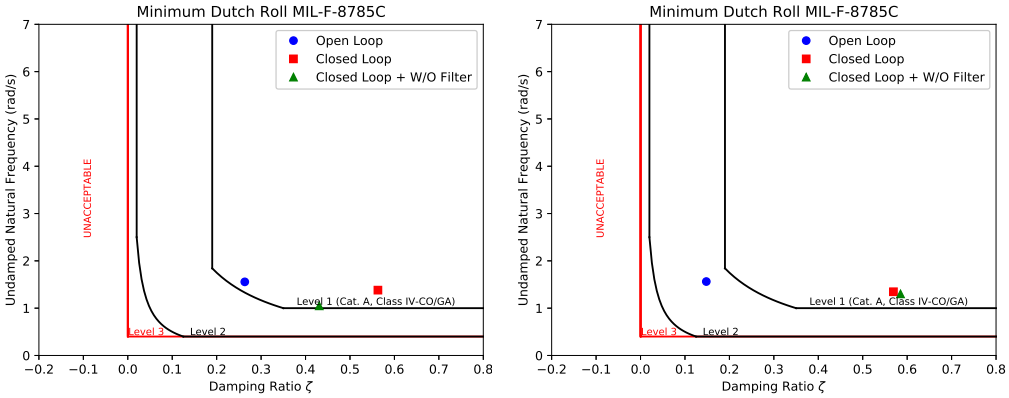

(a) 25 000 ft, Ma=0.59 (b) 25 000 ft, Ma=0.33

Figure 4.5: Open-loop and closed-loop Dutch roll flying qualities.

4.3 Trim Strategies and Dynamic Modes

Analyses were performed assuming the nominal refuelling conditions shown in Table 4.3 that correspond to closed loop controller gains of PK17 = 0.5, PK18 = 0.47, YK17 = 0.84, and RK6 = 0.169. All analyses were performed with a 5m longitudinal separation between the tail of the C-130 and the nose of the F/A-18. The typical vortex panel representation of this flight formation can be seen in Figure 4.6.

Table 4.3: Refuelling Conditions

Parameter	Value	Units
Airspeed	250	KIAS
Ma_∞	0.54	-
Altitude	20 000	ft MSL
ρ_∞	0.653	kg/m^3
a	316	m/s

Two trim strategies are presented here: the first involves trimming the aircraft at a roll angle of $\Phi = 0$ and yawing the aircraft to use minimize the sideslip angle and the thrust of the engines to counteract the sideforce in the wake of the tanker *i.e.*

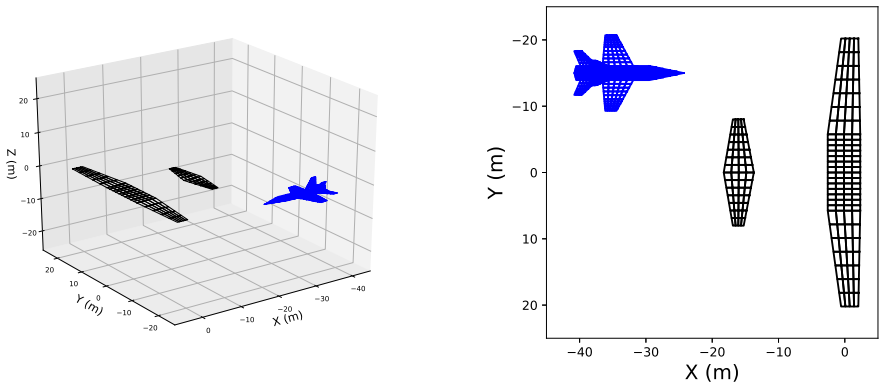

(a) Isometric View (b) 2D View in X-Y Plane

Figure 4.6: Vortex panel representation of the C-130 (black) and F/A-18 (blue) flying in close formation.

wings level, or string-centred trimming. The second strategy involves trimming the aircraft at a yaw angle of $\Psi = 0$ and rolling the aircraft and using the tilt of the F_{Z_B} vector to counteract the sideforce in the wake of the tanker *i.e.* constant heading or ball-centred trimming.

To help the reader to interpret the data presented, the Z-axis of Figure 4.6 and Figures 4.7 through 4.14 is defined such that a negative value corresponds to a location below the tanker, rather than above, as would be seen in the stability axis system. These left-handed axes are represented by X, Y, Z coordinates. In contrast, x, y, z coordinates correspond to the right-handed axes. Furthermore, the following figures are presented in the form of data contours filling a vertical slice in the Y-Z plane at the stated tail-to-nose longitudinal separation of 5 m. The contour value displayed at a certain point (Y, Z) is the value that corresponds to the receiver positioning, where its nose is positioned at (Y, Z), taking into account the aerodynamic forces over the entire receiver. In Figures 4.7 through 4.14, the airflow is moving in the $-X$ direction (coming out of the page). Figures 4.7 through 4.14 also show an outline of the C-130's wing and propeller locations to further help the reader interpret the results. From this (the receiver's) perspective, the propellers are rotating in the counter-clockwise direction. In several figures, the small white or black boxes denote areas of interest that will be further explored in Section 4.3.4.

4.3.1 Pitch, Roll, and Yaw at Trim

Figure 4.7 shows the predicted trim pitch angle at locations immediately below the wing of the C-130.

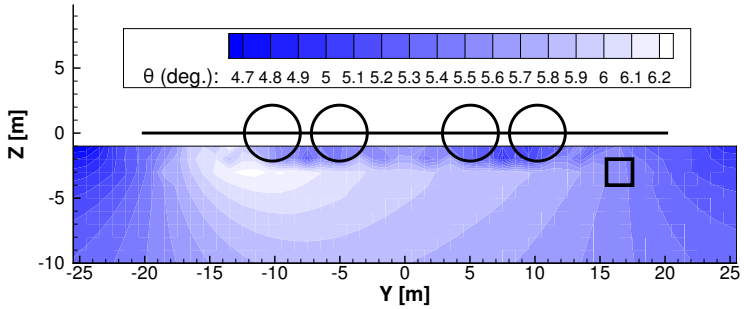

(a) Modelled Pitch Angle Θ, (Trim condition: variable Ψ, $\Phi = 0$)

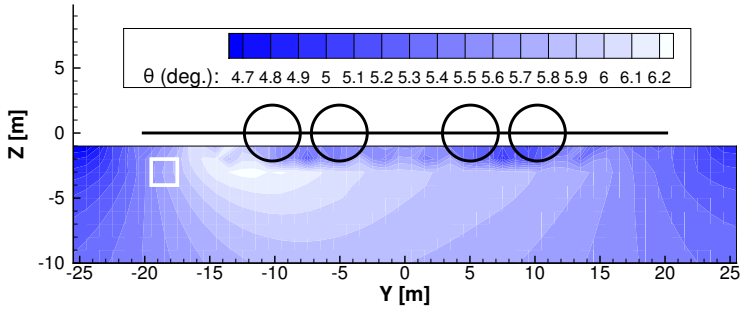

(b) Modelled Pitch Angle Θ, (Trim condition: variable Φ, $\Psi = 0$)

Figure 4.7: Trim pitch angle Θ, at various points in the wake behind a C-130 at 20 000 ft, Ma=0.54, and 5 m longitudinal separation.

Both figures show that the trim pitch angle is between 4.7 degrees in the areas of upwash outboard of the C-130 wingtips, and 6.2 degrees in the area of downwash near the left propellers of the C-130. The trim strategy chosen has very little effect on the trim pitch angle at the same locations in the wake. It can also be seen that flying in the immediate streamtube of the props at z = -2 m necessitates a lower angle of attack at trim due to the increase in local air velocity over the wings of the receiver. In general, these suggest that receiving fuel from a pod on the right wing may be preferable to receiving fuel from a pod on the left wing, since the upbound propwash works against the downwash on the right wing, leading to less sensitivity to trim pitch angle to receiver position.

Figure 4.8 shows the trim yaw angle and sideslip angle given a roll angle of zero, and Figure 4.9 shows the trim roll angle and sideslip angle for a yaw angle of zero. It can be seen in Figure 4.8 that for the variable yaw trim strategy, at most locations in the wake the yaw angle is such that it minimizes the sideslip angle, whereas in Figure 4.9, the roll and sideslip angles map onto each other very closely, since the roll angle is being used to counter the sidewash, and the sideslip angle is directly proportional to the amount of sidewash experienced. In both figures, as in Figure 4.7, some asymmetry about Y = 0 in the trim conditions can be seen due to the effect of the propwash, as the magnitude of the trim angles is larger on the left side than on the right side, again suggesting that, if the F/A-18 pilot is given a choice, it may be preferable to receive fuel from the right wing of a C-130.

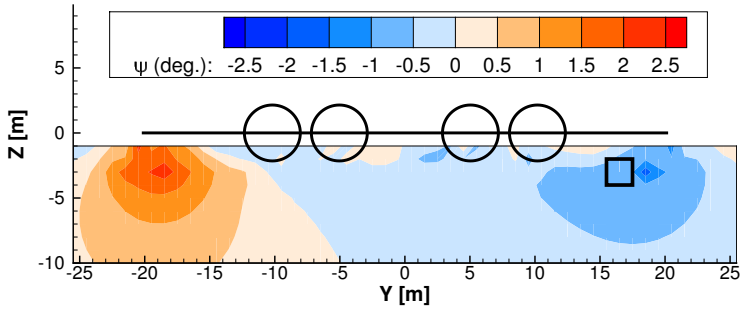

(a) Modelled Yaw Angle Ψ, (Trim condition: variable Ψ, $\Phi = 0$)

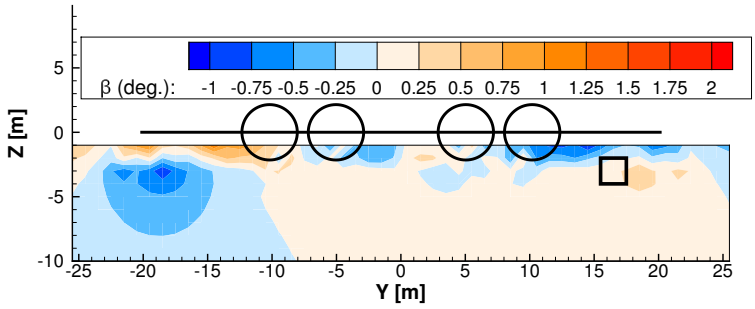

(b) Modelled Sideslip Angle β, (Trim condition: variable Ψ, $\Phi = 0$)

Figure 4.8: Yaw Ψ and Sideslip angle β in the C-130 wake with a trim strategy where $\Phi = 0$ (variable heading), altitude 20 000 ft, Ma=0.54, longitudinal separation = 5 m.

In general, the modelled trim data from Figures 4.7 through 4.9 suggest that, regardless of trim strategy, the ideal location for a contact point during F/A-18 AAR with a C-130 tanker is as far inboard of the right wingtip as possible, while

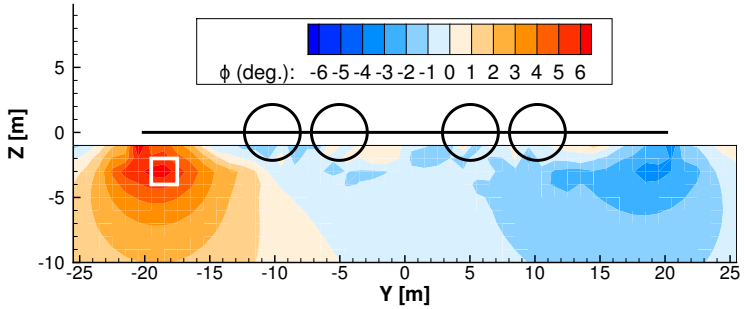

(a) Modelled Roll Angle Φ, (Trim condition: variable Φ, $\Psi = 0$)

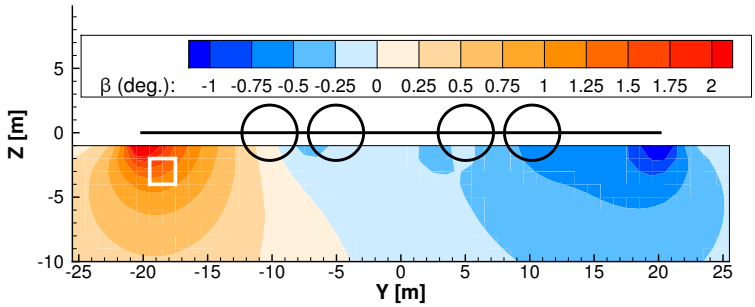

(b) Modelled Sideslip Angle β, (Trim condition: variable Φ, $\Psi = 0$)

Figure 4.9: Roll Φ and Sideslip angle β in the C-130 wake with a trim strategy where $\Psi = 0$ (constant heading), altitude 20 000 ft, Ma=0.54, longitudinal separation = 5 m.

still avoiding any interactions with the propwash. This location minimizes the aerodynamic forces in the wake, and therefore allows for the smallest deviation from regular flight. Consider the AAR procedure being conducted in Figure 4.10.

Figure 4.10: KC-130 tanker refuelling two F-35B receivers.[1]

The installation location of the PDR refuelling pods attached to the KC-130 shown in Figure 4.10 corresponds roughly to the location identified in the black boxes in the preceding figures. This is a further validation of the framework introduced in this chapter, in that it is capable of identifying refuelling contact points that have been independently determined to be optimal in practical operations. This has further use in tanker-receiver compatibility analysis and airworthiness clearance procedures, since PDR pods can be installed on tankers at different locations. The identification of suitable refuelling areas can guide this process.

4.3.2 Control Surface Deflections at Trim

The control surface deflections required to maintain trim are also found in this analysis, and Figure 4.11 shows the aileron deflection required to achieve trim at various points behind the C-130.

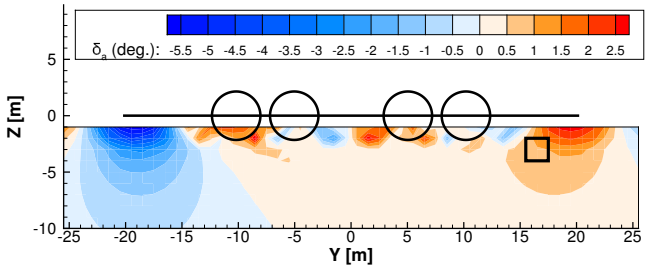

(a) Trim condition: variable Ψ, $\Phi = 0$

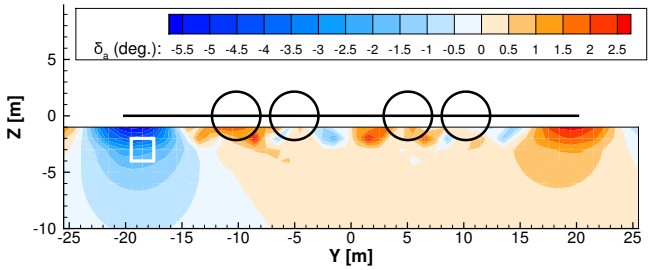

(b) Trim condition: variable Φ, $\Psi = 0$

Figure 4.11: Modelled trim aileron deflection, δ_a, in the C-130 wake, altitude 20 000 ft, Ma=0.54, longitudinal separation = 5 m.

As in previous figures, it can be seen that there is a clear asymmetry, and that there is very little difference between the required aileron deflections regardless

[1]Disclaimer: This is a Defense Visual Information Distribution Service photo. The appearance of U.S. Department of Defense (DOD) visual information does not imply or constitute DOD endorsement.

of whether the fighter is flying at $\Phi = 0$ or $\Psi = 0$. The effect of flying within the propeller streamtubes can also be clearly seen, since differences in lift generated by both wings requires compensation from the ailerons to achieve trim. In general, aileron deflection at trim can be thought of as a measure of the change in upwash or downwash across the span of the receiver. Areas where the trim aileron deflections are the largest correspond to areas where one receiver wing is in an area of upwash and the other receiver wing is in an area of downwash, producing a larger rolling moment which must be countered with greater aileron deflections.

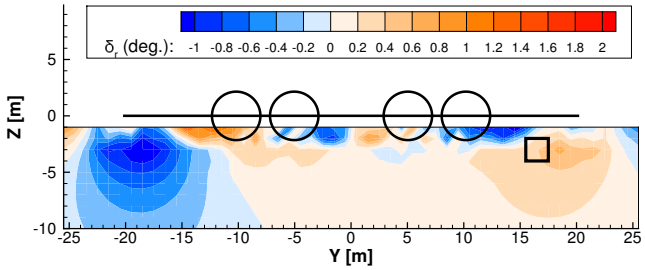

(a) Trim condition: variable Ψ, $\Phi = 0$

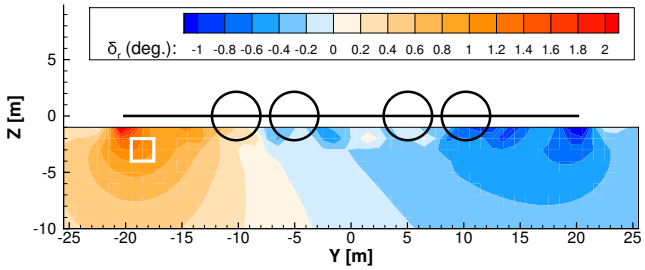

(b) Trim condition: variable Φ, $\Psi = 0$

Figure 4.12: Modelled trim rudder deflection, δ_r, in the C-130 wake, altitude 20 000 ft, Ma=0.54, longitudinal separation = 5 m.

Figure 4.12 shows the rudder deflection required to achieve trim. A large difference in rudder deflection required to maintain trim between the two analyzed trim strategies can be seen in Figure 4.12. When trimming for $\Phi = 0$, as seen in Figure 4.12a, the aircraft must yaw towards the centreline of the C-130 to counteract the sideforce. When this results in a non-zero sideslip, it causes a counteracting yaw force from the vertical stabilizers which must be compensated by opposite rudder to maintain the constant yaw angle. This corresponds to right rudder when on flying on the left side of the C-130 and left rudder when flying on the right side of the C-130. With $\Psi = 0$,, as seen in Figure 4.12b, the sidewash in the wake causes a yawing moment in the direction towards the centreline, that must be countered

with opposite rudder; left rudder when flying on the left side of the C-130, and right rudder when flying on the right side of the C-130. However, in general these rudder deflections are not very large, with 1 degree or less being necessary except in areas within 3 m of the C-130 wingtips.

4.3.3 Control Surface Positional Stability

Recall from the last chapter that the receiver is said to be positionally stable if forces in the wake tend to return the refuelling aircraft back to its original position when disturbed [32]. By calculating trim points at different locations in the wake, the positional stability can be examined in terms of control surface deflections, rather than change in induced moments. This is done by evaluating the changes in wake velocities with respect to Y and Z at each trim point and using the trim equations to predict the required change in control surface deflections to counter these changes using the coupled sensitivity analysis discussed in Chapter 3. This contextualizes the stability parameters in terms of pilot input that would be required to achieve an equivalent force or moment. Required change in control surface deflection with respect to change in lateral position can be seen in Figures 4.13 and 4.14.

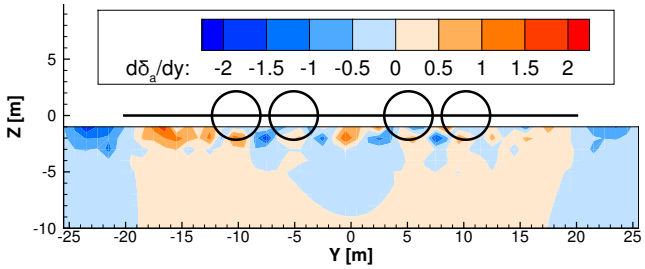

(a) Aileron deflection stability

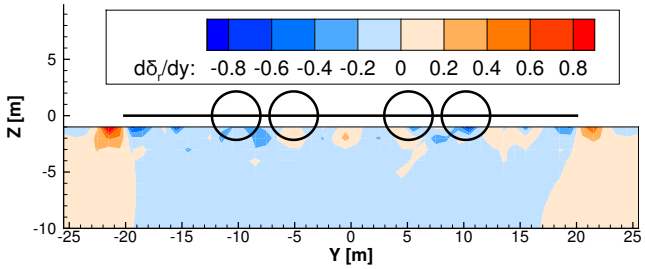

(b) Rudder deflection stability

Figure 4.13: Change in control surface deflection at trim with respect to change in lateral position in the C-130 wake, altitude 20 000 ft, Ma=0.54, longitudinal separation = 5 m. (Trim condition: variable Φ, $\Psi = 0$)

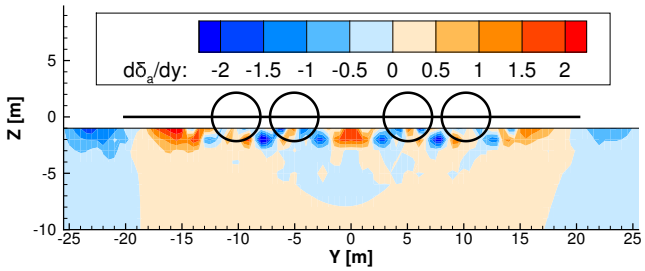

(a) Aileron deflection stability

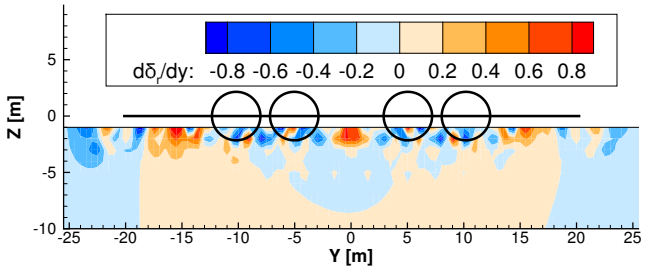

(b) Rudder deflection stability

Figure 4.14: Change in control surface deflection at trim with respect to change in lateral position in the C-130 wake, altitude 20 000 ft, Ma=0.54, longitudinal separation = 5 m. (Trim condition: variable Ψ, $\Phi = 0$).

Figure 4.13 shows positional stability with respect to control surface deflections for trim at no yaw angle, $\Psi = 0$. At most locations immediately behind the C-130's wing, the aileron deflection stability is positive. This means that as the F/A-18 moves in the positive Y direction, an increase in positive (right) aileron is required to maintain trim. Without this, the receiver will tend back towards its initial position, indicating positional stability in the roll axis. Similarly, at these same locations negative rudder deflection stability is observed. Based on the sign convention used here, left rudder is positive. As the F/A-18 moves in the positive Y direction, an increase in negative (right) rudder is required to maintain trim in yaw angle. Without this, the receiver would begin to yaw to the left, back towards its initial position, indicating positional stability in the yaw axis. These areas of positional stability are roughly analogous to those shown by Blake and Gingras and are thought to make close formation flight during the refuelling task easier for the pilot of the refuelling aircraft [32].

Figure 4.14 shows positional stability with respect to control surface deflections for trim with $\Phi = 0$. The aileron deflection stability is very similar to that of the $\Psi = 0$ trim condition, with a large area of positive stability, shown in orange,

between the wingtips of the C-130 tanker. However, the rudder deflection stability shows the opposite trend when compared to that of the $\Psi = 0$ trim strategy. The area of positive rudder deflection stability implies that as the aircraft moves in the positive Y direction, the amount of left rudder must be increased to maintain trim. Without this, the aircraft will tend to yaw to the right and continue slipping to the right. This suggests that a trim strategy involving yaw of the receiver instead of a bank angle strategy to maintain trim results in greater positional instability during AAR.

4.3.4 Phasor Analysis

Flying qualities defined in Refs. [68] and [69] are typically based on the natural frequencies and damping of the dynamic modes. When flying in a tanker wake, the closed-loop analysis does not predict a great change in eigenvalues compared to steady level flight, since the aerodynamic stiffness and damping do not change appreciably. However, while the eigenvalues themselves may not undergo great changes, the addition of an effective sideslip angle β and/or a bank angle Φ at trim leads to cross-coupling of the dynamic modes. To demonstrate this, a phasor plot can be seen in Figure 4.15 which visualizes the 9-state dynamic modes for the F/A-18 trimmed at the location of maximum roll angle with $\Theta = 5.72°$, $\Phi = 6.66°$, and $\Psi = 0.0°$. This location in the wake and its associated trim values are denoted by the annotated white boxes seen in Figures 4.7 through 4.12.

Each phasor shows the phase and normalized magnitude of the response of each degree of freedom for the dynamic mode with the indicated eigenvalue for six types of aircraft modes: heading, roll, short period, Dutch roll, spiral, and phugoid. Eigenvalues with an imaginary part will be oscillatory, whereas those with only negative real parts will show a decay response. The phasor plots are colour-coded such that eigenvector components associated with rotations about the x-axis shown in orange, the y-axis shown in purple, and the z-axis shown in blue respectively. While the short period mode mostly has components of α, q, and Θ, cross-coupling effects can be seen with the clear presence of p, Ψ, and Φ components, despite the fact that the short period is normally considered a purely longitudinal dynamic mode for most aircraft. Furthermore, there are small longitudinal components present in the eigenvectors of the Dutch roll mode. This cross-coupling is likely to result in undesirable handling qualities during the AAR task, since it will make performing precise manœuvres in a single axis very challenging for the receiver. However, given that this is the most extreme example in this work in terms of the maximum roll angle at trim, and likely the most unsuitable location for an AAR contact point behind a C-130 tanker, the dynamic modes given at a more favourable contact point will also be examined.

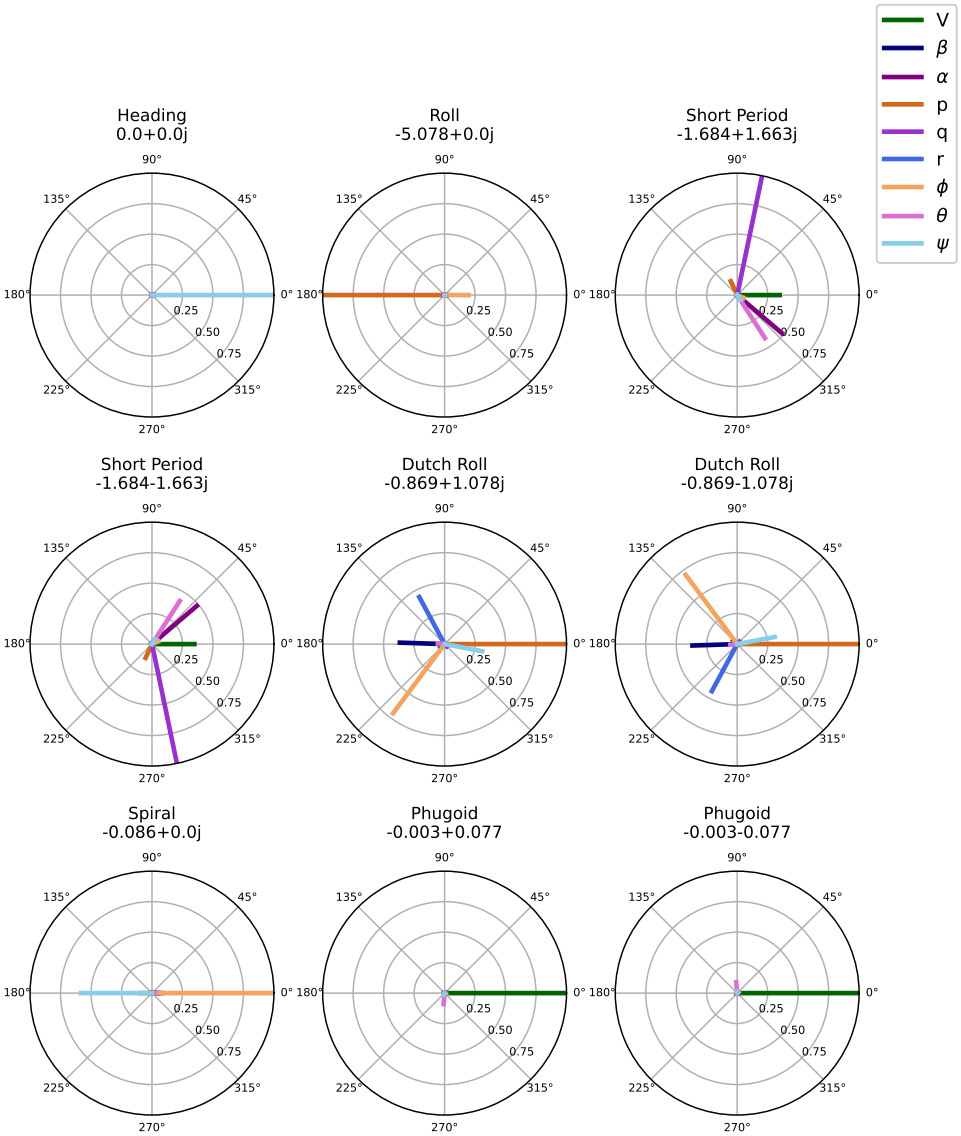

Figure 4.15: Phasor plot of the dynamic modes of an F/A-18 trimmed at $\Theta = 5.72°$, $\Phi = 6.66°$, and $\Psi = 0.0°$ in the C-130 wake, altitude 20 000 ft, Ma=0.54, longitudinal separation = 5 m..

A phasor plot of the 9-state dynamic modes for the F/A-18 trimmed at $\Theta = 5.53°$, $\Psi = -0.81°$, and $\Phi = 0.0°$ can be seen in Figure 4.16. This location in the wake and associated trim values is denoted with the black boxes seen in Figures 4.7 through 4.12.

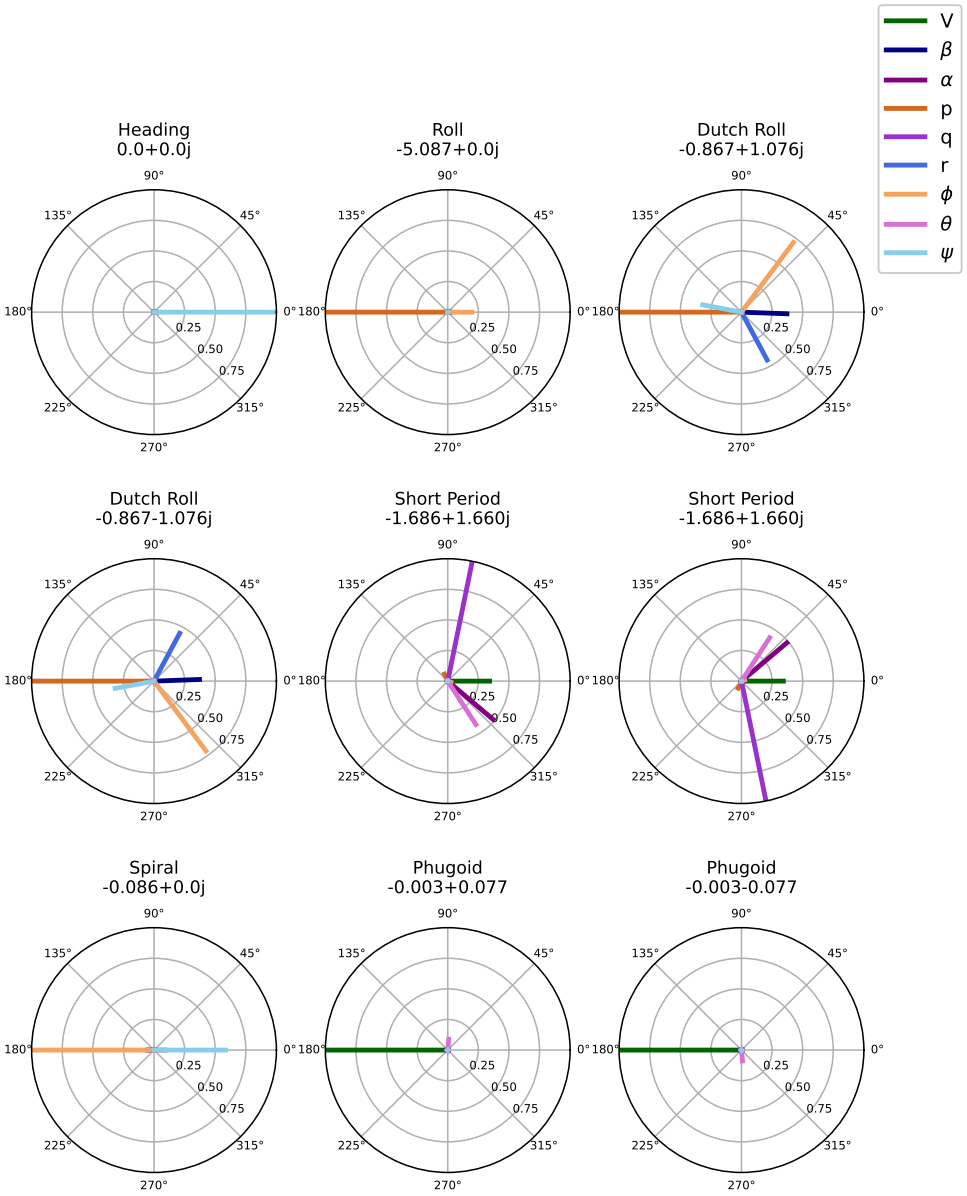

Figure 4.16: Phasor plot of the dynamic modes of an F/A-18 trimmed at $\Theta = 5.53°$, $\Psi = -0.81°$, and $\Phi = 0.0°$ in the C-130 wake, altitude 20 000 ft, Ma=0.54, longitudinal separation = 5 m..

Although Figure 4.16 shows no pitch-axis component in the Dutch roll phasors, a p component can still be seen in those of the short period mode. Given the nature of the precision manœuvring required during the drogue capture phase,

this p component may not be negligible despite being small in comparison to the longitudinal components of the short period mode. It is also notable that because this cross-coupling is observed at relatively low α, it cannot be the consequence of typical inertia cross-coupling observed in other fighter aircraft. Since this cross-coupling is predicted even at near-symmetrical trim conditions, a purely frequency-based analysis of the flying qualities such as those in Refs. [68] and [69] may not be sufficient to make handling qualities predictions for the AAR task, particularly in circumstances of light or moderate atmospheric turbulence where the receiver may be perturbed in any axis. This lends further credence to the work of Latimer and Klyde *et al.* who indicated that the flying qualities given in Refs. [68] and [69] are inadequate for predicting handling qualities for AAR tasks [70, 71].

The results presented in this section, *i.e.* trim states, control surface deflections, positional stability, and dynamic mode analysis, when examined individually, do not constitute a comprehensive picture of how challenging the AAR task will be for the receiver pilot. However, taken together, they present a holistic picture and allow for judgments to be made regarding which locations in the wake are likely to allow for the least challenging AAR process. The framework also enables the inclusion of frequency- and bandwidth-based flying qualities analysis. Further flight test data are needed to determine trim points and pilot handling quality ratings for the AAR task that can be cross-referenced against the framework outputs may eventually make it feasible to analytically predict handling qualities for any tanker-receiver pair. An example of analytic handling quality prediction will be demonstrated in Chapter 5, where a methodology will be introduced that uses calculation of longitudinal positional stability quantities $\frac{\partial C_L}{\partial \Delta z}$ and $\frac{\partial C_m}{\partial \Delta z}$ with frequency-based analyses to make determinations regarding receiver susceptibility to PIOs during AAR.

5 Pilot-Induced Oscillation Susceptibility During Flying Boom Refuelling

The ease with which the receiver can hold position relative to the tanker is not the only relevant factor when considering the feasibility of an AAR procedure. Pilots must also make precise flight manœuvres within the tanker wake in order to dock. The precision control required during the AAR task has been known to increase the likelihood of PIOs and several aircraft have been shown to be susceptible to PIOs while performing the AAR task as receivers or during high gain flight test manœuvres. Early flight tests showed that the C-17 was particularly prone to PIOs during the AAR procedure as a receiver. Iloputaife *et al.* strongly implicated a variety of causes for deficient handling qualities during AAR tasks, including the narrow frequency separation between the short period and control system dynamics, tanker exhaust impingement on the C-17 receiver horizontal stabilizer, and bow wave effects leading to poor static stability of the tanker [46]. In the longitudinal axis, this was alleviated in part by reducing the pitch control sensitivity, with further improvements to the flight control laws that minimized tendency towards PIOs during the AAR task documented by Weltz *et al.* [47].

The best PIO remediation is, of course, avoidance, and the identification of the potential for PIOs during the design process can save significant time and resources. In light of this, this chapter introduces a new analytical methodology for assessing the likelihood of PIO tendencies in the longitudinal axis of the receiver aircraft during the AAR tasks. This methodology considers both flight dynamics and pilot response to perturbations caused by changes in relative position between the tanker and receiver.

5.1 Methodology

This section introduces relevant flight dynamics and frequency domain analysis techniques for a new PIO susceptibility prediction method. It is then applied to two tanker-receiver pairs as test cases: a KC-135 tanker/C-5 receiver, and a KC-135 tanker/C-17 receiver. Although the receiver geometries are similar in that both receivers have a T-tail, the C-5 is much longer than the C-17 which means that it has a much larger moment of inertia resulting in significantly different pitch axis dynamics. These two similar aircraft have been selected for examination, because the C-17 has been reported to suffer from PIOs at high speeds during AAR before mitigation efforts [46, 47, 72], whereas the C-5 has not. Therefore, these two tanker-receiver pairs are excellent test cases that can demonstrate the ability of the analysis method's to characterize the flying qualities of two similar aircraft in the same task.

5.1.1 Positional Static Margin

Very early computational studies by Bloy, Ali, and Trochalidis found that the instability in the longitudinal axis was dependant on the differences in downwash gradients experienced by the wing and the tail [9, 10]. Blake and Gingras also discussed positional static stability [32], a matter that has been discussed in Chapters 3 and 4. Using both wind tunnel and potential flow calculations, they investigated positional stability derivatives including $\frac{\partial C_L}{\partial \Delta z}$ and $\frac{\partial C_m}{\partial \Delta z}$. The former is the change in lift per change in vertical separation, and the latter is the change in pitching moment per change in vertical separation. For typical stability axes, positional static stability requires that

$$C_{L,\Delta z} = \frac{\partial C_L}{\partial \Delta z} > 0 \qquad \text{and} \qquad C_{m,\Delta z} = \frac{\partial C_m}{\partial \Delta z} > 0 \tag{5.1}$$

so, to ensure positional static stability, an increase in vertical separation between the tanker and receiver should result in an increase in lift coefficient and a nose up pitching moment. A trimmed receiver aircraft is typically positionally stable with a positive value of $C_{L,\Delta z}$ when flying below the tanker. As vertical separation between tanker and receiver increases, the amount of downwash encountered by the receiver decreases. Assuming no change in the pitch angle of the receiver, this reduced downwash results in an increased effective angle of attack, which increases the amount of lift generated by the receiver, resulting in a restorative lifting force. However, in the pitch axis, as vertical separation between tanker and receiver increases, and the amount of downwash encountered by the receiver decreases, the increase in lift generated by the receiver should result in a nose-down pitching moment, assuming the receiver has a negative $C_{m,\alpha}$. In order to

quantify the positional static stability, a new quantity called Positional Static Margin (SM_P) is introduced using the terms in Equation 5.1. In flight dynamics, static margin (SM) quantifies the normalized distance from an aircraft's neutral point to its centre of gravity (CG) by relating the $C_{m,\alpha}$ and $C_{L,\alpha}$ curves at a particular trim point as follows:

$$SM = -\frac{C_{m,\alpha}}{C_{L,\alpha}} \tag{5.2}$$

The positional static margin uses an analogous form by relating the partial derivatives of C_L and C_m with respect to changes in position between tanker and receiver.

$$SM_P = \frac{C_{m,\Delta z}}{C_{L,\Delta z}} \tag{5.3}$$

While SM_P can also be a quantity of interest during PDR, it is not being examined in that context here. By examining FBR, which occurs close to the tanker's centreline, any asymmetric flight conditions in the lateral-directional axis can be minimized or eliminated, thus making the longitudinal stability of the receiver far more relevant than its lateral/directional stability. In this chapter, the values of the positional stability derivatives $C_{L,\Delta z}$ and $C_{m,\Delta z}$ for the receiver at various vertical separations between tanker and receiver are calculated using the methodology outlined in Chapter 3 and demonstrated in Chapter 4. This methodology is particularly useful since analysis of different tanker-receiver pairs at various vertical separations and flight conditions can be performed quickly.

5.1.2 Longitudinal Axis Approximation

In the Chapter 4, an AAR analysis method was introduced in which VLM data were combined with a closed-form aerodynamic model to analyze the receiver's flight dynamics. Here, a simplified version of that methodology that only considers the longitudinal axis is applied. By only analyzing one axis, the complexity of the aerodynamic model is reduced, and results can be generated with less aerodynamic data. Consider Equation 5.4, the longitudinal axis short period approximation, Schmidt [73], where the state variables are α and q, and the state matrix and input vector terms are defined in Table 5.1.

$$\begin{Bmatrix} \dot{\alpha} \\ \dot{q} \end{Bmatrix} = \begin{bmatrix} Z_\alpha/U_\infty & 1 \\ (M_\alpha + \frac{M_{\dot{\alpha}} Z_\alpha}{U_\infty}) & (M_q + M_{\dot{\alpha}}) \end{bmatrix} \begin{Bmatrix} \alpha \\ q \end{Bmatrix} + \begin{Bmatrix} Z_\delta/U_\infty \\ (M_\delta + \frac{M_{\dot{\alpha}} Z_\delta}{U_\infty}) \end{Bmatrix} \delta_e \tag{5.4}$$

Table 5.1: Dimensional Longitudinal stability derivatives [73]

Term	Description	Units
M_α	$\frac{QSc}{I_y}C_{m,\alpha}$	s^{-2}
$M_{\dot{\alpha}}$	$\frac{QSc}{I_y}\left(\frac{c}{2V}\right)\frac{\partial C_m}{\partial(\dot{\alpha}c/2V)}$	s^{-1}
M_q	$\frac{QSc}{I_y}\left(\frac{c}{2V}\right)\frac{\partial C_m}{\partial(qc/2V)}$	s^{-1}
M_δ	$\frac{QSc}{I_y}C_{m,\delta_e}$	s^{-2}
Z_α	$\frac{QS}{m}(C_D - C_{L,\alpha})$	$\mathrm{m{\cdot}s}^{-2}$
Z_δ	$\frac{QS}{m}C_{L,\delta_e}$	$\mathrm{m{\cdot}s}^{-2}$

Consider also the effect of a change in displacement between the tanker and receiver. Positional stability can be dimensionalized like the quantities in Table 5.1 as follows:

$$Z_{\Delta z} = \frac{QS}{m}C_{L,\Delta z} \tag{5.5}$$

$$M_{\Delta z} = \frac{QSc}{I_y}C_{m,\Delta z} \tag{5.6}$$

Equation 5.4 can then be modified to include the changes in pitching moment and lifting moment per unit change in vertical separation.

$$\begin{Bmatrix}\dot{\alpha}\\ \dot{q}\end{Bmatrix} = \begin{bmatrix} Z_\alpha/U_\infty & 1 \\ (M_\alpha + \frac{M_{\dot{\alpha}}Z_\alpha}{U_\infty}) & (M_q + M_{\dot{\alpha}})\end{bmatrix}\begin{Bmatrix}\alpha\\ q\end{Bmatrix} + \begin{Bmatrix} Z_\delta/U_\infty \\ (M_\delta + \frac{M_{\dot{\alpha}}Z_\delta}{U_\infty})\end{Bmatrix}\delta_e + \begin{Bmatrix} Z_{\Delta z}/U_\infty \\ M_{\Delta z}\end{Bmatrix}\Delta(\Delta z) \tag{5.7}$$

The previous work of Taschner, Wang *et al.*, and Yin *et al.* has demonstrated the relevance of flight path angle response to both AAR handling qualities and PIO avoidance [48, 52, 53]. The flight path angle can be approximated through the q state using the transfer function shown in Equation 5.8.

$$\frac{\gamma(s)}{q(s)} \approx \frac{L_\alpha}{s^2 + L_\alpha s} \tag{5.8}$$

In Equation 5.8, L_α is the derivative of the lift force with respect to angle of attack, normalized by the mass of the aircraft and U_∞ as shown in Equation 5.9.

$$L_\alpha = \frac{\partial L}{\partial \alpha}\frac{m}{U_\infty} \tag{5.9}$$

To perform an analysis in the frequency domain and to produce Bode plots, a harmonic forcing with frequency ω is assumed based on small fluctuations in the position of the tanker and the receiver. This takes the form $\sin(\omega t)\Delta z$. The changes in $\dot{\alpha}$ and $\dot{q}$ from this external forcing are then assumed to be directly proportional to the $Z_{\Delta z}$ and $M_{\Delta z}$ terms. It is also assumed that there will be some time lag between when the change in airflow in the wake interacts with the receiver's wing and when it interacts with the receiver's tail. This time lag is assumed to be the distance between the wing and the horizontal tail divided by U_∞ and is accounted for using a phase shift $-\phi$. Therefore, the total affect on $\dot{\alpha}$ and $\dot{q}$ is assumed to be:

$$\begin{Bmatrix} \Delta\dot{\alpha}(t) \\ \Delta\dot{q}(t) \end{Bmatrix} = \begin{Bmatrix} (Z_{\Delta z}/U_\infty)\sin(\omega t) \\ M_{\Delta z}\sin(\omega t - \phi) \end{Bmatrix} \Delta(\Delta z) \tag{5.10}$$

and this term is fully integrated into the short period approximation.

$$\begin{Bmatrix} \dot{\alpha} \\ \dot{q} \end{Bmatrix} = \begin{bmatrix} Z_\alpha/U_\infty & 1 \\ (M_\alpha + \frac{M_{\dot{\alpha}}Z_\alpha}{U_\infty}) & (M_q + M_{\dot{\alpha}}) \end{bmatrix} \begin{Bmatrix} \alpha \\ q \end{Bmatrix} + \begin{Bmatrix} Z_\delta/U_\infty \\ (M_\delta + \frac{M_{\dot{\alpha}}Z_\delta}{U_\infty}) \end{Bmatrix} \delta_e + \begin{Bmatrix} (Z_{\Delta z}/U_\infty)\sin(\omega t) \\ M_{\Delta z}\sin(\omega t - \phi) \end{Bmatrix} \Delta(\Delta z) \tag{5.11}$$

For a negative value of SM_P, this essentially results in a forcing of the pitching moment and lifting force that is 180 degrees out of phase, minus the phase shift due to time lag.

It is safe to assume that the pilot of the receiver wishes to keep the flight path angle constant throughout the AAR procedure, and therefore will be making compensatory control adjustments. The pilot behaviour and control stick position, c_p, are approximated here by a Tustin pilot model [74]. In equation 5.12, the transfer function of the pilot's control behaviour, Y_P, is approximated by assuming some gain K_p, an anticipation time-lead constant T_L, and a time delay constant τ.

$$Y_P = \frac{c_p(s)}{e(s)} = \frac{K_p(1 + T_L s)e^{-\tau s}}{s} \tag{5.12}$$

In the Tustin model, the gain K_p and time delay constant τ are representative of the pilot's observational and neuromuscular limitations, and the time-lead constant T_L is representative of the pilot's experience and ability to predict the behaviour of the aircraft. A more sophisticated model, which is commonly referred to as the *Precision model*, was developed by McRuer (Equation 5.13).

$$Y_P = \frac{c_p(s)}{e(s)} = K_p e^{-\tau s} \frac{T_L s + 1}{T_I s + 1} \left(\frac{1}{(T_N s + 1)\left(\frac{s^2}{\omega_n^2} + \frac{2\zeta}{\omega_n} s + 1\right)} \right) \tag{5.13}$$

As in the Tustin model, the Precision model makes use of both a pilot gain term (K_p) and time delay term ($e^{\tau s}$), but it also adds a lag-lead component and terms representing the neuromuscular actuation system [75]. In this work, the neuromuscular terms are set to nominal values of $T_I = 6.53$, $T_N = 0.0825$, $\omega_n = 16$ rad/s, and $\zeta = 0.6$ [75]. A schematic of the closed loop system can be seen in Figure 5.1.

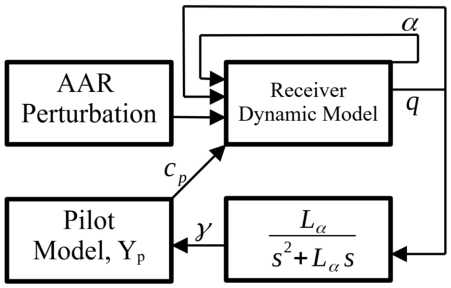

Figure 5.1: Closed-loop *Simulink* model block diagram.

Based on this, the analysis proposed here is to examine $|\frac{\gamma}{\Delta z}(j\omega)|$, $\angle\frac{\gamma}{\Delta z}(j\omega)$, and $\angle\frac{\gamma}{\delta}(j\omega)$ based on the different values of $C_{m,\Delta z}$, $C_{L,\Delta z}$, and SM_P at different vertical separations for the C-17 and C-5 receivers. The values of $C_{m,\Delta z}$, $C_{L,\Delta z}$, and SM_P were calculated using the methodology outlined in Chapters 3 and 4, and the frequency analyses and time-resolved simulations were performed in *MATLAB/Simulink*. It should also be noted that although this technique of frequency analysis is common in other flying qualities frameworks, sinusoidal perturbations and inputs are not necessarily typical during AAR. However, determining critical frequencies and the aircraft response at various input frequencies can still be part of a useful framework for AAR handling qualities prediction, as will now be demonstrated.

5.1.3 Model Validation

In order to find reasonable values for the pilot gain K_p, a step target analysis was performed. In the step target analysis, a desired pitch angle is set, in this case 10 degrees, and then the pilot is instructed to acquire the target as soon as possible without overshoot, and to stay on the target. Flight test data for this step target analysis was provided in Iloputaife [72], and this was used to also estimate the C-17's longitudinal stability derivatives, assuming a simple control system of the form seen in Figure 5.2.

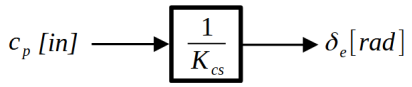

Figure 5.2: C-17 control system block diagram.

Elevator deflection rate limiting of 12 deg/s was also assumed. A comparison of the model behaviour with flight test data found in Iloputaife [72] can be seen in Figure 5.3. The pilot model response was achieved by setting the reference signal to 10 degrees pitch from an initial condition of 0 degrees pitch.

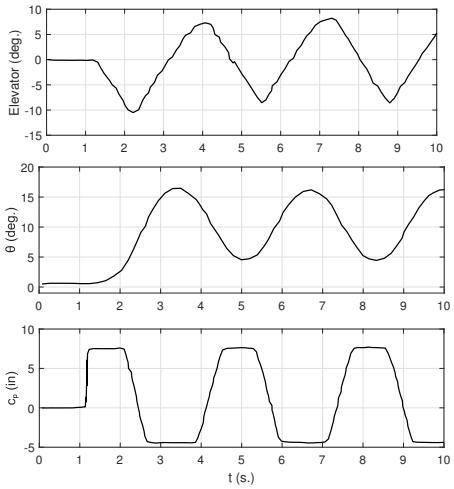

(a) C-17 flight test [72]

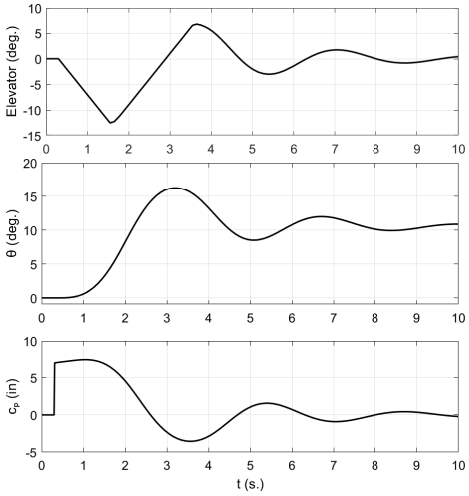

(b) Tustin model output

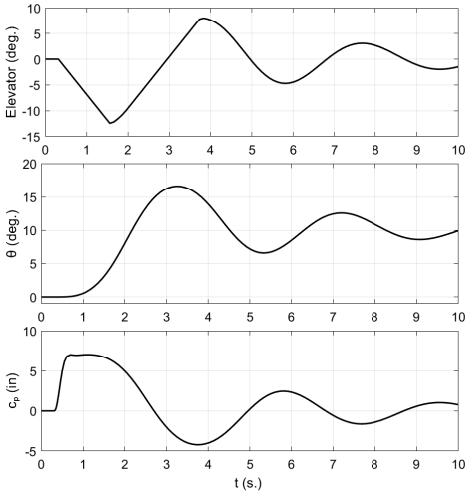

(c) Precision model output

Figure 5.3: Flight test and pilot model results of a C-17 pitch step target test.

The C-17 demonstrated PIO tendencies in this test before various changes were made to the control system. This version of the C-17 was used to derive values for the C-17 dynamic model and the Tustin and Precision pilot models. The resulting C-17 simulation controlled by the Tustin pilot model demonstrates similar rates and maxima in elevator deflection, pitch, and stick position when compared to the C-17 flight test, and the Precision pilot model exhibits almost identical rates and maxima in terms of elevator deflection, pitch, and stick position. The greatest difference between the two pilot models is that the Tustin model exhibits a period of oscillation about the pitch target of 10 degrees that is roughly 0.5 seconds longer than that of the flight test, whereas the Precision model's oscillations are roughly 0.3 longer than those of the Tustin model. The most notable difference between the flight tests and simulations is that the simulated C-17 controlled by the pilot models does not go into PIOs. This is largely due to the nature of the pilot model response, which is essentially a modified proportional-integral controller. Such a controller will not provide the extremely rapid changes in control stick input recorded in the flight test, thus giving the natural damping characteristics of the airplane time to damp out any oscillatory pitch behaviour. This makes the pilot model useful to establish a baseline best-case pilot response, something that is consistent across all flight conditions and aircraft configurations. Undesirable behaviour encountered in this best-case scenario is unlikely to be improved by the input of a human pilot.

The required longitudinal stability derivatives for the C-5 were taken from Heffley and Jewell [76]. Furthermore, a simplified control system without influence of additional stability augmentation systems was created based on that report, the general form of which can be seen in Figure 5.4.

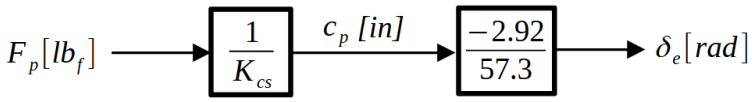

Figure 5.4: C-5 control system block diagram [76].

The control system converts a stick force F_p into a control stick position, c_p, based on the control system gain K_{cs} which at nominal refuelling conditions was assumed to be 28 lbs/in. This control stick position is then converted into an elevator deflection. In order to determine reasonable values of K_p, the step target analysis was again performed, and the pilot response was tuned such that the maximum stick force provided was 75 lb_f. Although this may seem large, the C-5's stick stiffness at nominal refuelling conditions is 28 lbs/in., so a stick force

of 75 lb_f represents a stick travel of 2.67 in, which is about one third of that of the C-17. The pilot model parameters derived and used are given in Table 5.2.

Table 5.2: Pilot Model Parameters

Aircraft (Pilot Model)	K_p	K_{cs}	T_L	τ
C-17 (Tustin)	4	30	10	0.3
C-17 (Precision)	60	30	10	0.3
C-5 (Tustin)	40	28	10	0.3
C-5 (Precision)	600	28	10	0.3

The gains for the two models cannot be directly compared, since the C-17's pilot model is assumed to provide a stick displacement c_p, whereas the C-5's control system requires a pilot stick force F_p as input. However, the gains for each pilot model can be considered equal for both aircraft if a stick stiffness of 10 lb_f/in for the C-17 is assumed.

5.1.4 Frequency Domain Analysis

The proportional-integral controllers that model pilot behaviour provide a control input that is proportional to both the magnitude of an error signal, and its duration. In this analysis, this error is the induced deviation from a 0 degree flight path angle. For the perturbation of α and q given in Equation 5.10, the error signal will be constantly changing at the perturbation frequency ω, and therefore both the response of the pilot model and the aircraft itself will also be at this frequency. However, the aircraft and pilot response will be out of phase with the perturbation up to a certain frequency. For an ideal perturbation response, the receiver and the tanker will move in phase, representing a minimal change in vertical separation between the receiver and the tanker. To demonstrate, consider the following refuelling procedure taking place at Ma = 0.54, 20 000 ft MSL altitude between a KC-135 tanker a C-17 receiver. It is assumed that $C_{m,\Delta z} = 6.71 \times 10^{-3}$ and $C_{L,\Delta z} z = 4.37 \times 10^{-3}$ and that the a 0.5 m peak-to-peak variation in the vertical position of the tanker relative to the receiver is causing the receiver's flight path angle to change. Figure 5.5 compares the responses of a receiver controlled by a Tustin pilot model at perturbation frequencies of 1.88 rad/s and 1.2 rad/s.

It can be seen in Figure 5.5a that the flight path angle oscillation is in phase with the vertical movement of the tanker, which minimizes the change in vertical distance between the tanker and receiver. For comparison, at the perturbation

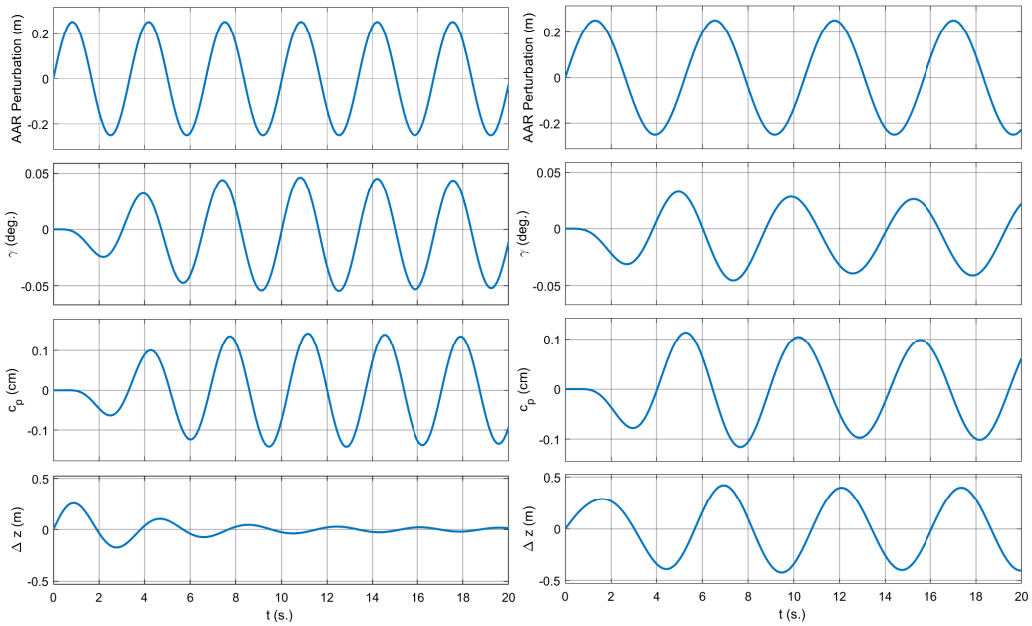

(a) $f = 1.88$ rad/s. (b) $f = 1.20$ rad/s.

Figure 5.5: C-17 receiver and pilot response to an external perturbation.

frequency of 1.2 rad/s, seen Figure 5.5b, the change in vertical position of the tanker and the response of the receiver are nearly 180 degrees out of phase, resulting in a large variation in Δz over time. It can be assumed that in a real flight scenario, the pilot will be capable of providing inputs at higher frequencies than some low frequency perturbations in order to keep the flight path of the receiver in phase with that of the tanker. The frequency at which the perturbation and modelled aircraft response is in phase is representative of the minimum frequency at which a real receiver pilot must make adjustments to compensate for aerodynamic forces due to changes in the tanker position, while minimizing any changes in vertical separation between the tanker and receiver. This frequency can be determined using Bode plots.

To demonstrate, consider a C-17 receiver and a KC-135 tanker refuelling at 20 000 ft MSL and Ma = 0.54. Assuming a vertical separation between tanker and receiver of $\Delta z = 8.0$ m, the values of $C_{m,\Delta z} = -7.2 \times 10^{-3}$ and $C_{L,\Delta z} = 4.5 \times 10^{-3}$ were calculated. Figure 5.6 shows a typical Bode plot examining the response of the flight path angle γ and the response of the pilot, represented by the stick position c_p measured in cm.

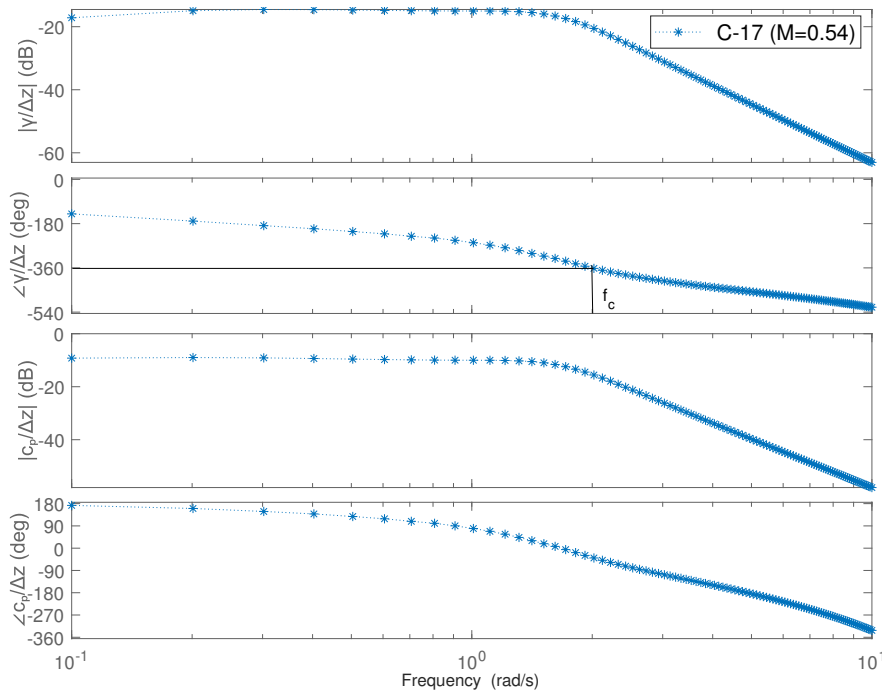

Figure 5.6: Bode plot of a C-17 receiver and pilot response to a vertical separation perturbation. $\text{Ma}_\infty = 0.54$, $\Delta z = 8.0\text{m}$, $C_{m,\Delta z} = -7.2 \times 10^{-3}$ and $C_{L,\Delta z} = 4.5 \times 10^{-3}$.

The three poles of the dynamic system are evidenced by the -60 dB/decade slope of the $|\frac{\gamma}{\Delta z}|$ and $|\frac{c_p}{\Delta z}|$ sections of Figure 5.6. Given the negative value of $C_{m,\Delta z}$, an increase in separation between the aircraft will result in a nose down pitching moment. This is represented in the Bode plot by the response of γ and c_p being close to 180 degrees out of phase with the perturbation at low frequencies. As frequency increases, the phase difference between the perturbation and the aircraft and pilot response tends to zero degrees at some frequency, f_c, where $\angle\frac{\gamma}{\Delta z}(f_c) = 0$, referred to as the *crossover frequency*. The crossover frequency of γ shown in Figure 5.6 is 2 rad/s. Therefore, it is predicted that manœuvers during the AAR procedure must be performed by the pilot at a frequency no less than 2 rad/s, or the flight path response and relative separation between tanker and receiver will fall out of phase. An example of the aircraft and pilot response at this crossover frequency of 2 rad/s can be seen in Figure 5.7.

Figure 5.7 shows the aircraft flight path angle response in phase with the perturbation, with the pilot response slightly lagging in phase behind the flight path angle response. This phase lag is largely a function of the Tustin model time de-

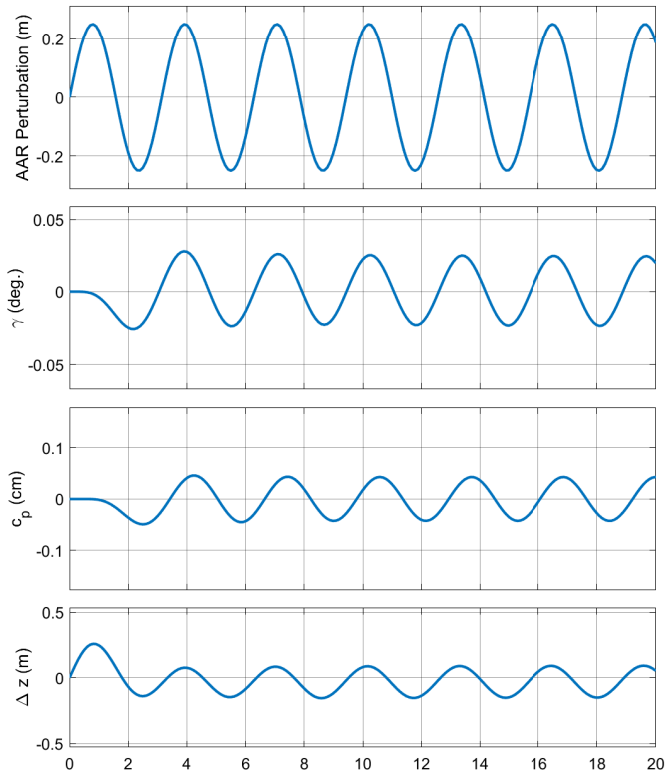

Figure 5.7: C-17 aircraft and pilot response to an external perturbation at a frequency of 2.0 rad/s, and initial vertical separation of 8.0 m.

lay constant, τ, and can be artificially removed by arbitrarily setting $\tau = 0$. The aircraft response to external perturbation at $\Delta z = 8.0$m can be contrasted to the Bode plot of the same flight condition, where $\Delta z = 7.0$m, $C_{m,\Delta z} = 4.0 \times 10^{-3}$, and $C_{L,\Delta z} = 1.2 \times 10^{-3}$, seen in Figure 5.8.

The positive values of $C_{m,\Delta z}$ mean that an increase in vertical separation between tanker and receiver will result in a pitch up moment in the receiver, and similarly a decrease in vertical separation between tanker and receiver will result in a pitch down moment in the receiver. This is reflected in Figure 5.8, where it can be seen that the crossover frequency is very low. This implies that the minimum frequency of inputs that will allow the pilot to control the receiver's flight path at this vertical separation is very slow, since the receiver is stable with respect to its position relative to the tanker. The aircraft and pilot response at this very low crossover frequency can be seen in Figure 5.9.

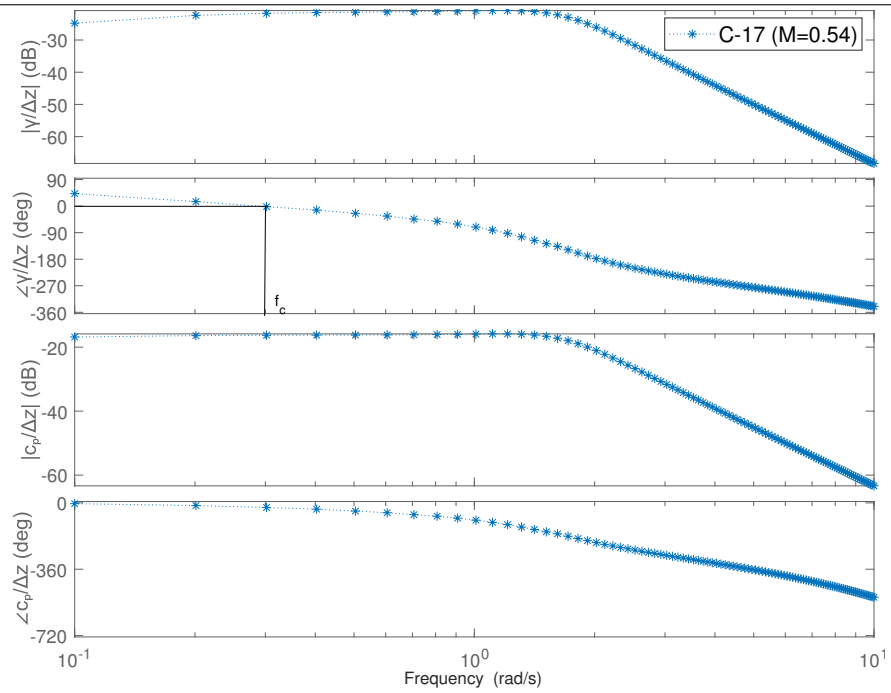

Figure 5.8: Bode plot of a C-17 receiver and pilot response to a perturbation caused by a change in vertical separation between tanker and receiver. $\mathrm{Ma}_\infty = 0.54$, $\Delta z = 7.0$m, $C_{m,\Delta z} = 4.0 \times 10^{-3}$, and $C_{L,\Delta z} = 1.2 \times 10^{-3}$.

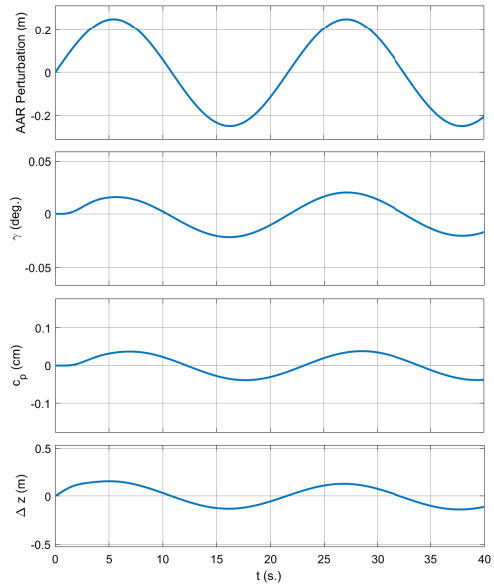

Figure 5.9: C-17 receiver and pilot response to an external perturbation at a frequency of 0.3 rad/s. $\mathrm{Ma}_\infty = 0.54$, $\Delta z = 7.0$m,

Given the very slow external forcing and aircraft response, it is easy to see that a pilot reaction that occurs at a higher frequency than that of the perturbation will be capable of keeping the change in γ throughout the oscillation close to 0. Likewise, it can be seen in Figure 5.7 that a slower pilot input will result in the aircraft falling out of phase with the perturbation. This is why the crossover frequency, f_c, was selected as the frequency of interest for the analysis.

Figure 5.7 also shows a clear phase difference between the pilot input, c_p, and the flight path angle. Based on the crossover frequency and the phase difference between the pilot and the aircraft response at the crossover frequency, ϕ_{c_p}, the time delay margin is defined as shown in Equation 5.14.

$$\tau_{d_{\mathrm{m}}} = \frac{\frac{\pi}{2} - \phi_{c_p}}{f_c} \tag{5.14}$$

The time delay margin is a measure of how much total system equivalent time delay can be allowed in the higher order system before the pilot and aircraft response become 90 degrees out of phase at the crossover frequency, assuming a pilot reaction time of 0.3s. For example, in Figure 5.7 the pilot model is -39.5° out of phase with the aircraft response. This gives a time delay margin of 0.44 seconds. Figure 5.10 shows the receiver and pilot response for the refuelling condition seen in Figure 5.7 where the pilot time delay constant has been increased from 0.3 seconds to 0.744 seconds.

In Figure 5.10, although the receiver response itself remains mostly in phase with the AAR perturbation, it can be seen that the pilot is now 90 degrees out of phase with the response of the flight path angle, as predicted by the time delay margin. Pilot inputs being out of phase with the aircraft response are one of the main markers of PIOs, along with the magnitude of the pilot inputs themselves. The magnitude of the pilot response to the external perturbation can also be examined in Bode plots. Therefore, the following quantities of interest will be examined for the case of the C-5 and C-17 refuelling at various flight conditions:

- Positional static margin
- Crossover frequencies
- Pilot input resonance vs. pilot compensation phase at f_c
- Pilot input resonance vs. time delay margin

These will be evaluated in terms of their ability to make predictions about the likelihood of PIOs during AAR, thereby providing a new technique for AAR analysis capable of predicting PIO susceptibility in the receiver.

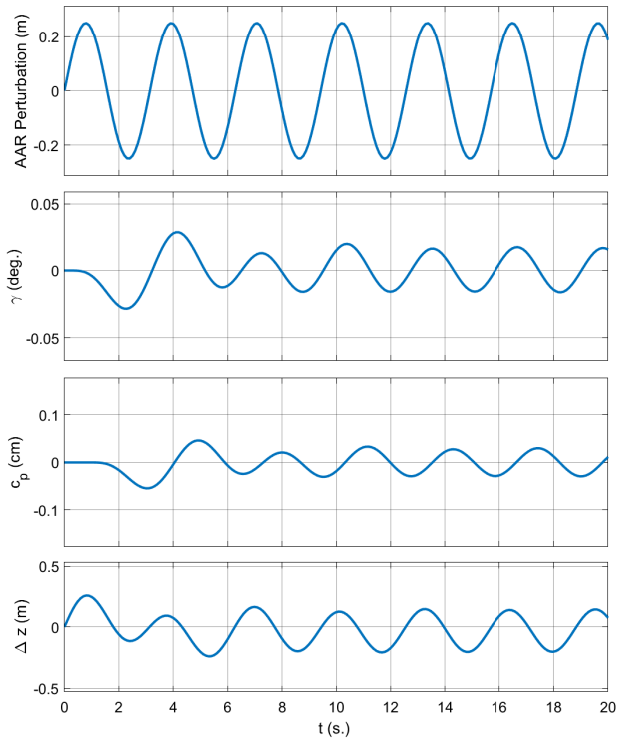

Figure 5.10: C-17 aircraft and pilot response to an external perturbation at a frequency of 2.0 rad/s when the pilot reaction time is increased to 0.74 seconds. $\mathrm{Ma}_\infty = 0.54$, $\Delta z = 7.0$m,

5.2 Analysis of the C-17 and C-5

Table 5.3: refuelling Conditions

Parameter	Value	Units
Airspeeds	144.2, 170.6, 212.5	m/s
Altitude	20 000	ft
ρ_∞	0.653	kg/m^3
a	316	m/s
Ma_∞	0.46, 0.54, 0.67	-

The three flight conditions examined can be seen in Table 5.3 and a typical alignment of the aircraft during AAR is illustrated in Figure 5.11. Both receivers are depicted at the approximate contact point. The three flight conditions chosen correspond to a low speed, nominal, and high speed refuelling process at 20 000 ft. Notably, Ma = 0.67 was the point at which the C-17 began to exhibit PIO tendencies during refuelling [46].

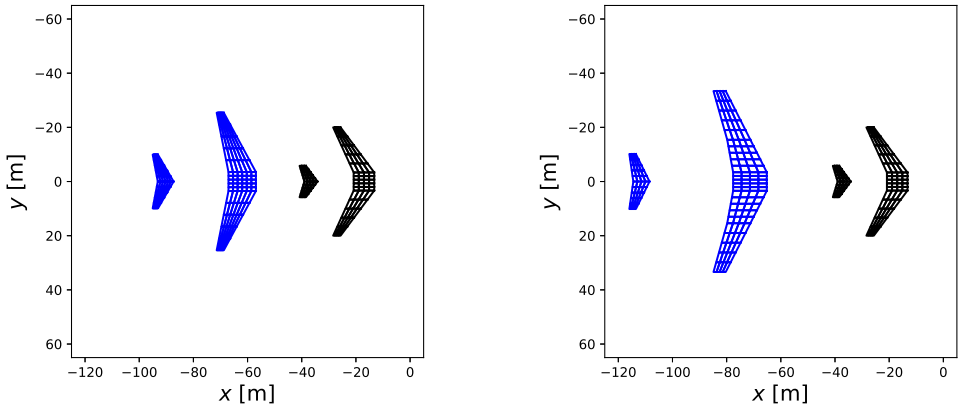

(a) KC-135 tanker with C-17 receiver (b) KC-135 tanker with C-5 receiver

Figure 5.11: Typical alignment of tanker and receiver lifting surfaces during AAR.

A comparison of the longitudinal positional static stability at various vertical separations can be seen in Figure 5.12. The vertical separation between the tanker and receiver, Δz, is measured from the level of the wing planform of the tanker at $y = 0$ to the level of the wing planform of the receiver at $y = 0$. Note that there are small data gaps in Figure 5.12 at certain Δz where interactions between the receiver VLM model and the tanker wake caused non-physical spikes in $C_{m,\Delta z}$ and $C_{L,\Delta z}$, and therefore the data are presented here.

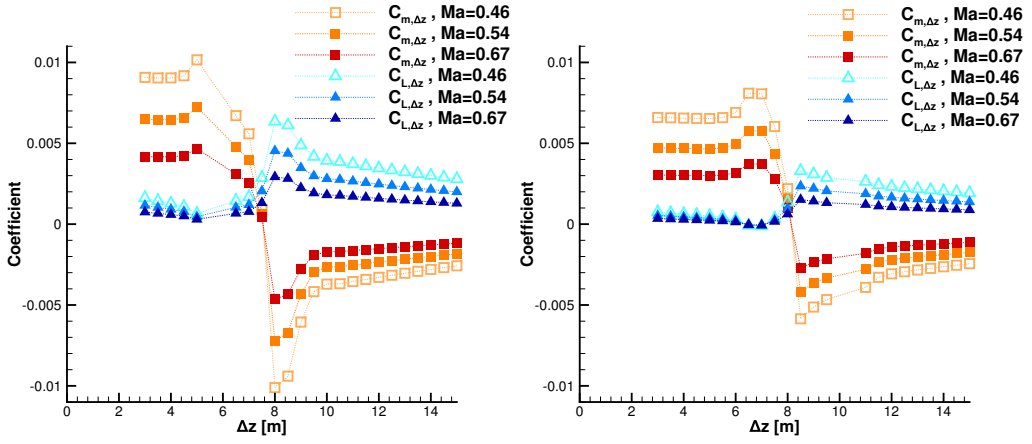

(a) C-17 (b) C-5

Figure 5.12: Comparison of longitudinal positional static stability of a C-17 and C-5 receiver during aerial refuelling at various vertical separations.

The C-17 and C-5 both demonstrate similar positional static stability traits, showing a positive value for $C_{m,\Delta z}$ and a smaller value of $C_{L,\Delta z}$ at smaller vertical separations up until some crossover point. This is due to the height difference between the wing and tail planforms. At small vertical separations, as the receiver moves downwards, the main wings encounter less downwash leading to increased lift. By contrast, the tail encounters more downwash, which increases the nose-up pitching moment on the entire aircraft. This persists as the vertical separation increases until the tail passes through the region of maximum downwash. After this point, the downwash decreases with increased vertical separation, increasing the lift generated by the tail, and resulting in a nose-down pitching moment. The crossover point occurs around $\Delta z = 7.5$ m for the C-17, and around $\Delta z = 8$ m for the C-5. This crossover point is the vertical separation at which the level of each receiver's tail is between the level of the tanker's horizontal stabilizer and wing. After this crossover point, $C_{m,\Delta z}$ becomes negative, and $C_{L,\Delta z}$ becomes more positive, with the C-17 exhibiting greater sensitivity to small changes in relative position. The region of greatest sensitivity corresponds to the T-tail being just below the level of the receiver wings, and therefore in the region of maximum downwash. The flying boom of the KC-135 extends between 6.5m and 9m vertically, and therefore this is the range of vertical separations that will be considered in the following figures. The KC-135 typically prefers to refuel at as large a vertical separation as possible so as to limit the bow wave effect from the much larger aircraft that is being refueled.

A summary of the crossover frequencies for the C-17 and C-5 receivers at vertical separations between 6.5 m and 9.0 m is presented in Figure 5.13. In general, crossover frequency is a function of positional static stability at each vertical separation, although the exact crossover frequency is still dependent on flight condition, aircraft dynamic characteristics, and pilot model. For the C-17, the crossover frequencies predicted by the Precision model are slightly lower than those of the Tustin model. The crossover frequencies of the C-5 appear to be independent of the pilot model chosen, since there is no significant difference between the crossover frequencies exhibited by the Tustin and Precision models. The magnitude of the pilot model response (pilot input resonance) is also examined at crossover frequencies, as well as the phase difference between pilot input and aircraft response. This can be seen in Figure 5.14.

The pilot compensation phase shown in Figure 5.14 is the phase difference between the pilot and the response of the receiver flight path angle at the crossover frequency. This is a function of the time delay in the Tustin pilot model, and a function of both the time delay and lead/lag constants used in the Precision model. The pilot compensation phase of the C-5 increases with increased vertical

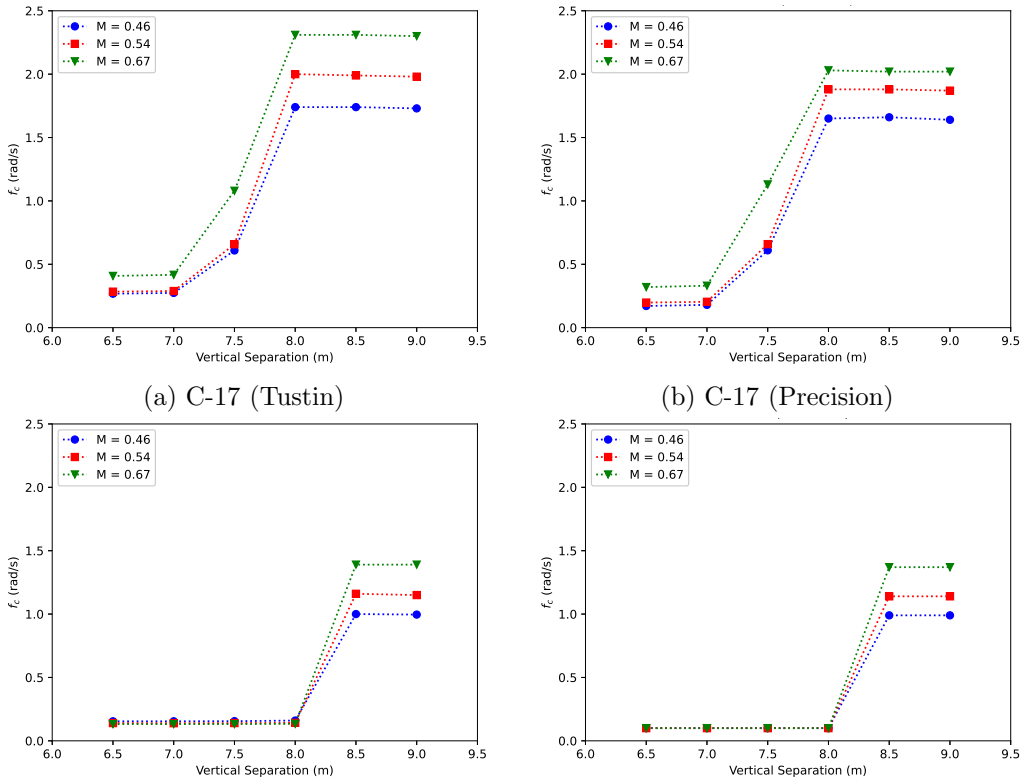

(a) C-17 (Tustin)

(b) C-17 (Precision)

(c) C-5 (Tustin)

(d) C-5 (Precision)

Figure 5.13: Predicted crossover frequencies for the C-17 and C-5.

separation between tanker and receiver according to results from the Precision pilot model, whereas the pilot compensation phase decreases with increased Δz according to the results from the Tustin model. Furthermore, the magnitude of the pilot input of the C-5 decreases with increased vertical separation, whereas the pilot input resonance of the C-17 drastically decreases at $\Delta z = 7.5$ m. This can be partially predicted using the SM_P values of both aircraft. The pilot input resonance values remain similar, however. Figure 5.15 compares the SM_P of both receivers at vertical separations from 6.5 m to 9 m in terms of the log of the absolute value of SM_P. At all examined airspeeds, the magnitude of both the $C_{L,\Delta z}$ and $C_{m,\Delta z}$ derivatives is reduced as airspeed increases, but interestingly, SM_P remains unchanged, suggesting that the relationship between positional stability quantities is a fundamental quality of the tanker-receiver pair, rather than a function of flight condition.

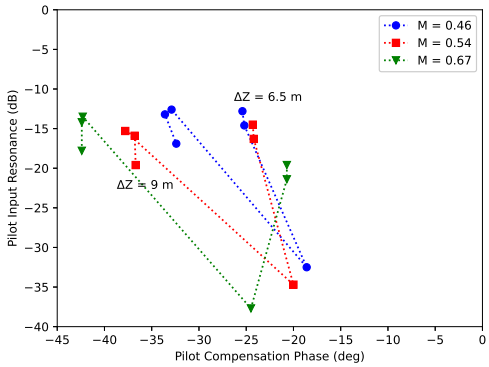

(a) C-17 (Tustin)

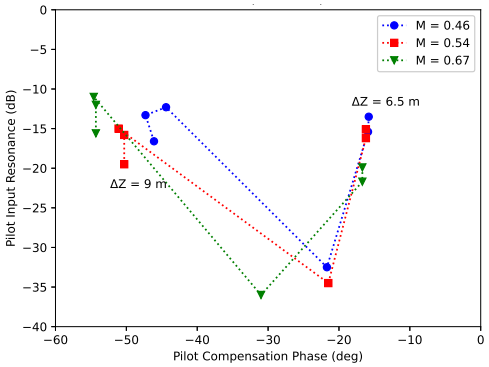

(b) C-17 (Precision)

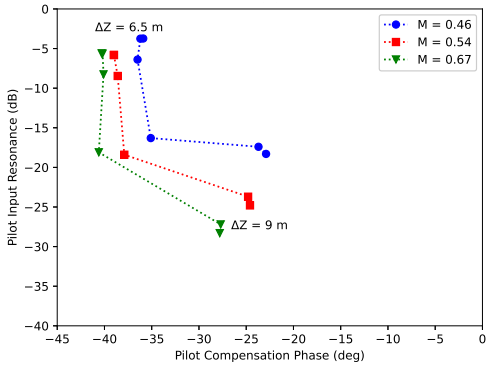

(c) C-5 (Tustin)

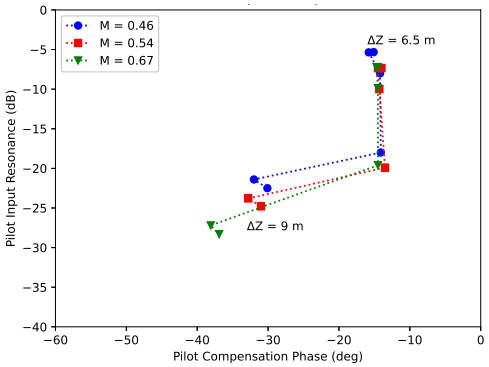

(d) C-5 (Precision)

Figure 5.14: Phase difference between pilot input and aircraft response and pilot input resonance at crossover frequency at various flight conditions and separations between tanker and receiver.

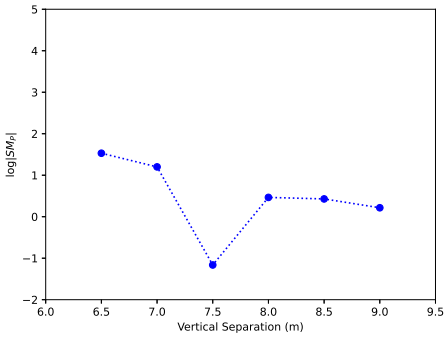

(a) C-17

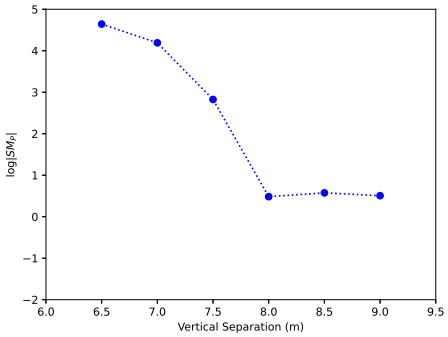

(b) C-5

Figure 5.15: $\log|SM_P|$ at various vertical separations between tanker and receiver.

The SM_P is much larger for the C-5 than for the C-17 at the smaller vertical separations, owing to the extremely small values of $C_{L,\Delta z}$ up to the crossover point. The C-17 exhibits one region at $\Delta z = 7.5$m where $C_{L,\Delta z}$ is much larger than $C_{m,\Delta z}$, resulting in a comparatively small value of SM_P. In general, it can be seen in Figure 5.14 that the magnitude of the pilot response is related to $\log|SM_P|$, although the precise relationship between to the magnitude of the pilot input is dependent on factors, such as gains within the closed loop system. Based on this, it can be assumed that the C-5 also has a vertical separation between $\Delta z = 8.0$ m and $\Delta z = 8.5$ m, at which the value of $\log|SM_P|$ is very small, due to neutral positional static stability in the pitch axis. This Goldilocks Zone of small $\log|SM_P|$ exists roughly at vertical separations where the horizontal tail plane is at a height between the tail plane and wing plane of the tanker. However, due to the larger tail of the C-5, this occurs at a larger vertical separation than that of the C-17, which is considered preferable for the KC-135 tanker. The time delay margin was calculated at all flight conditions from the crossover frequency and the phase difference between the pilot and the aircraft response at the crossover frequency. A comparison of the time delay margins can be seen in Figure 5.16.

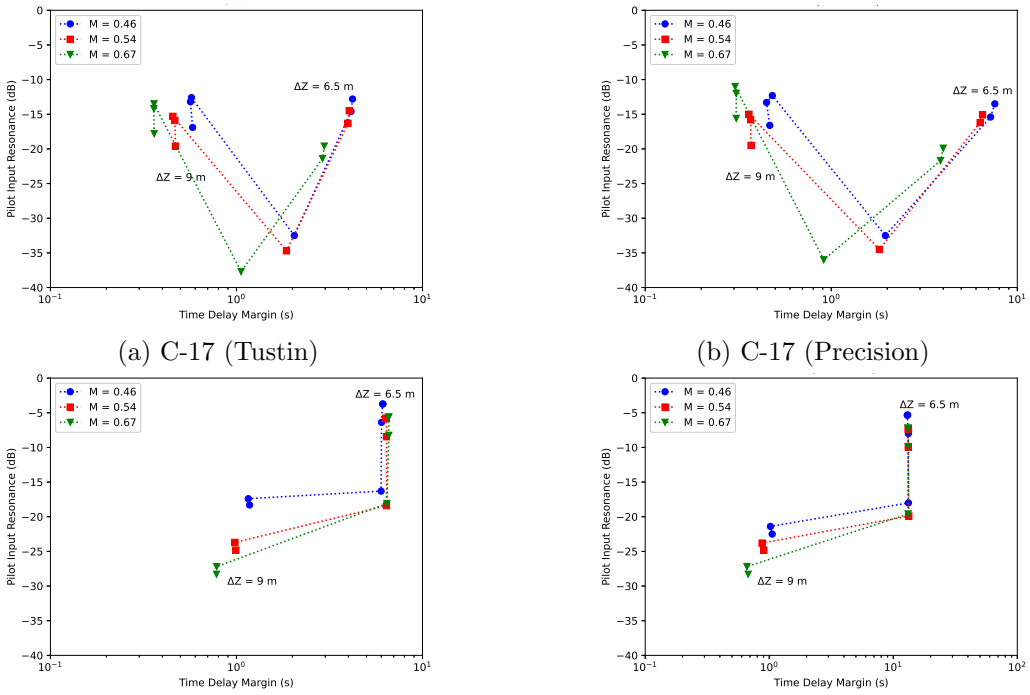

(a) C-17 (Tustin)

(b) C-17 (Precision)

(c) C-5 (Tustin)

(d) C-5 (Precision)

Figure 5.16: Time delay margin and pilot input resonance at various flight conditions and vertical separations.

Figure 5.16 shows that at small vertical separations, although the pilot input resonance is comparatively high, the low crossover frequency allows the pilot ample time to correct any effect of disturbances. As vertical separation increase, this time delay margin reduces down to the order of 1 second, but the pilot input resonance is reduced. This suggests favourable handling qualities for the pilot, where changes to pilot input based on disturbances from the tanker can be small and slow. By contrast, the time delay margin of the C-17 at vertical separations of 8.0 m to 9.0 m runs from 560 ms at low speeds to 360 ms at high speeds, and the pilot input resonance is also up to 10 dB higher than that of the C-5. Interestingly, the time delay margin suggested by both the Tustin and the Precision models are similar, since the lower crossover frequencies of the Precision model are counter-balanced by the increased pilot compensation phase, particularly at vertical separations between 8.0 m and 9.0 m. The Precision pilot model also predicts larger pilot input resonances than the Tustin model at $\mathrm{Ma}_\infty = 0.672$.

The combination of higher pilot input resonance and the requirement of shorter pilot input timescales leading to a lower time delay margins are likely to be factors indicative of the potential for PIOs during AAR tasks. To demonstrate this, a time trace of the aircraft and pilot response can be seen in Figure 5.17 for a perturbation at $\mathrm{Ma}_\infty = 0.672$ and $\Delta z = 8.0$m where the pilot response delay, τ, has been increased to 0.75s.

In Figure 5.17, given that the initial pilot reaction delay was 0.3 seconds, and the time delay margin at this flight condition was 0.38 s, the time delay margin in this scenario is close to zero. It can be seen that the aircraft and pilot responses grow over a period of 20 seconds, with vertical separation between tanker and receiver varying by up to 1.5 m. This indicates that the aircraft is extremely likely to become susceptible to PIOs. This could be further exacerbated by making small increases to the pilot or control system gains. The relevance of pilot input resonance and time delay margin is further supported efforts undertaken to mitigate PIOs in the C-17 involving pitch stick shaping that effectively reduced pilot input gain at smaller stick displacements, thus reducing pilot input resonance [46]. Other remediation efforts included reducing the time delay in the higher order system by 150 ms with a combination of filter changes [47, 72], and the addition of stick force command path lead in the pitch axis [47].

The comparison between the stick fixed and pilot-in-the-loop flight path responses is also of interest, as presented in Figure 5.18, for which the Precision pilot model is used.

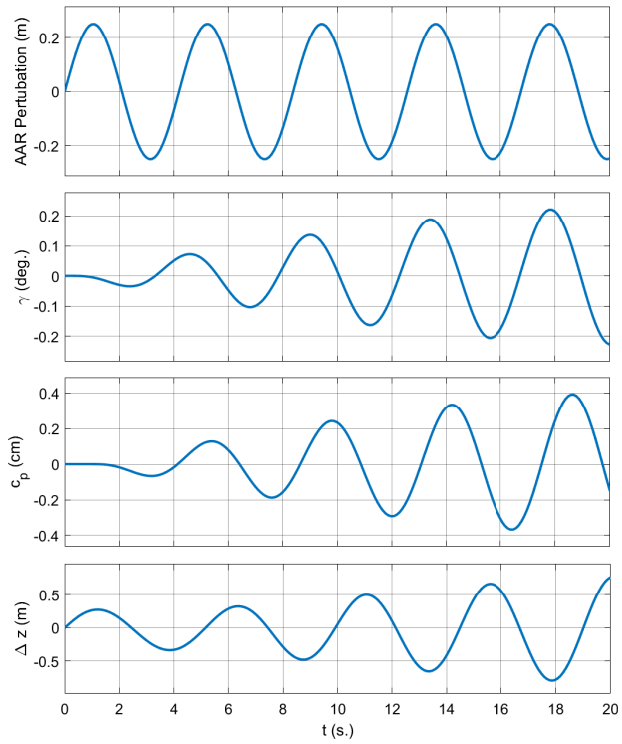

Figure 5.17: C-17 and pilot response to a perturbation of 1.5 rad/s at Ma_∞ = 0.672 and $\Delta z = 8.0$ m when response delay is increased to $\tau = 0.75$s.

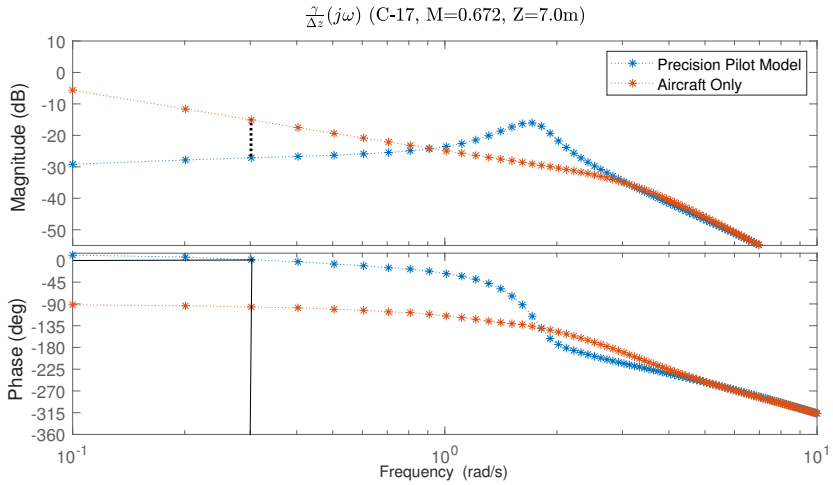

Figure 5.18: Bode plot of stick fixed and pilot-in-the-loop C-17 flight path response to a vertical separation perturbation between tanker and receiver. Ma_∞ = 0.672, $\Delta z = 7.0$m.

Figure 5.18 shows that at the crossover frequency of the pilot-in-the-loop aircraft response at $\mathrm{Ma}_\infty = 0.672$ and $\Delta z = 7.0$m, the pilot response damps out the aircraft oscillation when compared to the stick fixed aircraft response at the same frequency. Figure 5.19 compares the stick fixed and pilot-in-the-loop aircraft responses assuming the same flight condition of $\mathrm{Ma}_\infty = 0.672$, but with an increased vertical separation of $\Delta z = 8.5$m.

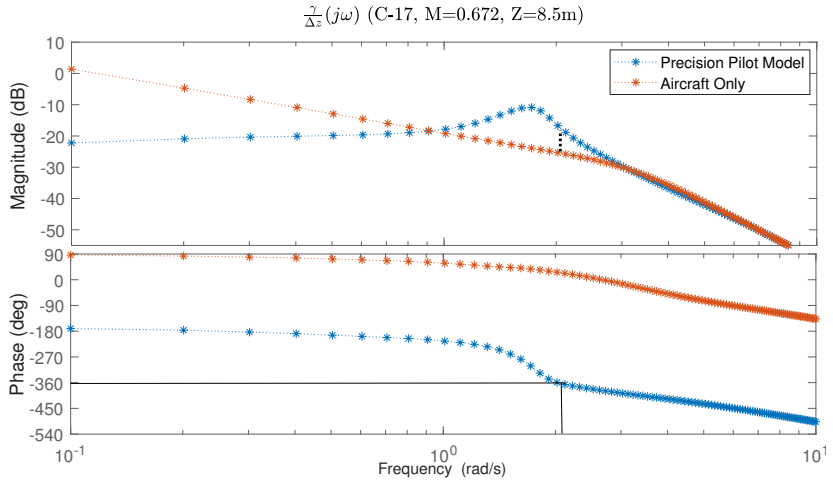

Figure 5.19: Bode plot of stick fixed and pilot-in-the-loop C-17 flight path response to a vertical separation perturbation between tanker and receiver. $\mathrm{Ma}_\infty = 0.672$, $\Delta z = 8.5$m.

In Figure 5.19 it can be seen that the pilot response to the perturbation creates resonance in the flight path response, resulting in a 7dB increase in flight path response when compared to the fixed stick response at the crossover frequency. This resonance effect cannot be seen in the behaviour of the C-5 at the same flight condition when examining Figure 5.20.

In general, the size and sluggishness of the C-5 makes it much less reactive to higher frequency perturbations, either from external aerodynamics or pilot inputs. Hence, there is little difference between stick fixed and pilot-in-the-loop responses, even during high-speed AAR performed at a vertical separation with detrimental positional static stability characteristics.

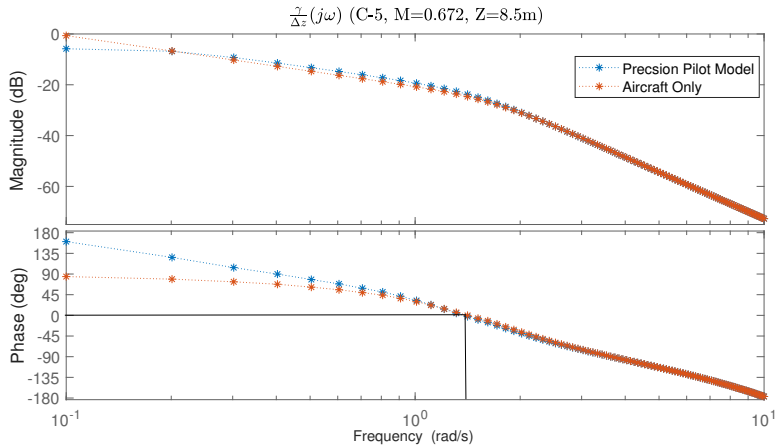

Figure 5.20: Bode plot of stick fixed and pilot-in-the-loop C-5 receiver response to a vertical separation perturbation between tanker and receiver. $\mathrm{Ma}_\infty = 0.672$, $\Delta z = 8.5$m.

Finally, to examine the effect of airspeed, Figure 5.21 shows the receiver fixed stick and piloted response at an airspeed of $\mathrm{Ma}_\infty = 0.456$ and a vertical separation of $\Delta z = 8.5$m.

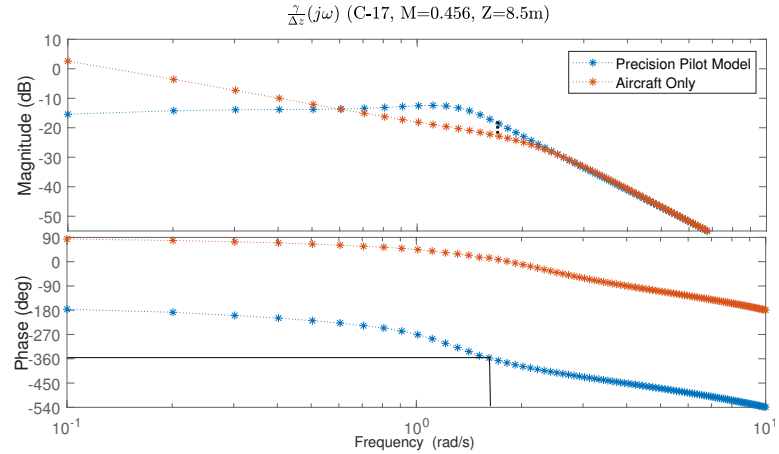

Figure 5.21: Bode plot of stick fixed and pilot-in-the-loop C-17 flight path response to a vertical separation perturbation between tanker and receiver. $\mathrm{Ma}_\infty = 0.456$, $\Delta z = 8.5$m.

Compared to the $\mathrm{Ma}_\infty = 0.672$ conditions, the crossover frequency reduced from 2.01 rad/s to 1.61 rad/s, and the magnitude of the pilot induced resonance at

the crossover frequency has reduced from 7 dB to 4 dB. Therefore, although a pilot-induced resonance exists, the reduced crossover frequency and subsequent increase in time delay margin implies a reduced PIO susceptibility at the lower speed flight condition.

5.2.1 Suggested PIO Prediction Guidelines

Based on the proposed method and subsequent analysis of the C-17 and C-5, the following factors can be indicative of PIO susceptibility:

- The combination of increased pilot input resonance with low time delay margin at the crossover frequency of various tanker-receiver separations; and
- Significant increase in pilot flight path response when piloted at crossover frequency compared to an stick fixed response.

This methodology only applies in tanker-receiver compatibility analysis if one seeks reasonable predictions about pilot and aircraft response during high gain tracking tasks such as AAR, notwithstanding that higher order system effects are neglected. It could also be used early in the design process for predicting AAR performance well before details of the higher-order control system are known. It may also be used in the design process to create guidelines for higher-order control system delays, or creating gain-scheduling guidelines specific to AAR. Furthermore, its viability with different mathematical pilot models obviates the necessity of performing simulator tests immediately. The Tustin pilot model specifically can be adapted for use with remotely piloted flight control systems, since the time delay could be tuned to better represent remote pilot system delays.

6 Conclusions and Recommendations

AAR refuelling is a procedure during which fuel is transferred from a tanker aircraft to a receiver aircraft in flight in order to increase the operational capabilities of the receiver. During the AAR refuelling procedure, the tanker and receiver must fly in close formation, which means that the receiver is subject to changing aerodynamic forces due to the local air velocities in the tanker wake. In order to perform AAR successfully, the receiver must make precise manœuvres which may be challenging to perform due to the nature of the wake flowfield. Current interest in modelling and analysis of AAR is being driven by a combination of automated refuelling technology development and pilot-in-the-loop simulations, and for both applications, consideration of the stability and control of the receiver and prediction of the air velocities in the tanker wake are critical. High-fidelity methods for AAR analysis can be costly in terms of time, computational power, and data infrastructure. Medium-fidelity analysis methods, which can produce useful results at a fraction of the investment, have use cases in situations such as aircraft clearance analysis and for exploration of the configuration space during the design process.

The principal goal of this research was to develop a multi-modal AAR analysis framework that is both light in terms of computational resources required, and robust to different types of tankers, receivers, and refuelling methods. This was achieved through a combination of potential flow-based aerodynamic computational methods and flight dynamics modelling. The framework developed was primarily concerned with receiver trim conditions, flight dynamics, and susceptibility to PIOs.

6.1 Conclusions

The critical contributions of this work pertained to existing methods being improved and combined in novel ways to create an analysis framework which generated new insights into the challenges associated with AAR. In particular, the mathematical basis was developed for the calculation of the sensitivities of the aerodynamic forces and moments experienced by the receiver to changes in the relative position between the tanker and receiver within a VLM. Building on this foundation, potential flow-based methods and closed-form aerodynamic models were combined, which led to new insights about receiver dynamics during PDR. The further addition of analytical pilot models to this framework led to the development of a new methodology for predicting PIO susceptibility.

Air velocities in the tanker wake were calculated using a VLM which was modified to include the effect of jetwash/propwash. This VLM also used vortex cores of finite velocity to limit numerical artifacts and discontinuities in the wake velocities. Integrating aerodynamic forces over the surface of the receiver aircraft also allowed for calculation of the forces and moments induced by a receiver flying in the tanker wake. Validation using flight test data showed good agreement in terms of the wake velocities and induced moments in the wake within the tanker wingspan, although the upwash values outside the wingspan of the tanker were over-predicted. Furthermore, in cases where the aerodynamic interaction between the tanker and receiver was highly coupled, the developed methodology was shown to be capable of calculating the positional stability values faster than a full calculation could be completed using the finite difference method.

This VLM was then included in the development of a multi-modal analysis framework designed to rapidly analyze tanker-receiver interactions during AAR. In addition to calculating trim points in the tanker wake and to identifying the regions of positional stability and instability, a major goal in the development of this framework is eventually to make quantitative and qualitative handling qualities predictions for the AAR task. Two different receiver trim strategies were examined, one that used a roll angle to counteract side force, and one that used no roll, but rather a yaw angle to counteract side force. The roll angle trim strategy was found to have an advantage over the yaw trim strategy, since the latter exhibited undesirable positional stability characteristics, with non-intuitive rudder deflections being required to maintain position behind the tanker. The closed-loop dynamic modes were also examined for both trim strategies. Examination of the phasors and eigenvectors revealed cross-coupling in the dynamic modes in both cases, implying a multi-axial receiver dynamic response to either external perturbation or pilot input during AAR.

Finally, this framework was further extended to examine aircraft and pilot response during FBR. New metrics were introduced for evaluating receiver performance during the AAR task by examining the positional stability characteristics of the tanker/receiver pair, the resonance of the pilot inputs, and the phase difference between changes in the vertical separation and the response of the flight path angle at different perturbation frequencies. Validation test cases examined the aircraft/pilot input response during flying boom refuelling for a C-17 and C-5 receiver being refuelled by a KC-135 tanker. These receivers were of research interest due to their similarity in geometry, but differences in AAR performance, with the C-17 having previously demonstrated susceptibility to PIOs at higher speeds. Results generated using the Tustin pilot model showed that pilot inputs to perturbations were smaller for the C-5 compared to the C-17 as the critical crossover frequency was increased. Furthermore, flight path control of the C-17 demanded higher frequency and higher amplitude pilot inputs, leading to the potential for PIOs at high speeds, assuming equivalent system time delays on the order of 100 ms. Results for the C-17 generated using the Precision pilot model showed slightly increased pilot response, greater phase delay between the receiver response and the aircraft, and a lower crossover frequency, resulting in similar predictions of the time delay margin at all flight conditions. The utility of this analysis framework is supported by the history of PIOs demonstrated by the C-17 during AAR, that drove improvements through changes to control system gains and equivalent system time delays. The framework may also be useful in the design process to create guidelines for higher-order control system delays, or for gain scheduling guidelines specific to AAR and other high gain tasks.

6.2 Recommendations for Future Developments

It is inherent to the nature of engineering that any models and analysis methods must eventually be subjected to the scrutiny of reality for evaluation. While the utility of the medium-fidelity analyses presented here has been demonstrated throughout this work in comparison to test cases, further study should seek to confirm that these results hold for different tanker/receiver pairs and flight conditions.

With respect to two-way coupled VLM calculations, the calculation of adjoint-based sensitivities demonstrated could be considered for use in more sophisticated analyses of FBR in which aerodynamic coupling between tanker and receiver is non-negligible, or where the dynamics of the tanker are of interest. CFD analysis of FBR may consider the adjoint-based sensitivities simpler to implement, since

adjoints are already used in aerodynamic and aero-structural optimization routines.

It should be noted that there are still physical effects that this framework does not take into account. In particular, unsteady effects cannot presently be considered. These could take the form of unsteadiness in the wake caused by tanker propwash/fuselage interactions, or changes in aerodynamic interaction between the tanker and receiver during coordinated turns.

In cases where dynamic cross-coupling is seen, it is unlikely that a purely frequency-based approach to handling quality prediction will be adequate. Furthermore, bandwidth-based handling quality prediction should also consider these cross-coupling effects to provide a more complete picture of flying qualities and handling qualities during probe and drogue AAR.

Bibliography

[1] C. S. Buttrill, P. D. Arbuckle, and K. D. Hoffler, "Simulation model of a twin-tail, high performance airplane," Tech. Rep., NASA-TM-107601, NASA, 1992.

[2] P. Thomas, U. Bhandari, S. Bullock, T. Richardson, and J. duBois, "Advances in air-to-air refueling," *Progress In Aerospace Science*, vol. 71, pp. 14–35, 2014. https://doi.org/10.1016/j.paerosci.2014.07.001

[3] M. Toydas, "Fuel savings opportunities from air refueling," Master's thesis, Air Force Institute of Technology, 2010. https://scholar.afit.edu/etd/2091/

[4] R. Nangia, "Operations and aircraft design towards greener civil aviation using air-to-air refuelling," *Aeronautical Journal*, vol. 110, no. 1113, pp. 705–721, 2006. https://doi.org/10.1017/S0001924000001585

[5] W. Mao and F. Eke, "A survey of the dynamics and control of aircraft during aerial refueling," *Nonlinear Dynamics and Systems Theory*, vol. 8, no. 4, pp. 375–388, 2008. https://www.e-ndst.kiev.ua/v8n4/6(25).pdf

[6] NATO, *Guide to Obtaining Air-to-Air Refuelling Clearances and Compatibility Certification*. North Atlantic Treaty Organization, February 2016.

[7] N. Fezans and T. Jann, "Modeling and simulation for the automation of aerial refueling of military transport aircraft with the probe-and-drogue system," in *AIAA Modeling and Simulation Technologies Conference*, p. 4008, 2017. https://doi.org/10.2514/6.2017-4008

[8] A. Bloy, P. Lamont, H. Abu-Assaf, and K. Ali, "The lateral dynamic stability and control of a large receiver aircraft during air-to-air refuelling," *Aeronautical Journal*, vol. 90, pp. 237–243, 1986. https://doi.org/10.1017/S0001924000015773

[9] A. Bloy, K. Ali, and V. Trochalidis, "The longitudinal dynamic stability and control of a large receiver aircraft during air-to-air refueling," *Aeronautical Journal*, vol. 91, no. 902, pp. 64–71, 1987. https://doi.org/10.1017/S0001924000050764

[10] A. Bloy and V. Trochalidis, "The performance and longitudinal stability and control of large receiver aircraft during air to air refuelling," *Aeronautical Journal*, vol. 93, no. 930, pp. 367–378, 1989. https://doi.org/10.1017/S0001924000022193

[11] A. Bloy and V. Trochalidis, "The aerodynamic interference between tanker and receiver aircraft during air-to-air refuelling," *Aeronautical Journal*, vol. 94, no. 935, pp. 165–171, 1990. https://doi.org/10.1017/S0001924000022776

[12] A. Bloy, V. Trochalidis, and M. West, "The aerodynamic interference between a flapped tanker aircraft and a receiver aircraft during air-to-air refueling," *Aeronautical Journal*, vol. 95, pp. 274–282, October 1991. https://doi.org/10.1017/S0001924000024106

[13] A. Bloy and M. Jouma'a, "Trailing vortex effects on large receiver aircraft," *Journal of Aircraft*, vol. 32, pp. 1198–1204, 1995. https://doi.org/10.2514/3.46864

[14] A. Bloy and M. West, "Interference between tanker wing wake with roll-up and receiver aircraft," *Journal of Aircraft*, vol. 31, no. 5, pp. 1214–1216, 1994. https://doi.org/10.2514/3.46633

[15] A. Bloy and K. Lea, "Directional stability of a large receiver aircraft in air-to-air refueling," *Journal of Aircraft*, vol. 32, no. 2, pp. 453–455, 1995. https://doi.org/10.2514/3.46741

[16] A. Bloy and M. Khan, "Modeling of the receiver aircraft in air-to-air refueling," *Journal of Aircraft*, vol. 38, no. 2, pp. 393–396, 2001. https://doi.org/10.2514/2.2775

[17] S. Venkataramanan and A. Dogan, "Dynamic effects of trailing vortex with turbulence & time-varying inertia in aerial refueling," in *AIAA Atmospheric Flight Mechanics Conference and Exhibit*, no. AIAA 2004-4945, (Providence, RI), AIAA, August 2004. https://doi.org/10.2514/6.2004-4945

[18] A. Dogan, S. Venkataramanan, and W. Blake, "Modeling of aerodynamic coupling between aircraft in close proximity," *Journal of Aircraft*, vol. 42, pp. 941–955, July–August 2005. https://doi.org/10.2514/1.7579

[19] A. Dogan, S. Sato, and W. Blake, "Flight control and simulation for aerial refueling," in *AIAA Guidance, Navigation, and Control Conference and Exhibit*, no. AIAA 2005-6264, (San Francisco, CA), AIAA, August 2005. https://doi.org/10.2514/6.2005-6264

[20] J. Tucker, A. Dogan, and W. Blake, "Derivation of the dynamics equations of receiver aircraft in aerial refueling," in *45th AIAA Aerospace Sciences*

Meeting and Exhibit, no. AIAA 2007-251, (Reno, NE), AIAA, January 2007. https://doi.org/10.2514/1.35892

[21] A. Dogan, T. Lewis, and W. Blake, "Flight data analysis and simulation of wind effects during aerial refueling," *Journal of Aircraft*, vol. 45, pp. 2036–2048, November–December 2008. https://doi.org/10.2514/1.36797

[22] W. Blake, E. Dickes, and D. Gingras, "UAV aerial refueling – wind tunnel results and comparison with analytical predictions," in *AIAA Atmospheric Flight Mechanics Conference and Exhibit*, no. AIAA 2004-4820, (Providence, RI), AIAA, August 2004. https://doi.org/10.2514/6.2004-4820

[23] A. Dogan and W. Blake, "Modeling of bow wave effect in aerial refueling," in *AIAA Atmospheric Flight Mechanics Conference*, no. AIAA-2010-7926, AIAA, August 2010. https://doi.org/10.2514/6.2010-7926

[24] X. Dai, Z. Wei, and Q. Quan, "Modeling and simulation of bow wave effect in probe and drogue aerial refueling," *Chinese Journal of Aeronautics*, vol. 29, no. 2, pp. 448–461, 2016. https://doi.org/10.1016/j.cja.2016.02.001

[25] A. Dogan, W. Blake, and C. Haag, "Bow wave effect in aerial refueling: Computational analysis and modeling," *Journal of Aircraft*, vol. 50, no. 6, pp. 1856–1868, 2013. https://doi.org/10.2514/1.C032165

[26] Y. Liu, H. Wang, Z. Su, and J. Fan, "Deep learning based trajectory optimization for UAV aerial refueling docking under bow wave," *Aerospace Science and Technology*, vol. 80, pp. 392–402, 2018. https://doi.org/10.1016/j.ast.2018.07.024

[27] J. Katz, "Aerodynamic aspects of unmanned aerial vehicle aerial refueling," *Journal of Aircraft*, vol. 54, no. 6, pp. 2311-2316, 2017. https://doi.org/10.2514/1.C034373

[28] B. Maskew, "Formation flying benefits based on vortex lattice calculations," *NASA Technical Report*, NASA-CR-151974, 1977.

[29] W. Blake and D. Multhopp, "Design, performance and modeling considerations for close formation flight," in *23rd Atmospheric Flight Mechanics Conference*, vol. 150, p. 2, 1998. https://doi.org/10.2514/6.1998-4343

[30] W. Blake, "An aerodynamic model for simulation of close formation flight," in *AIAA Modeling and Simulation Technologies Conference and Exhibit*, no. AIAA 2000-4304, (Denver, CO), AIAA, August 2000. https://doi.org/10.2514/6.2000-4304

[31] S. Venkataramanan, A. Dogan, and W. Blake, "Vortex effect modelling in aircraft formation flight," in *AIAA Atmospheric Flight Mechanics Conference and Exhibit*, no. AIAA 2012-5385, 2003. https://doi.org/10.2514/6.2003-5385

[32] W. Blake and D. Gingras, "Comparison of predicted and measured formation flight interference effects," *Journal of Aircraft*, vol. 41, pp. 201–207, March–April 2004. https://doi.org/10.2514/1.9278

[33] G. Bramesfeld and M. Maughmer, "Effects of wake rollup on formation-flight aerodynamics," *Journal of Aircraft*, vol. 45, pp. 1167–1173, July–August 2008. https://doi.org/10.2514/1.33821

[34] D. Saban and J. Whidborne, "Modeling of wake vortex effects for unmanned air vehicle simulations," in *AIAA Modeling and Simulation Technologies Conference*, no. AIAA 2009-5686, (Chicago, IL), AIAA, August 2009. https://doi.org/10.2514/6.2009-5686

[35] Q. Zhang and H. H. T. Liu, "Aerodynamics modeling and analysis of close formation flight," *Journal of Aircraft*, vol. 54, no. 6, pp. 2192-2204, 2017. https://doi.org/10.2514/1.C034271

[36] D. Fleischmann and M. M. Lone, "Analysis of wake surfing benefits using a fast unsteady vortex lattice method," in *AIAA Scitech 2019 Forum*, no. AIAA 2019-0264, 2019. https://doi.org/10.2514/6.2019-0264

[37] S. Ning, T. Flanzer, and I. Kroo, "Aerodynamic performance of extended formation flight," in *48th AIAA Aerospace Sciences Meeting Including the New Horizons Forum and Aerospace Exposition*, no. AIAA 2010-1240, (Orlando, FL), AIAA, January 2010. https://doi.org/10.2514/1.C031046

[38] F. Holzäpfel, "Probabilistic two-phase wake vortex decay and transport model," *Journal of Aircraft*, vol. 40, pp. 323–331, March–April 2003. https://doi.org/10.2514/2.3096

[39] J. E. Kless, M. J. Aftosmis, S. A. Ning, and M. Nemec, "Inviscid analysis of extended-formation flight," *AIAA Journal*, vol. 51, no. 7, pp. 1703–1715, 2013. https://doi.org/10.2514/1.J052224

[40] T. Jann, N. Fezans, *et al.*, "Assisted and automated aerial refuelling - overview of the conducted research at the German Aerospace Center (DLR)," in *34th Congress of the International Council of the Aeronautical Sciences*, no. ICAS2024-0819, 2024.

[41] A. Denis, *A simplified vortex sheet roll-up method for formation flight*. PhD thesis, Massachusetts Institute of Technology, 2004. http://hdl.handle.net/1721.1/28898

[42] P. Weinerfelt and A. Nilsson, "A dynamic real time model for air-to-air refueling," in *27th Congress of the International Council of the Aeronautical Sciences*, ICAS, 2010.

[43] N. Fezans, T. Jann, T. Gerlach, D. Niedermeier, J. Hettwer, S. Lademann, J. Gotschlich, S. Schopferer, S. Lorenz, U. Durak, *et al.*, "Modelling and simulation for aerial refueling automation research for manned and unmanned aircraft," in *DLRK 2016*, DLR, September 2016.

[44] Y. Li, Y. Zhang, and J. Bai, "Numerical simulation of the aerodynamic influence of aircrafts during aerial refueling with engine jet," *International Journal of Aeronautical and Space Sciences*, vol. 21, pp. 15–24, 2020. https://doi.org/10.1007/s42405-019-00212-2

[45] J. Bradley, "The handling and performance trials needed to clear an aircraft to act as a receiver during air-to-air refuelling," in *AGARD Conference Proceedings No. 373*, 1984.

[46] O. Iloputaife, G. Svoboda, and T. Bailey, "Handling qualities design of the C-17A for receiver-refueling," in *Guidance, Navigation, and Control Conference*, no. AIAA 1996-3746, AIAA, 1996. https://doi.org/10.2514/6.1996-3746

[47] G. L. Weltz, M. G. Barajas, and K. M. Shweyk, "Improvements in aerial refueling flight control system for a large receiver aircraft," in *AIAA Scitech 2021 Forum*, no. AIAA 2021-0716, 2021. https://doi.org/10.2514/6.2021-0716

[48] M. Taschner, "A handling qualities investigation of selected response-types for the air refueling task," in *20th Atmospheric Flight Mechanics Conference*, no. AIAA-95-3428, 1995. https://doi.org/10.2514/6.1995-3428

[49] M. J. Taschner, "A handling qualities investigation of conventional, rate command/attitude hold, and attitude command/attitude hold response-types in the probe and drogue air refueling task," Master's thesis, 1994. https://scholar.afit.edu/etd/6636/

[50] D. G. Mitchell and D. H. Klyde, "Identifying a pilot-induced oscillation signature: New techniques applied to old problems," *Journal of Guidance, Control, and Dynamics*, vol. 31, no. 1, pp. 215–224, 2008. https://doi.org/10.2514/1.31470

[51] J. H. Bidinotto, H. C. d. Moura, and J. P. C. A. d. Macedo, "A survey of human pilot models for study of pilot-induced oscillation (PIO) in longitudinal aircraft motion," *The Aeronautical Journal*, vol. 126, no. 1297, pp. 533–546, 2022. https://doi.org/10.1017/aer.2021.82

[52] L. Wang, H. Yin, Y. Guo, T. Yue, and X. Jia, "Closed-loop motion characteristic requirements of receiver aircraft for probe and drogue aerial refueling," *Aerospace Science and Technology*, vol. 93, p. 105293, 2019. https://doi.org/10.1016/j.ast.2019.07.026

[53] H. Yin, L. Wang, T. Yue, and H. Liu, "Pilot-induced oscillation analysis for receiver in flying-boom aerial refueling via mission-oriented evaluation," in *2019 IEEE 10th International Conference on Mechanical and Aerospace Engineering (ICMAE)*, pp. 47–51, IEEE, 2019. https://doi.org/10.1109/ICMAE.2019.8881023

[54] C. Lu, L. Wang, T. Yue, and H. Liu, "Longitudinal flying qualities evaluation method for receiver in probe and drogue aerial refueling," in *2020 11th International Conference on Mechanical and Aerospace Engineering (ICMAE)*, pp. 87–92, IEEE, 2020. https://doi.org/10.1109/ICMAE50897.2020.9178904

[55] J. Katz and A. Plotkin, *Low-Speed Aerodynamics*, vol. 13. Cambridge University Press, 2001.

[56] J. T. Conway, "Analytical solutions for the actuator disk with variable radial distribution of load," *Journal of Fluid Mechanics*, vol. 297, pp. 327–355, 1995. https://doi.org/10.1017/S0022112095003120

[57] G. Droandi and G. Gibertini, "Assessment of a propeller model embedded on a panel method code for aircraft aerodynamics.," *The Journal of Aerospace Science, Technology and Systems*, vol. 91, no. 3/4, pp. 98–108, 2012. https://hdl.handle.net/11311/740973

[58] C. Alba, A. Elham, B. German, and L. L. Veldhuis, "A surrogate-based multidisciplinary design optimization framework exploiting wing-propeller interaction," in *18th AIAA/ISSMO Multidisciplinary Analysis and Optimization Conference*, no. AIAA 2017-4329, AIAA, 2017. https://doi.org/10.2514/6.2017-4329

[59] D. D. Vicroy, P. M. Vijgen, H. M. Reimer, J. L. Gallegos, and P. R. Spalart, "Recent NASA wake-vortex flight tests, flow-physics database and wake-development analysis," in *1998 World Aviation Conference*, vol. 107, pp. 1764–1777, American Technical Publishers Ltd., 1998. https://doi.org/10.2514/6.1998-5592

[60] J. Hansen and B. Cobleigh, "Induced moment effects of formation flight using two F/A-18 aircraft," in *Flight Mechanics Conference and Exhibit*, no. AIAA 2002-4489, (Monterey, CA), AIAA, 2002. https://doi.org/10.2514/6.2002-4489

[61] E. J. Cramer, J. E. Dennis, Jr, P. D. Frank, R. M. Lewis, and G. R. Shubin, "Problem formulation for multidisciplinary optimization," *SIAM Journal on Optimization*, vol. 4, no. 4, pp. 754–776, 1994. https://doi.org/10.1137/0804044

[62] A. Chakraborty, "Linear and nonlinear analysis of susceptibility of F/A-18 flight control laws to the falling leaf mode," Master's thesis, 2010. https://hdl.handle.net/11299/92982

[63] M. R. Napolitano and J. M. Spagnuolo, "Determination of the stability and control derivatives of the NASA F/A-18 HARV using flight data," Tech. Rep., NASA-CR-194838, NASA, 1993.

[64] K. W. Iliff and K.-S. C. Wang, "Extraction of lateral-directional stability and control derivatives for the basic F-18 aircraft at high angles of attack," Tech. Rep., NASA-TM-4786, NASA, 1997.

[65] M. Napolitano, A. Paris, B. Seanor, and A. Bowers, "Estimation of the longitudinal aerodynamic parameters from flight data for the NASA F/A-18 HARV," in *21st Atmospheric Flight Mechanics Conference*, no. AIAA 1996-3419, AIAA, 1996. https://doi.org/10.2514/6.1996-3419

[66] J. B. Davidson, *High-alpha research vehicle lateral-directional control law description, analyses, and simulation results.* National Aeronautics and Space Administration, Langley Research Center, 1998.

[67] A. J. Ostroff, K. D. Hoffler, and M. S. Proffitt, *High-Alpha Research Vehicle (HARV) Longitudinal Controller: Design, Analyses, and Simulation Results.* National Aeronautics and Space Administration, Langley Research Center, 1994.

[68] "Flying qualities of piloted vehicles," Standard MIL-STD-1797, United States Air Force, Mar. 1987.

[69] "Military specification flying qualities of piloted airplanes," Mil. Spec. MIL-F-8785C, Air Force Flight Dynamics Laboratory, Nov. 1980.

[70] K. J. Latimer, "A limited investigation of probe-and-drogue aerial refueling tasks to evaluate closed-loop handling qualities (HAVE GAS II).," Tech. Rep., AFFTC-TR-97-13, Air Force Flight Test Center Edwards AFB, 1997.

[71] D. H. Klyde, D. G. Mitchell, and K. J. Latimer, "Development of the probe-and-drogue handling qualities demonstration maneuver," *Journal of Guidance, Control, and Dynamics*, vol. 22, no. 4, pp. 528–535, 1999. https://doi.org/10.2514/2.4429

[72] O. Iloputaife, "Minimizing pilot-induced-oscillation susceptibility during C-17 development," in *22nd Atmospheric Flight Mechanics Conference*, no. AIAA-97-3497, AIAA, 1997. https://doi.org/10.2514/6.1997-3497

[73] L. V. Schmidt, *Introduction to Aircraft Flight Dynamics.* American Institute of Aeronautics and Astronautics, 1998.

[74] A. Tustin, "The nature of the operator's response in manual control, and its implications for controller design," *Journal of the Institution of Electrical Engineers-Part IIA: Automatic Regulators and Servo Mechanisms*, vol. 94, no. 2, pp. 190–206, 1947. https://doi.org/10.1049/ji-2a.1947.0025

[75] D. T. McRuer and E. S. Krendel, "Mathematical models of human pilot behavior," Tech. Rep. AGARD-AG-188, NATO, 1974.

[76] R. K. Heffley and W. F. Jewell, "Aircraft handling qualities data," Tech. Rep., NASA-CR-2144, NASA, 1972.

[77] A. Guha, "Optimum fan pressure ratio for bypass engines with separate or mixed exhaust streams," *Journal of Propulsion and Power*, vol. 17, no. 5, pp. 1117–1122, 2001. https://doi.org/10.2514/2.5852

Appendices

A Jetwash Model Exploration

The question of how to model jetwash was briefly explored during the development of this research. The method presented here was ultimately rejected due to its complicated implementation requiring a discretised spatial grid within the potential flow method environment. To begin, it is assumed that the flow velocity in the x-direction can be modelled via the diffusion equation.

$$\frac{\partial u}{\partial x} = \mu \frac{\partial^2 u}{\partial y^2} \tag{A.1}$$

where ρ is the fluid density, u is the x component of the fluid velocity, and μ is "velocity viscosity". This equation can be discretised in x and y and solved using an implicit scheme as follows:

$$\frac{u_{i,j} - u_{i,j-1}}{k} = \mu \frac{u_{i+1,j} - 2u_{i,j} + u_{i-1,j}}{h^2} \tag{A.2}$$

Points in x are indexed with i and points in y are indexed with j. The grid discretisation size in x is k and the grid discretisation size in y is h. This can be rearranged to find values of $u_{n,j}$ as follows:

$$u_{i,j-1} = -\lambda u_{i+1,j} - \lambda u_{i-1,j} + (2\lambda + 1)u_{i,j} \tag{A.3}$$

where $\lambda = \frac{\mu k}{\rho h^2}$. Given boundary conditions for $u_{i,j-1}$ for all i, the above formula can be used to create a series of equations to solve for all values of $u_{i,j}$ for all i. This essentially means knowing the velocity of a jet at the outlet. An example of the jet velocity diffusion profile, assuming a nozzle radius of 1.75 m and a value of λ of 1.25, can be seen in Figure A.1. This velocity profile looks somewhat physical in terms of comparison to a real jet, although diffusion constants must be tuned by engineering judgment rather than being derived from physical insights.

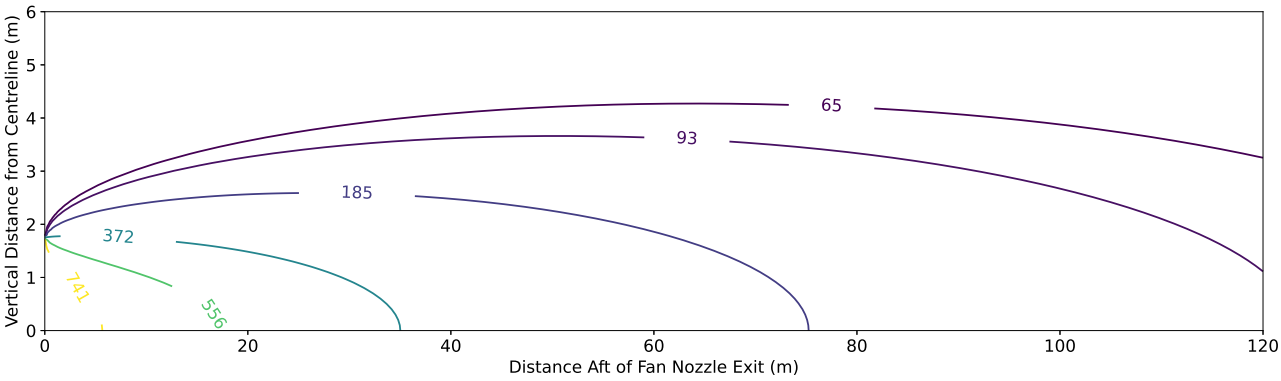

Figure A.1: Velocity diffusion profile.

To infer reasonable velocities at the nozzles of turbofan engines, we use the total thrust, bypass ratio, and total mass flow rate.

$$T = \dot{m}_c V_c + \text{BPR}\dot{m}_f V_f \tag{A.4}$$

$$\dot{m}_o = \dot{m}_c + \dot{m}_f \tag{A.5}$$

$$\text{BPR} = \frac{\dot{m}_f}{\dot{m}_c} \tag{A.6}$$

where T is thrust, $\dot{m}_c$ is the mass flow rate of the turbofan core, V_c is the air velocity at the core outlet, $\dot{m}_f$ is the mass flow rate of the turbofan fan, V_f is the air velocity at the fan outlet, and BPR is the bypass ratio. From these equations, the thrust can be calculated in terms of the total mass flow rate, bypass ratio, V_c, and V_f.

$$T = \frac{\dot{m}_o}{\text{BPR}+1} V_c + \frac{\text{BPR}\dot{m}_o}{\text{BPR}+1} V_f \tag{A.7}$$

Here the values of V_c and V_f can be found by assuming some ratio between them. Based on Guha [77], we assume that $V_f/V_c = 0.8$.

$$V_c = \frac{T}{\frac{\dot{m}_o}{\text{BPR}+1} + 0.8\frac{\text{BPR}\dot{m}_o}{\text{BPR}+1}} \tag{A.8}$$

$$V_f = 0.8 V_c \tag{A.9}$$

We can then determine the radius of the core outlet and the radius of the fan outlet by using mass flow rate equations and the bypass ratio. The areas of the core flow A_c and fan flow A_f are given by

$$A_c = \pi r_c^2 \qquad \text{and} \qquad A_f = \pi(r_t^2 - r_c^2) \tag{A.10}$$

where r_t is the total radius of the engine outlet. The mass flow rates of the core and fan are given by

$$\dot{m}_c = \rho_c A_c V_c \qquad \text{and} \qquad \dot{m}_c = \rho_f A_f V_f \tag{A.11}$$

Using the bypass ratio, we can then say that

$$\text{BPR} = \frac{V_f}{V_c}\frac{A_f}{A_B} \tag{A.12}$$

Via these equations, we can find that the radius of the core outlet is

$$R_c = \sqrt{\frac{r_t^2}{V_c \text{BPR}/V_f + 1}} \tag{A.13}$$

Using these equations, we can set the boundary conditions at the jet outlet assuming we know the bypass ratio, total thrust generated, total mass flow rate, and the total exhaust diameter. Figure A.2 shows a jet profile generated for a PW4060 engine in a velocity field of 200 m/s assuming BPR = 4.8, $T = 224.8 \times 10^3$ N, $\dot{m}_o = 818$ kg/s, and $r_t = 2.84$m.

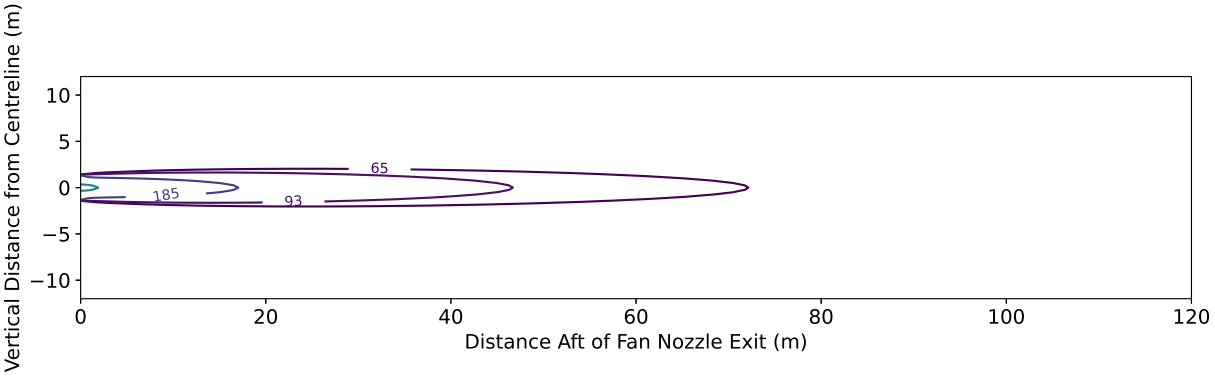

Figure A.2: PW4060 jetwash profile when flying at 200 m/s.

Ultimately this model was not developed further as it lacks physical insight although the jet profiles look plausible. Additionally, the required spatial discretization added complexity which was avoided by simply assuming a streamtube jet velocity originating from the jet outlet in the VLM.

B F/A-18 VLM Breakpoints

This appendix contains the details of the F/A-18 geometry used throughout this work. The VLM breakpoints used to model the F/A-18 are given Table B.1. The points in Table B.1 are listed in a counter-clockwise order and the aircraft is symmetrical about $y = 0$.

Table B.1: Coordinate points used to define the F/A-18.

Surface	Point 1 (x,y,z) [m]	Point 2 (x,y,z) [m]	Point 3 (x,y,z) [m]	Point 4 (x,y,z) [m]
Inboard R. Wing	$(-8.18, -1.06, 0.00)$	$(-12.81, -1.06, 0.00)$	$(-12.65, -3.91, -0.06)$	$(-9.83, -3.91, -0.15)$
Outboard R. Wing	$(-9.83, -3.91, -0.15)$	$(-12.65, -3.91, -0.06)$	$(-12.55, -5.70, -0.13)$	$(-10.86, -5.70, -0.24)$
R. H-Stab.	$(-13.70, -1.06, 0.00)$	$(-16.21, -1.06, 0.00)$	$(-17.25, -3.30, -0.08)$	$(-16.10, -3.30, -0.08)$
Lower R. Vertical Stab.	$(-11.77, -0.98, 0.95)$	$(-14.64, -0.98, 0.95)$	$(-15.00, -1.58, 2.60)$	$(-13.31, -1.58, 2.60)$
Upper R. V-Stab.	$(-13.31, -1.58, 2.60)$	$(-15.00, -1.58, 2.60)$	$(-15.16, -1.85, 3.36)$	$(-14.02, -1.85, 3.36)$
Body	$(0.00, 0.00, 0.00)$	$(-16.46, 0.00, 0.00)$	$(-16.46, -1.06, 0.00)$	$(-5.43, -1.06, 0.00)$
Body	$(0.00, 0.00, 0.00)$	$(-16.46, 0.00, 0.00)$	$(-16.46, 0.00, 1.31)$	$(-3.51, 0.00, 1.31)$

C F/A-18 Aerodynamic Model

This appendix contains the details of the aerodynamic model used in this paper based on the model published by Chakraborty *et al.* [62]

$$\begin{aligned} C_m =& \big(C_{m\alpha 3}\alpha^3 + C_{m\alpha 2}\alpha^2 + C_{m\alpha 1}\alpha\big) + \big(C_{m\delta_e 2}\alpha^2 + C_{m\delta_e 1}\alpha + C_{m\delta_e 0}\big)\delta_e \\ &+ \frac{\bar{c}}{2V}\big(C_{mq3}\alpha^3 + C_{mq2}\alpha^2 + C_{mq1}\alpha + C_{mq0}\big)q \end{aligned} \tag{C.1}$$

Table C.1: Pitching Moment Coefficient Model Data

Airframe	Control Surfaces	Rates
$C_{m\alpha 3} = -1.5022$	$C_{m\delta_e 2} = 0.9338$	$C_{mq3} = 64.7190$
$C_{m\alpha 2} = 0.9176$	$C_{m\delta_e 1} = -0.3245$	$C_{mq2} = -68.5641$
$C_{m\alpha 1} = -0.3823$	$C_{m\delta_e 0} = -0.9051$	$C_{mq1} = 10.9921$
		$C_{mq0} = -4.1186$

$$\begin{aligned} C_\ell =& \big(C_{\ell\beta 4}\alpha^4 + C_{\ell\beta 3}\alpha^3 + C_{\ell\beta 2}\alpha^2 + C_{\ell\beta 1}\alpha + C_{\ell\beta 0}\big)\beta \\ &+ \big(C_{\ell\delta_a 3}\alpha^3 + C_{\ell\delta_a 2}\alpha^2 + C_{\ell\delta_a 1}\alpha + C_{\ell\delta_a 0}\big)\delta_a \\ &+ \big(C_{\ell\delta_r 3}\alpha^3 + C_{\ell\delta_r 2}\alpha^2 + C_{\ell\delta_r 1}\alpha + C_{\ell\delta_r 0}\big)\delta_r \\ &+ \frac{b}{2V}\big(C_{\ell p1}\alpha + C_{\ell p0}\big)p + \frac{b}{2V}\big(C_{\ell r2}\alpha^2 + C_{\ell r1}\alpha + C_{\ell r0}\big)r \end{aligned} \tag{C.2}$$

$$\begin{aligned} C_n =& \big(C_{n\beta 2}\alpha^2 + C_{n\beta 1}\alpha + C_{n\beta 0}\big)\beta \\ &+ \big(C_{n\delta_a 3}\alpha^3 + C_{n\delta_a 2}\alpha^2 + C_{n\delta_a 1}\alpha + C_{n\delta_a 0}\big)\delta_a \\ &+ \big(C_{n\delta_r 4}\alpha^4 + C_{n\delta_r 3}\alpha^3 + C_{n\delta_r 2}\alpha^2 + C_{n\delta_r 1}\alpha + C_{n\delta_r 0}\big)\delta_r \\ &+ \frac{b}{2V}\big(C_{np1}\alpha + C_{np0}\big)p + \frac{b}{2V}\big(C_{nr1}\alpha + C_{nr0}\big)r \end{aligned} \tag{C.3}$$

Table C.2: Rolling Moment Coefficient Model Data

Airframe	Control Surfaces	Rates
$C_{\ell\beta 4} = -1.6196$	$C_{\ell\delta_a 3} = 0.1989$	$C_{\ell p 1} = 0.2377$
$C_{\ell\beta 3} = 2.3843$	$C_{\ell\delta_a 2} = -0.2646$	$C_{\ell p 0} = -0.3540$
$C_{\ell\beta 2} = -0.3620$	$C_{\ell\delta_a 1} = -0.0516$	$C_{\ell r 2} = -1.0871$
$C_{\ell\beta 1} = -0.4153$	$C_{\ell\delta_a 0} = 0.1424$	$C_{\ell r 1} = 0.7804$
$C_{\ell\beta 0} = -0.0556$	$C_{\ell\delta_r 3} = -0.0274$	$C_{\ell r 0} = 0.1983$
	$C_{\ell\delta_r 2} = 0.0083$	
	$C_{\ell\delta_r 1} = 0.0014$	
	$C_{\ell\delta_r 0} = 0.0129$	

Table C.3: Yawing Moment Coefficient Model Data

Airframe	Control Surfaces	Rates
$C_{n\beta 2} = -0.3816$	$C_{n\delta_a 3} = 0.2694$	$C_{np 1} = -0.0881$
$C_{n\beta 1} = 0.0329$	$C_{n\delta_a 2} = -0.3413$	$C_{np 0} = 0.0792$
$C_{n\beta 0} = 0.0885$	$C_{n\delta_a 1} = 0.0584$	$C_{nr 1} = -0.1307$
	$C_{n\delta_a 0} = 0.0104$	$C_{nr 0} = -0.4326$
	$C_{n\delta_r 4} = 0.3899$	
	$C_{n\delta_r 3} = -0.8980$	
	$C_{n\delta_r 2} = 0.5564$	
	$C_{n\delta_r 1} = -0.0176$	
	$C_{n\delta_r 0} = -0.0780$	

$$
\begin{aligned}
C_Y =& \big(C_{Y\beta 2}\alpha^2 + C_{Y\beta 1}\alpha + C_{Y\beta 0}\big)\beta \\
&+ \big(C_{Y\delta_a 3}\alpha^3 + C_{Y\delta_a 2}\alpha^2 + C_{Y\delta_a 1}\alpha + C_{Y\delta_a 0}\big)\delta_a \\
&+ \big(C_{Y\delta_r 3}\alpha^3 + C_{Y\delta_r 2}\alpha^2 + C_{Y\delta_r 1}\alpha + C_{Y\delta_r 0}\big)\delta_r
\end{aligned}
\tag{C.4}
$$

Table C.4: Side Force Coefficient Model Data

Airframe	Control Surfaces
$C_{Y_{\beta 2}} = -0.1926$	$C_{Y_{\delta_a 3}} = -0.8500$
$C_{Y_{\beta 1}} = 0.2654$	$C_{Y_{\delta_a 2}} = 1.5317$
$C_{Y_{\beta 0}} = -0.7344$	$C_{Y_{\delta_a 1}} = 0.2403$
	$C_{Y_{\delta_a 0}} = -0.1656$
	$C_{Y_{\delta_r 3}} = 0.9351$
	$C_{Y_{\delta_r 2}} = -1.6921$
	$C_{Y_{\delta_r 1}} = 0.4082$
	$C_{Y_{\delta_r 0}} = 0.2054$

$$\begin{aligned} C_D =& \big(C_{D\alpha 4}\alpha^4 + C_{D\alpha 3}\alpha^3 + C_{D\alpha 2}\alpha^2 + C_{D\alpha 1}\alpha + C_{D\alpha 0}\big)\cos\beta + C_{D_0} \\ &+ \big(C_{D\delta_e 3}\alpha^3 + C_{D\delta_e 2}\alpha^2 + C_{D\delta_e 1}\alpha + C_{D\delta_e 0}\big)\delta_e \end{aligned} \tag{C.5}$$

Table C.5: Drag Coefficient Model Data

Airframe	Control Surfaces
$C_{D\alpha 4} = 1.4610$	$C_{D\delta_e 3} = -3.8578$
$C_{D\alpha 3} = -5.7341$	$C_{D\delta_e 2} = 4.2360$
$C_{D\alpha 2} = 6.3971$	$C_{D\delta_e 1} = -0.2739$
$C_{D\alpha 1} = -0.1995$	$C_{D\delta_e 0} = 0.0366$
$C_{D\alpha 0} = -1.4994$	
$C_{D_0} = 1.5036$	